

MAY 24 2005

REPORT DOCUMENTATION PAGE			Form Approved OMB No. 0704-0188	
Public reporting burden for this collection of information is estimated to average 1 hour per response, including the time for reviewing instructions, searching existing data sources, gathering and maintaining the data needed, and completing and reviewing the collection of information. Send comments regarding this burden estimate or any other aspect of this collection of information, including suggestions for reducing this burden, to Washington Headquarters Services, Directorate for Information Operations and Reports, 1215 Jefferson Davis Highway, Suite 1204, Arlington, VA 22202-4302, and to the Office of Management and Budget, Paperwork Reduction Project (0704-0188), Washington, DC 20503.				
1. AGENCY USE ONLY (Leave blank)		2. REPORT DATE 19.May.05		3. REPORT TYPE AND DATES COVERED THESIS
4. TITLE AND SUBTITLE STATE ESTIMATION OF INTERNATIONAL SPACE STATION CENTRIFUGE ROTOR WITH INCOMPLETE KNOWLEDGE OF DISTURBANCE INPUTS			5. FUNDING NUMBERS	
6. AUTHOR(S) 2D LT SULLIVAN MICHAEL J				
7. PERFORMING ORGANIZATION NAME(S) AND ADDRESS(ES) RICE UNIVERSITY			8. PERFORMING ORGANIZATION REPORT NUMBER CI04-1087	
9. SPONSORING/MONITORING AGENCY NAME(S) AND ADDRESS(ES) THE DEPARTMENT OF THE AIR FORCE AFIT/CIA, BLDG 125 2950 P STREET WPAFB OH 45433			10. SPONSORING/MONITORING AGENCY REPORT NUMBER	
11. SUPPLEMENTARY NOTES				
12a. DISTRIBUTION AVAILABILITY STATEMENT Unlimited distribution In Accordance With AFI 35-205/AFIT Sup 1			12b. DISTRIBUTION CODE	
13. ABSTRACT (Maximum 200 words)				
14. SUBJECT TERMS			15. NUMBER OF PAGES 146	
			16. PRICE CODE	
17. SECURITY CLASSIFICATION OF REPORT		18. SECURITY CLASSIFICATION OF THIS PAGE		19. SECURITY CLASSIFICATION OF ABSTRACT
20. LIMITATION OF ABSTRACT				

RICE UNIVERSITY

**State Estimation of International Space Station
Centrifuge Rotor with Incomplete Knowledge of
Disturbance Inputs**

By

Michael James Sullivan

A THESIS SUBMITTED
IN PARTIAL FULFILLMENT OF THE
REQUIREMENTS FOR THE DEGREE

Master of Science

APPROVED, THESIS COMMITTEE:

Satish Nagarajaiah, Associate Professor
Mechanical Engineering & Material Science

Pol D. Spanos, Lewis B. Ryon Professor
Mechanical Engineering & Material Science

DISTRIBUTION STATEMENT A
Approved for Public Release
Distribution Unlimited

Marcia K. O'Malley, Assistant Professor
Mechanical Engineering & Material Science

Nazareth Bedrossian, Group Leader
The Charles Stark Draper Laboratory

HOUSTON, TEXAS

MAY 2005

Note: The Views expressed in this thesis are those of the author and do not reflect the official policy or position of the United States Air Force, Department of Defense, or the U.S. Government

ABSTRACT

State Estimation of International Space Station Centrifuge Rotor with Incomplete Knowledge of Disturbance Inputs

by

Michael James Sullivan

This thesis develops a state estimation algorithm for the Centrifuge Rotor (CR) system where only relative measurements are available with limited knowledge of both rotor imbalance disturbances and International Space Station (ISS) thruster disturbances. A Kalman filter is applied to a plant model augmented with sinusoidal disturbance states used to model both the effect of the rotor imbalance and the ISS thrusters on the CR relative motion measurement. The sinusoidal disturbance states compensate for the lack of the availability of plant inputs for use in the Kalman filter. Testing confirms that complete disturbance modeling is necessary to ensure reliable estimation. Further testing goes on to show that increased estimator operational bandwidth can be achieved through the expansion of the disturbance model within the filter dynamics. In addition, Monte Carlo analysis shows the varying levels of robustness against defined plant/filter uncertainty variations.

ABSTRACT

State Estimation of International Space Station Centrifuge Rotor with Incomplete Knowledge of Disturbance Inputs

by

Michael James Sullivan

This thesis develops a state estimation algorithm for the Centrifuge Rotor (CR) system where only relative measurements are available with limited knowledge of both rotor imbalance disturbances and International Space Station (ISS) thruster disturbances. A Kalman filter is applied to a plant model augmented with sinusoidal disturbance states used to model both the effect of the rotor imbalance and the ISS thrusters on the CR relative motion measurement. The sinusoidal disturbance states compensate for the lack of the availability of plant inputs for use in the Kalman filter. Testing confirms that complete disturbance modeling is necessary to ensure reliable estimation. Further testing goes on to show that increased estimator operational bandwidth can be achieved through the expansion of the disturbance model within the filter dynamics. In addition, Monte Carlo analysis shows the varying levels of robustness against defined plant/filter uncertainty variations.

ACKNOWLEDGEMENTS

The author wishes to thank his advisor with Draper Laboratory, Dr. Nazareth Bedrossian, for his guidance throughout thesis research and write-up as well as his mentorship through the professional engineering development process.

The author thanks his advisor at Rice University, Dr. Satish Nagarajaiah, for his time and effort throughout this process.

The author also wishes to thank Dr. Ernest Griffith of Draper Laboratory for his continual guidance, support, encouragement, and advice during the thesis research and write-up.

The author would like to thank Dr. Rami Mangoubi of Draper Laboratory for his support and guidance during thesis research.

Finally, the author would like to thank, Dr. Pol D. Spanos and Dr. Marcia K. O'Malley, for their help and advice during the thesis write-up and approval process.

ASSIGNMENT

Draper Laboratory Report Number T-1508.

In consideration for the research opportunity and permission to prepare my thesis by and at
The Charles Stark Draper Laboratory, Inc., I hereby assign my copyright of the thesis to
The Charles Stark Draper laboratory, Inc., Cambridge, Massachusetts.

Michael J. Sullivan

March 31, 2005

Table of Contents

1	Introduction.....	1
1.1	Introduction to Centrifuge Accommodation Module (CAM)	3
1.2	Alternative Estimation Options	9
1.3	Thesis Overview and Content	11
2	Problem Overview	13
2.1	Modeling Assumptions.....	13
2.2	Derivation of the Linear, Time-Varying Equations of Motion	14
2.2.1	EOMs for Coupled x Translation and ϕ_y Rotation	16
2.2.1.1	EOMs for x Translation	17
2.2.1.2	EOMs for ϕ_y Rotation	19
2.2.2	EOMs for Coupled y Translation and ϕ_x Rotation	21
2.2.2.1	EOMs for y Translation	22
2.2.2.2	EOMs for ϕ_x Rotation	23
2.3	Model Frequency Response	24
3	Solution Method.....	25
3.1	Filter Model EOMs	27
3.1.1	Derivation of Rotor Imbalance Disturbance Forces	27
3.1.2	ISS Disturbance Modeling	29
3.1.2.1	Sinusoidal Approximation of a Pulse Train.....	29
3.1.2.2	ISS Model 1: 4 ISS Disturbance States.....	31
3.1.2.3	ISS Model 2: 8 ISS Disturbance States.....	32
3.1.2.4	PSD Difference between Sinusoid and Pulse Train.....	33

3.2	Observability	36
3.2.1	PBH Criterion for Observability	37
3.2.2	Modal Criterion for Observability	39
3.2.3	Time Invariant Observability Test for Time Varying Dynamics	42
3.2.3.1	Observability of Plant Model	42
3.2.3.2	Observability of Filter Model	43
3.2.3.3	Example of Fully Observable Filter Model	44
3.2.3.4	Example of Unobservable Filter Model	45
3.2.4	Time Variant Observability Test	48
3.3	Introduction to Optimal Linear Filtering	50
3.4	Advanced Optimal Linear Filtering: The Kalman Filter	51
3.5	Initial Kalman Filter Parameter Calculations	63
4	Results	65
4.1	Performance Measures	65
4.1.1	Estimation Percent Amplitude Error	65
4.1.2	Error Duration	66
4.1.3	Estimation Error Standard Deviation Envelope	67
4.1.4	Time to Convergence	69
4.2	ISS Disturbance Models Used for Testing	70
4.3	ISS Model 1 Test: Performance	70
4.3.1	ISS Model 1 Test Set-Up	71
4.3.2	ISS Model 1 Test Results	75
4.3.3	ISS Model 2 Testing: Increased Disturbance Frequency Range Test	88

4.4	ISS Model 2 Test Set-Up.....	89
4.4.1	ISS Model 2 Test Results: Focusing on x and ϕ_y	94
4.4.2	ISS Model 2 Test Results: Focusing on y and ϕ_x	104
4.5	Monte Carlo Analysis: Robustness Test Set-Up	109
4.5.1	Monte Carlo Analysis: Parameter Uncertainty Results.....	110
4.5.2	Monte Carlo Analysis: Rotor Disturbance Amplitude Uncertainty Results ...	119
4.5.3	Monte Carlo Analysis: ISS Disturbance Frequency Uncertainty Results	121
4.5.4	Monte Carlo Analysis: Combination of All Uncertainties Results	123
5	Conclusions	125
6	References	128

List of Figures

Figure 1-1. Exploded Diagram of International Space Station Components [1].....	1
Figure 1-2. CAM Internal Components [2]	4
Figure 1-3. CR Components	5
Figure 1-4. Proper and Improper ABS Control with Using Relative Measurements	6
Figure 1-5. Overall CR System and Control.....	7
Figure 1-6. Open Loop System Used for Thesis.....	8
Figure 1-7. Possible Use of Inverse System ID for Estimation Process.....	9
Figure 2-1. VIM/Rotor Reference Frame	13
Figure 2-2. Simplified Model	15
Figure 2-3. Model Used for Derivation of X-translation and ϕ_y -rotation	16
Figure 2-4. External Disturbance Naming Convention	17
Figure 2-5. State Naming Convention	18
Figure 2-6. Naming Convention for Stiffness and Damping Values.....	18
Figure 2-7. Naming Convention for Mass and Inertia Values.....	18
Figure 2-8. Model Used for Derivation of Y-translation and ϕ_x -rotation.....	21
Figure 2-9. Frequency Response of Reduced System	24
Figure 3-1. Method Comparison with Standard Kalman Filter Formulation	26
Figure 3-2. Rotor-Fixed Rotational Reference Frame	27
Figure 3-3. PSD of Plant Output due to Pulse Train Input is Sinusoidal.....	29
Figure 3-4. Frequency Response Plots.....	30
Figure 3-5. Output PSD Differential Between and Sine and Pulse Train Inputs.....	34
Figure 3-6. Output PSD Results of Amplitude Ratio Sine and Pulse Train Inputs	35

Figure 3-7. PSD Ratio Over All ISS Frequencies for All ISS Disturbance Inputs.....	35
Figure 3-8. Plant Observability Test over the Entire Range of Spin Frequencies.....	43
Figure 3-9. Observability Test for All Time-Varying Dynamics Combinations.....	44
Figure 3-10. Numerical Solution for $\Phi(t,t_0)$	49
Figure 3-11. Discrete Kalman Filter Timing Diagram [23].....	58
Figure 3-12. Predictor - Corrector Model [26]	60
Figure 3-13. Block Diagram of Discrete System and State Estimator	61
Figure 3-14. Block Diagram Kalman Gain Computation.....	62
Figure 4-1. Example of Error Duration Performance Metric	66
Figure 4-2. Example Plot of Estimation Error and Error Standard Deviation Envelope for Excellent Estimation (100% within bounds).....	68
Figure 4-3. Example Plot of Estimation Error and Standard Deviation Envelope for Unacceptable Estimation (~40% within bounds).....	68
Figure 4-4. Time History Showing Convergence within 2.5 Seconds	69
Figure 4-5. Bode Plot Used to Determine Testing Frequencies	72
Figure 4-6. Amplitude Ratio Components.....	73
Figure 4-7. Flow Chart to Determine F_s Necessary for Desired Amplitude Ratios	73
Figure 4-8. Sensor Measurement x_{rel} Time History (left) and PSD (right).....	80
Figure 4-9. Results of Implementation of All Disturbance Models.....	81
Figure 4-10. Results of Implementation of Only Rotor Disturbance Model	81
Figure 4-11. Results of Implementation of Only ISS Disturbance Model	82
Figure 4-12. Results of Implementation of No Disturbance Models.....	82

Figure 4-13. Standard Deviation Envelope Resulting from Implementation of All Disturbance Models.....	84
Figure 4-14. Standard Deviation Envelope Resulting from Implementation of Only Rotor Disturbance Model	84
Figure 4-15. Standard Deviation Envelope from Implementation of Only ISS Disturbance Model	85
Figure 4-16 Standard Deviation Envelope from Implementation of No Disturbance Models	85
Figure 4-17. Duration of Error of x_r Estimation from Implementation of All Disturbance Models.....	86
Figure 4-18. Duration of Error of x_r Estimation from Implementation of Only Rotor Disturbance Model	86
Figure 4-19. Duration of Error of x_r Estimation from Implementation of Only ISS Disturbance Model	87
Figure 4-20. Duration of Error of x_r Estimation from Implementation of No Disturbance Models.....	87
Figure 4-21. Bode Plots Used For Rotor Disturbance Frequencies.....	89
Figure 4-22. Bode Plots Used For ISS Rotational Disturbance Center Frequencies.....	90
Figure 4-23. Testing Algorithm for Improving Operational Bandwidth	93
Figure 4-24. Logic Flow Diagram for Testing Regimen	94
Figure 4-25. Disturbance Frequencies Used when Focusing on x and ϕ_y	94
Figure 4-26. Time History of Actual, Estimated, and Error for x_r Using ISS Model 1	96
Figure 4-27. Time History of Actual, Estimated, and Error for x_r Using ISS Model 2	96

Figure 4-28. Estimation Error and Error Standard Deviation Envelope of x_r Estimation with ISS Model 1.....	97
Figure 4-29. Estimation Error and Error Standard Deviation Envelope of x_r Estimation with ISS Model 2.....	97
Figure 4-30. Duration of Error of x_r Estimation with ISS Model 1.....	98
Figure 4-31. Duration of Error of x_r Estimation with ISS Model 2	98
Figure 4-32. Time History of Actual, Estimated, and Error for x_r Using ISS Model 1 (with rotor spin-up).....	101
Figure 4-33. Time History of Actual, Estimated, and Error for x_r Using ISS Model 2 (with rotor spin-up).....	101
Figure 4-34. Estimation Error and Error Standard Deviation Envelope of x_r Estimation with ISS Model 1 (with rotor spin-up).....	102
Figure 4-35. Estimation Error and Error Standard Deviation Envelope of x_r Estimation with ISS Model 2 (with rotor spin-up).....	102
Figure 4-36. Duration of Error of x_r Estimation with ISS Model 1 (with rotor spin-up) ..	103
Figure 4-37. Duration of Error of x_r Estimation with ISS Model 2 (with rotor spin-up)...	103
Figure 4-38. Disturbance Frequencies used when focusing on y and ϕ_x	104
Figure 4-39. Time History of Actual, Estimated, and Error for y_r Using ISS Model 1	106
Figure 4-40. Time History of Actual, Estimated, and Error for y_r Using ISS Model 2.....	106
Figure 4-41. Estimation Error and Error Standard Deviation Envelope of y_r Estimation with ISS Model 1.....	107
Figure 4-42. Estimation Error and Error Standard Deviation Envelope of y_r Estimation with ISS Model 2.....	107

Figure 4-43. Duration of Error of y_r Estimation with ISS Model 1	108
Figure 4-44. Duration of Error of y_r Estimation with ISS Model 2	108
Figure 4-45. Distribution of Translational and Rotational Stiffness between Rotor and Shroud (top row) and Shroud and ISS Mass 1 (bottom row).....	111
Figure 4-46. Distribution of Translational and Rotational Stiffness between ISS Mass 1 and ISS Mass 2 (top row) and ISS Mass 2 and Inertial (bottom row)	111
Figure 4-47. Modal Frequency Distribution Caused by ΔK (for d_{xs} to x_{rel})	112
Figure 4-48. Modal Frequency Distribution Caused by ΔK (for d_{ys} to y_{rel})	113
Figure 4-49. Modal Frequency Distribution Caused by ΔK (for $d_{\phi xs}$ to ϕ_{xrel}).....	113
Figure 4-50. Modal Frequency Distribution Caused by ΔK (for $d_{\phi ys}$ to ϕ_{yrel}).....	114
Figure 4-51. Monte Carlo Results Testing Parameter Uncertainty (no spin-up).....	115
Figure 4-52. x_r Estimation.....	116
Figure 4-53. y_r Estimation.....	116
Figure 4-54. ϕ_{xr} Estimation	117
Figure 4-55. ϕ_{yr} Estimation	117
Figure 4-56. Monte Carlo Results Testing Parameter Uncertainty (with spin-up).....	118
Figure 4-57. Distribution of Rotor Disturbance Amplitude Parameters.....	119
Figure 4-58. Monte Carlo Results Testing Rotor Disturbance Amplitude Uncertainty (no spin-up).....	119
Figure 4-59. Monte Carlo Results Testing Rotor Disturbance Amplitude Uncertainty (with spin-up).....	120
Figure 4-60. Distribution of Translational and Rotational ISS Disturbance Frequencies .	121

Figure 4-61. Monte Carlo Results Testing ISS Disturbance Frequency Uncertainty (no spin up).....	121
Figure 4-62. Monte Carlo Results Testing ISS Disturbance Frequency Uncertainty (with spin up).....	122
Figure 4-63. Monte Carlo Results Testing Combination of All Uncertainties (no spin up)	123
Figure 4-64. Monte Carlo Results Testing Combination of All Uncertainties (with spin up)	124

List of Tables

Table 3-1. 1- Norm of the Columns of the Modal Observability Matrix (CT) for a Fully Observable Case	45
Table 3-2. Modal 1- Norm of the Columns of the Modal Observability Matrix (CT) for an Unobservable Case	46
Table 3-3. Rows of the T^{-1} Matrix which Account For Unobservable Z States	47
Table 3-4. Summary of Discrete Kalman Filter Equations [23]	59
Table 4-1. Testing Parameters Determined for Desired FR and AR	74
Table 4-2. Percent Amplitude Error in Estimation between a Filter Model with All Disturbances Modeled and a Filter Model with No Disturbance Modeling	75
Table 4-3. Comparison between Using All Disturbance Models and Only Rotor Disturbance Model: Test Results	76
Table 4-4. Comparison between Using All Disturbance Models and Only ISS Disturbance Model: Test Results	77
Table 4-5. Comparison between Using All Disturbance Models and Only ISS Disturbance Model: Test Results	78
Table 4-6. Performance Verification Test Case for x_r (AR = 1, FR = 0.9)	79
Table 4-7. Test Matrix	91
Table 4-8. Test Results Focusing on x and ϕ_y (no spin-up)	95
Table 4-9. Results Focusing on x and ϕ_y (with spin-up)	99
Table 4-10. Results Focusing on y and ϕ_x (no spin-up)	105
Table 4-11. Results Focusing on y and ϕ_x (with spin-up)	109

1 Introduction

The National Aeronautics and Space Administration (NASA), in association with the Japanese Aerospace Exploration Agency (JAXA), are building a Centrifuge Accommodation Module (CAM) for attachment onto the International Space Station (ISS). The CAM houses the Centrifuge Rotor (CR) and will be attached at node 2 on the International Space Station (ISS) as shown in Figure 1-1.

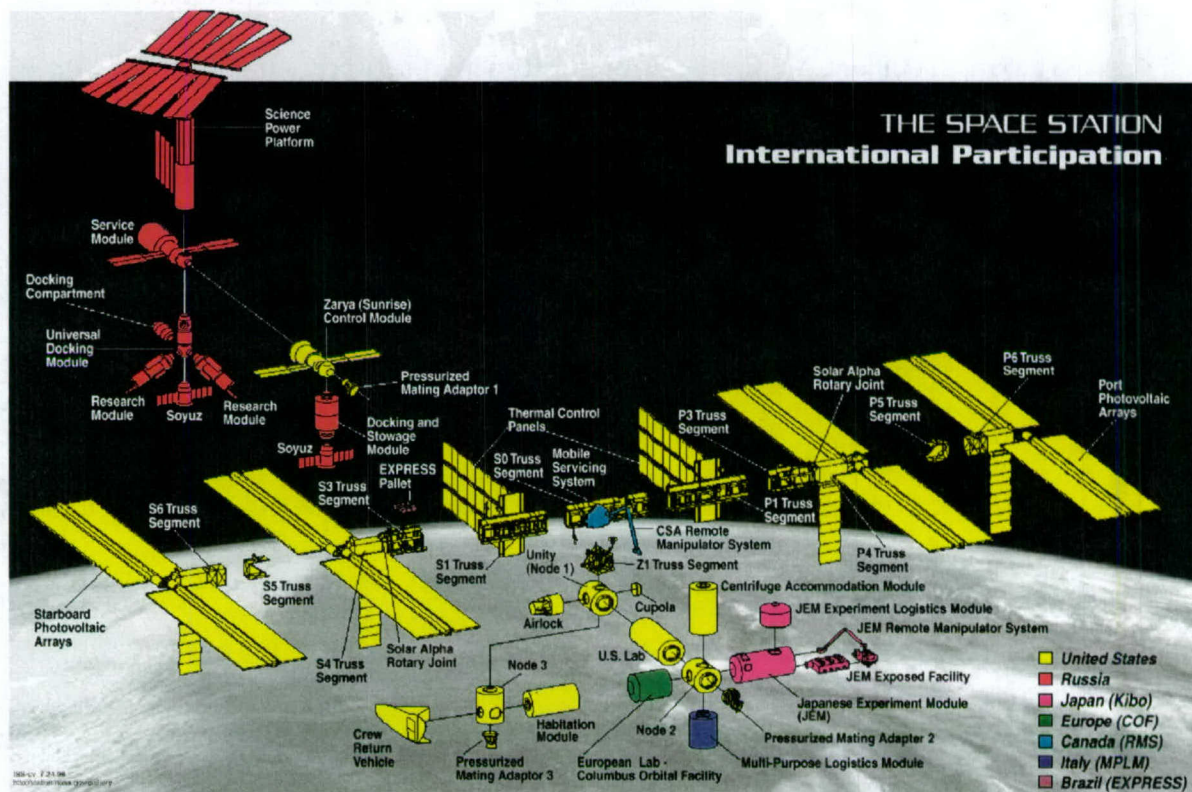


Figure 1-1. Exploded Diagram of International Space Station Components [1]

The CAM/CR is an orbiting laboratory which will study the effects of zero gravity and micro gravity environments on rodents. More details concerning the CAM/CR can be found in Section 1.1.

Before the CAM/CR can be attached to the ISS, all verification must be completed on the ground to ensure robust stability and safe operation. This is important not only to for increasing the probability of mission success, but also to make certain the safety of the ISS crew members. One issue concerning the safe operation of the CR aboard the ISS is the occurrence and the effect of rotor imbalances due to changing inertia during CR operation. The effect of rotor imbalances can be found in everyday life such as an unbalanced washing machine drum impacting the side of the washing machine or steering issues caused by unbalanced automotive tires. Although this problem may seem benign in the washing machine example, if the massive rotor in the CR impacts the CAM, critical damage to the ISS could result.

One method of solving this problem would be to use counterbalancing masses to cancel out any imbalances in the rotor. In the case of the CR, a system called the Auto Balancing System (ABS) employs this method. A problem occurs during implementation of the ABS due to the unavailability of measurements integral to ABS control, namely the rotor's absolute (i.e., relative to inertial space) states. These absolute rotor states cannot be obtained, because the displacement sensors are located in such a manner that only relative (i.e., between two moving masses) measurements are possible. Therefore an estimator is needed to estimate absolute rotor states from the relative measurements. This thesis proposes a method for estimating absolute rotor states from available relative/corrupt measurements involving the use of a Kalman filter. However using a standard Kalman filter formulation requires availability of both the rotor imbalance disturbances as well as the ISS thruster disturbances which are not available. This thesis will also discuss the

methods used to overcome this problem. Note that the words filter, observer, and estimator will be used interchangeably throughout the thesis.

Although the goal of this thesis is specific, the basic premise of the problem being solved is applicable to any field where there is a need to compute absolute measurements from relative and/or corrupt measurements with limited input knowledge. For example, state estimation would be helpful in many applications such as determining the core temperature of a nuclear reactor, where it is too hazardous for sensor location. This is accomplished with the use of thermodynamics and sensors placed in less intense locations [3]. Also, optimal filters are useful in the field of aeronautics when applied to estimation of turbine blade states through dynamics and inferior measurements [4].

1.1 Introduction to Centrifuge Accommodation Module (CAM)

The CAM, shown in Figure 1-2, which is composed of a life sciences glove box and freezer racks also houses the CR. The CR contains up to 4 habitats designed to house rodents. The CR will be used to study the long term effects of zero gravity and micro gravity environments on rodents. An artificial gravitational force of anywhere from 0 to 2 g can be generated by spinning the rotor anywhere from 0 and 1.4 Hz. The normal operational spin rate is 0.7 Hz, which is the spin rate necessary for 1 g.

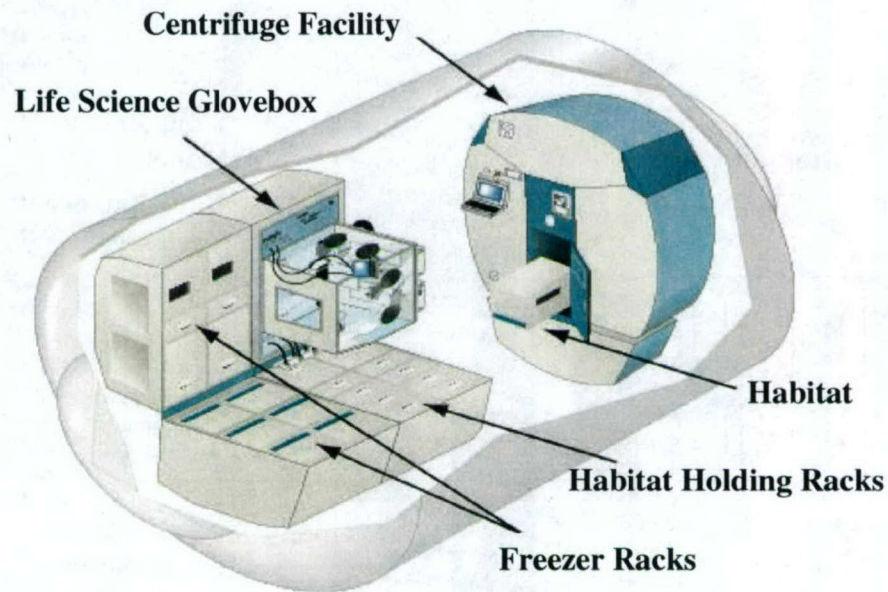


Figure 1-2. CAM Internal Components [2]

A rotor imbalance will occur whenever the spinning-member center of mass is not on the spin axis (e.g., due to location of rodents). Also a disturbance caused by the ISS jet-firing Attitude Control System will act on the rotor through the CAM shroud. Two separate systems, the Vibration Isolation Mechanism (VIM) and the Auto Balancing System (ABS) will be used to help minimize the rotor motion caused by these two disturbance sources. They are shown in Figure 1-3. Excessive rotor motion will result in snubber strikes against the shroud, causing the system to perform a safety shutdown.

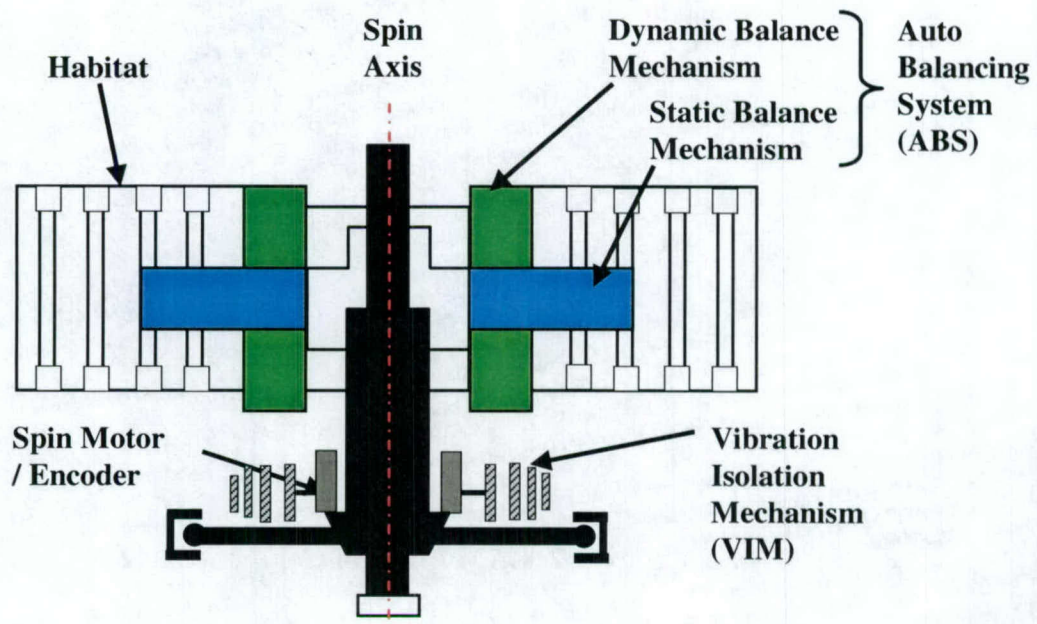


Figure 1-3. CR Components

The ABS controls the counter balancing masses which move in order to cancel out any rotor imbalance caused by rodent motion [5]. The sensors, which measure the motion of the rotor relative to the ISS, are located within the VIM. This relative measurement is the only available measurement with information of rotor motion.

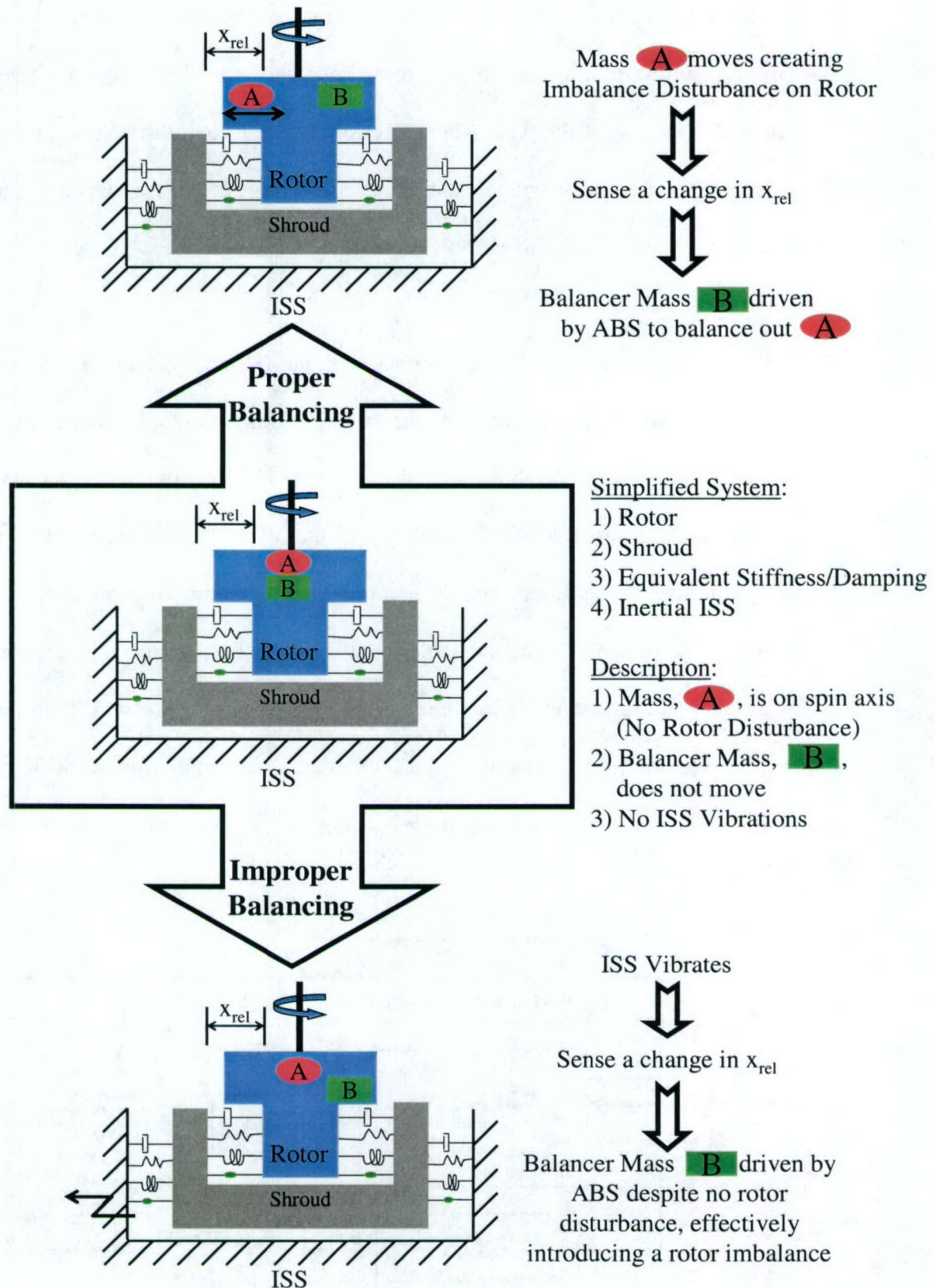


Figure 1-4. Proper and Improper ABS Control with Using Relative Measurements

By sensing only relative motion, if any ISS motion occurs, the relative measurement will not be the resulting motion due to pure rotor imbalance. In the case of a balanced rotor with only ISS motion, if the ABS were to act on the relative motion alone, it would drive the balancing mass away from the spin axis, effectively introducing an imbalance into a previously balanced rotor. This is shown in Figure 1-4.

The CR controls and sensors do not interface with the ISS controls and sensors. This lack of system interaction limits the amount of knowledge available for either system's controllers. The result is no direct knowledge of the ISS disturbance inputs which affect the relative measurement sensor located within the VIM. Also, since rodent motion is unpredictable and unmeasured, neither a rotor disturbance measurement, d_r , nor an ISS disturbance measurement, d_s , is available for use by the ABS controller or for use by the Kalman filter during state estimation. However, some rotor and ISS disturbance parameters (spin frequency, ISS disturbance characteristics, approximant rodent mass, etc.) are nominally known. Furthermore, the measurement, x_{rel} is corrupted by the addition of sensor noise, v_k .

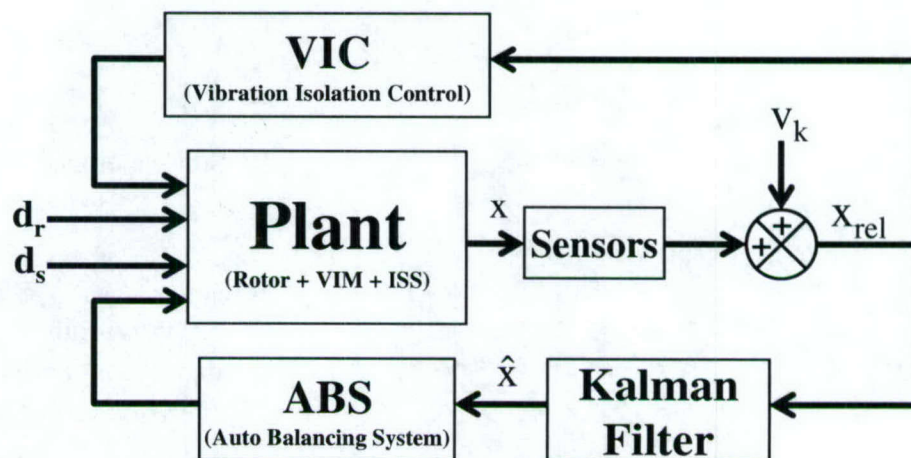


Figure 1-5. Overall CR System and Control

Since the main purpose of the VIM is to allow the rotor to follow the rigid body motion of the ISS while isolating rotor vibrations, a relative measurement is sufficient for the Vibration Isolation Controller (VIC) (see Figure 1-5); this can be achieved by ensuring there is no change in relative displacement. However, the main purpose of the ABS is to counterbalance any imbalance caused solely by rotor motion, therefore, a relative measurement is not sufficient. Instead, absolute rotor state information is necessary for proper ABS control. This leads to the central question addressed in this thesis; that is, “How do we calculate absolute rotor states from relative measurements, with only partial knowledge of the disturbance inputs into the system?” This thesis provides a method of state estimation through the use of a Kalman Filter applied to a plant model which has been augmented by disturbance states. A more in depth discussion on the system and the details of the CR example problem can be found in Chapter 2.

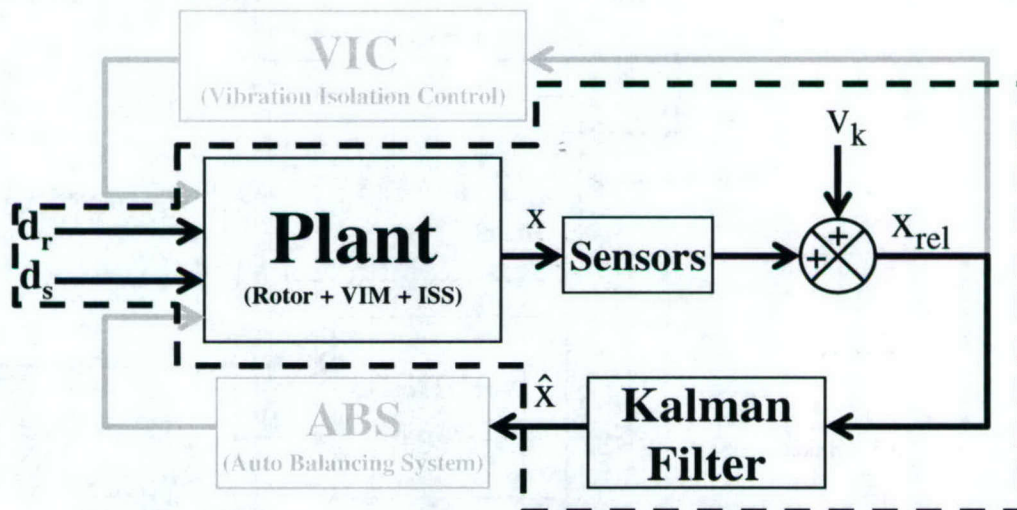


Figure 1-6. Open Loop System Used for Thesis

Since state estimation is the only operation of concern, the controllers in Figure 1-5 will be eliminated to create the open loop system found in Figure 1-6. This is the system used during the filter design process.

1.2 Alternative Estimation Options

One approach to resolve the lack of input knowledge is input reconstruction. Input reconstruction involves the use of the knowledge of the plant and the output time history to estimate the input, u , which in this case would include both rotor and ISS disturbances. This is also known as Inverse System Identification technique. This method may be helpful during state estimation, because if the inputs into the system can be reconstructed, then they can be used in the estimation process (see Figure 1-7).

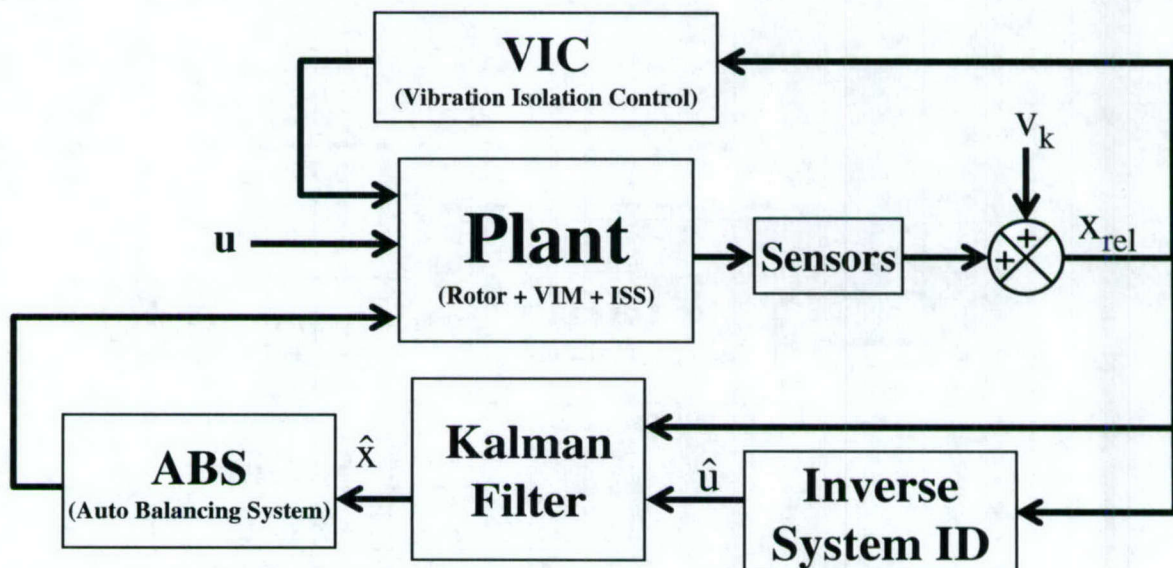


Figure 1-7. Possible Use of Inverse System ID for Estimation Process

A time domain method for estimating the applied forces on a structure was proposed by Stelzner, Kammer, and Milenkovic [6]. The method uses a non-causal moving average representation of the inverse structural system and has been successful in estimating the individual input forces for structures where the sensors are not collocated with the force input locations. The problem with the implementing of this method is that it only allows for *near*-real time estimation of the input forces, while the Kalman filter requires knowledge of real time input forces for proper estimation. Therefore, the approach suggested in Figure 1-7 cannot be used to solve the rotor estimation problem.

Another recently developed time domain Inverse System Identification method called the Sum of Weighted Accelerations Technique (SWAT) has been applied to many different impact problems [7]. The limitations of using SWAT lie in the fact that it can only reconstruct the sum of the external forces acting on a body's center of mass and not the individual applied forces. To overcome this shortcoming, Genaro and Rade created a variation of SWAT which would yield the input forces [8]. However, this process introduces a shortcoming of its own in the fact that the number of sensors must be equal to or be greater than the number of responding modes, which is not the case for the CR.

A further limitation of the input estimation or indirect force measurement techniques is that the process is found to be numerically ill-conditioned [9]. The numeric ill-conditioning occurs during calculations that require inverses of matrices which allows very small errors in measurements to result in large errors in estimated forces.

Another approach includes the use of general structured (GS) observers for state estimation during the case where inputs are unknown. A method for designing a full order unknown input observer (UIO) based on a GS observer is presented by Chang, You, and Hsu which allows for state estimation despite the existence of unknown inputs or uncertain disturbances [10]-[13]. However this method cannot be used for the CR problem since it requires the number of outputs (measurements) to be greater than the number of unknown inputs. For the CR problem, there are only 4 outputs versus the 8 possible inputs.

1.3 Thesis Overview and Content

Chapter 2 provides a problem overview and a concise description of the CR system. This description includes a list of assumptions made during problem formulation and the process used to create a simplified model, which includes the rotor, the shroud, and a two-mass ISS flex model, for analysis and testing purposes. Also, the reference frames used as well as the derivations of the equations of motion for the simplified system are presented.

Chapter 3 presents a detailed description of the proposed solution method by introducing a formulation of the disturbance models. The rotor disturbance is derived as a function of imbalance geometry, mass/inertia, and spin rate, while the ISS disturbance modeling is accomplished through a sinusoidal approximation of the effect of a pulse train through the system dynamics. Issues dealing with the peripheral effects of this sinusoidal approximation are examined along with both plant and filter system observability. Examples of both observable and unobservable filter models are presented using a modal form of the observability test. A time varying observability test is presented and used to

determine observability during cases of rotor spin-up and ISS operation. Also, the discrete Kalman filter equations and algorithm are introduced along with a method for calculating initial Kalman filter parameters.

Chapter 4 provides a summary of the testing conducted to analyze estimation capabilities using the solution method proposed in Chapter 3. A description of the different performance measures used to evaluate Kalman filter performance is given. These measures included percent amplitude error in estimation, error covariance standard deviation envelope, error duration, and time to convergence. Testing was conducted to evaluate the validity of the proposed solution method and to show improved performance through disturbance model expansion within the filter dynamics. Finally, Monte Carlo analysis was performed to show both robustness of the estimator as well as its sensitivity to different uncertainties. The following computer programs were used to run all simulations and to perform all data analysis: Matlab Version 6.5.1.199709 (R13SP1) and Simulink Version 5.5.1 (R13SP1+).

Chapter 5 provides a summary of the conclusions, along with a description of possible future work on the estimation process proposed in this thesis.

2 Problem Overview

This section provides a problem overview and a concise description of the CR system. This description includes a list of assumptions made during problem formulation and the process used to create a simplified model, which includes the rotor, the shroud, and a two-mass ISS flex model, for analysis and testing purposes. Also, the reference frames used as well as the derivations of the equations of motion for the simplified system are presented.

2.1 Modeling Assumptions

For design and verifications purposes, a simplified model consisting of the CR system on a flexible ISS platform was used (see Figure 2-1).

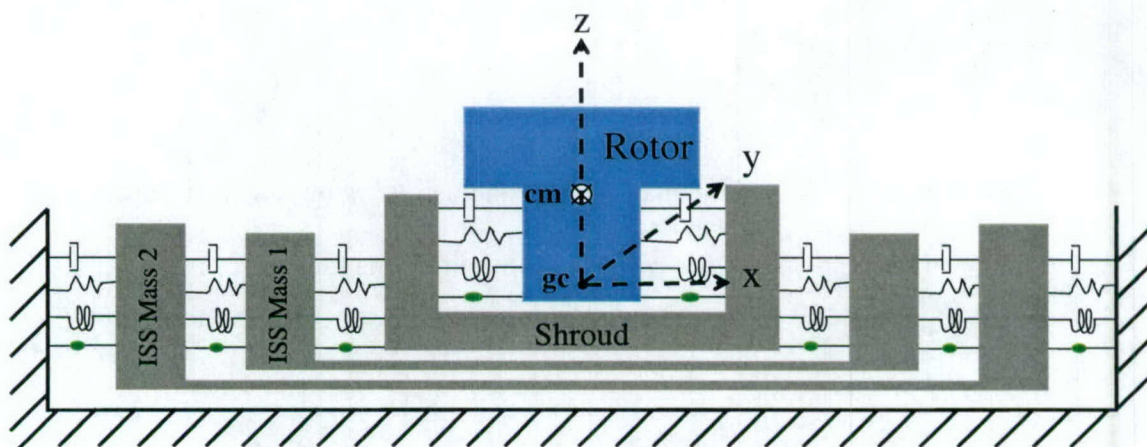


Figure 2-1. VIM/Rotor Reference Frame

During the modeling process, in order to simplify the problem all external forces on the ISS other than attitude control jet firings, such as gravity gradients, ISS Control Momentum Gyroscopes (CMG) torques, aerodynamic forces, and orbital effects were neglected. Secondly, all masses which make up the ISS, shroud, and rotor are considered to be rigid bodies. The rotor is assumed to be cylindrical and therefore symmetric about the axis of rotation. ISS flexibility was modeled using a two mass-spring-damper system. A nominal ISS configuration was used for the determination of mass and inertia values of the two mass ISS flex model created for testing purposes.

The origin of the reference frame is located at the geometric center, gc , which is the point on the x - y plane of the rotor through which all of the springs and dampers act. The gc is defined during equilibrium, and is the non-rotating inertial reference frame.

The center of mass, cm , of the shroud and ISS flex model masses are collocated with the cg , thus eliminating any coupling between translation and rotation in or about the x or y -axis between the shroud and ISS flex model. Only the rotor's static cm , noted on Figure 2-1, is located directly above the reference frame along the z -axis, which causes coupling in the translational and rotational equations of motion between the rotor and the shroud.

2.2 Derivation of the Linear, Time-Varying Equations of Motion

In this section, the equations of motion for the simplified model has been developed to include the rotor, the shroud, and a two-mass ISS flex model. Each of the four masses has 4 degrees of freedom (dofs) for a total of 16 dofs.

A cross-section of the model, in the x - z plane, that was used in the derivations of the equation of motion in x -axis is shown in Figure 2-2. This figure is not to scale.

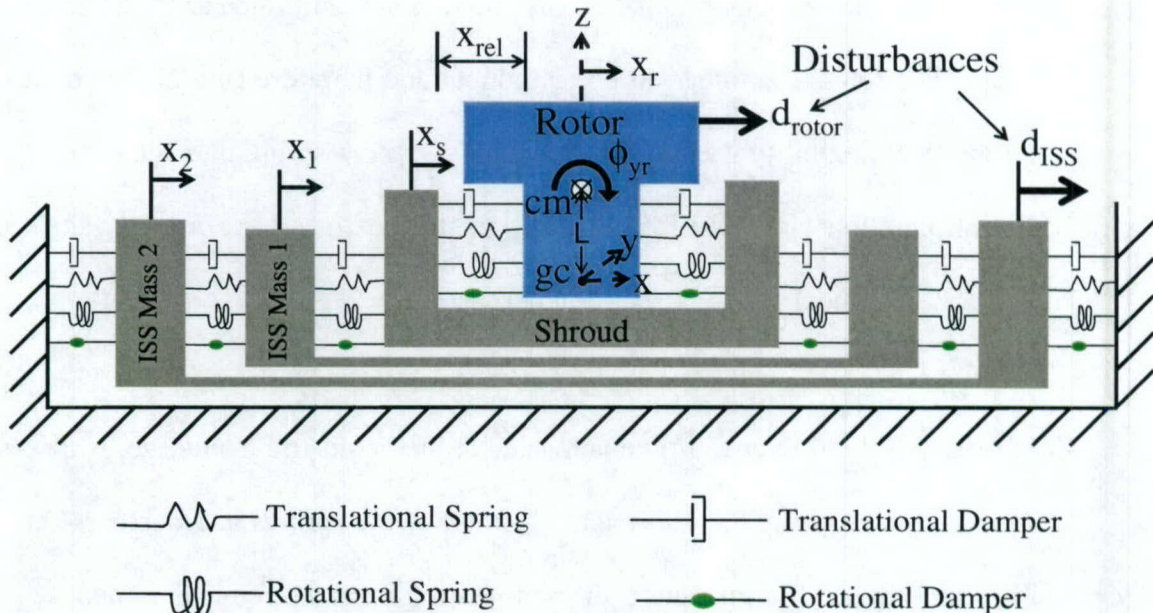


Figure 2-2. Simplified Model

Typical ISS flex modes, between ~ 0.01 and ~ 1.0 Hz, are captured by a two-mass ISS flex model, which attaches to the shroud through translational and rotational springs and dampers. Each of the four masses in this simplified model has two translational dofs (x and y -axis) and two rotational dofs (about x and y -axis), resulting in a model with 16 dofs. In addition, the disturbance on the rotor, d_{rotor} , caused by rodent motion during operation, acts on the rotor mass, while the disturbance on the ISS, d_{ISS} , caused by jet firings, acts on the outside mass of the ISS flex model. Note that the relative measurement, x_{rel} , is a relative measurement between the rotor and the shroud. The system is time varying due to variable rotor spin rate experienced during rotor spin-up and spin-down.

2.2.1.1 EOMs for x Translation

For the x translation equations of motion,

$$F = m\ddot{x} \quad (2-1)$$

where

$$\ddot{x}_r = \frac{1}{M_r} F_{rx}, \quad \ddot{x}_s = \frac{1}{M_s} F_{sx}, \quad \ddot{x}_1 = \frac{1}{M_1} F_{1x}, \text{ and } \ddot{x}_2 = \frac{1}{M_2} F_{2x} \quad (2-2)$$

The variable M represents each mass represented in the simplified model. The forces, F in equation (2-2), are provided by the springs, dampers, and external disturbance forces (See Figure 2-3). These forces are

$$\begin{aligned} F_{rx} &= -C_{Rtx} \dot{x}_r + C_{Rtx} \dot{x}_s + C_{Rtx} L \sin \phi_{y_r} - K_{Rtx} x_r + K_{Rtx} x_s + K_{Rtx} L \sin \phi_{y_r} + d_{x_r} \\ F_{sx} &= C_{Rtx} \dot{x}_r - (C_{Rtx} + C_{Ztx}) \dot{x}_s + C_{Ztx} \dot{x}_1 - C_{Rtx} L \sin \phi_{y_r} \\ &\quad + K_{Rtx} x_r - (K_{Rtx} + K_{Ztx}) x_s + K_{Ztx} x_1 - K_{Rtx} L \sin \phi_{y_r} \\ F_{1x} &= C_{Ztx} \dot{x}_s - (C_{Ztx} + C_{1tx}) \dot{x}_1 + C_{1tx} \dot{x}_2 + K_{Ztx} x_s - (K_{Ztx} + K_{1tx}) x_1 + K_{1tx} x_2 \\ F_{2x} &= C_{1tx} \dot{x}_1 - (C_{1tx} + C_{2tx}) \dot{x}_2 + K_{1tx} x_1 - (K_{1tx} + K_{2tx}) x_2 + d_{x_s} \end{aligned} \quad (2-3)$$

where external disturbance forces are defined by Figure 2-4,

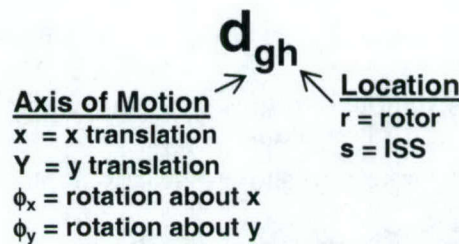


Figure 2-4. External Disturbance Naming Convention

The naming conventions for the states, the stiffness/damping values, and the mass/inertia values can be found in Figure 2-5, Figure 2-6 and Figure 2-7, respectively.

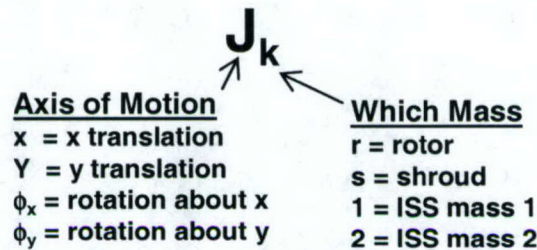


Figure 2-5. State Naming Convention

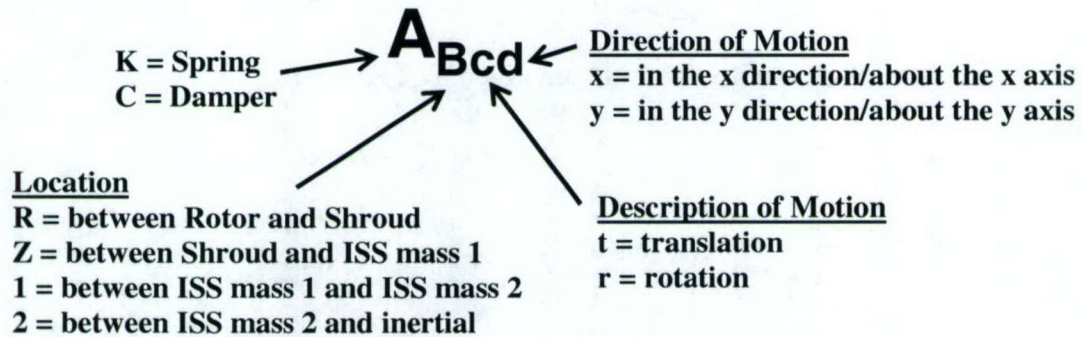


Figure 2-6. Naming Convention for Stiffness and Damping Values

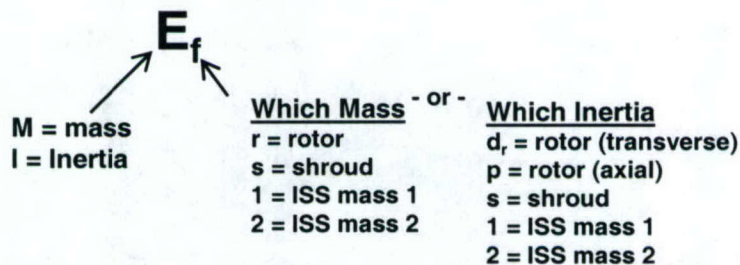


Figure 2-7. Naming Convention for Mass and Inertia Values

Assuming small angle rotations allow for linear but coupled equation for x translation given in equation (2-4). Substituting equation (2-3) into equation (2-2) gives

$$\begin{aligned}
 M_r \ddot{x}_r + C_{Rtx} \dot{x}_r - C_{Rtx} \dot{x}_s - C_{Rtx} L \dot{\phi}_{y_r} + K_{Rtx} x_r - K_{Rtx} x_s - K_{Rtx} L \phi_{y_r} &= d_{x_r} \\
 M_s \ddot{x}_s - C_{Rtx} \dot{x}_r + (C_{Rtx} + C_{Ztx}) \dot{x}_s - C_{Ztx} \dot{x}_1 + C_{Rtx} L \dot{\phi}_{y_r} \\
 - K_{Rtx} x_r + (K_{Rtx} + K_{Ztx}) x_s - K_{Ztx} x_1 + K_{Rtx} L \phi_{y_r} &= 0 \\
 M_1 \ddot{x}_1 - C_{Ztx} \dot{x}_s + (C_{Ztx} + C_{ltx}) \dot{x}_1 - C_{ltx} \dot{x}_2 - K_{Ztx} x_s + (K_{Ztx} + K_{ltx}) x_1 - K_{ltx} x_2 &= 0 \\
 M_2 \ddot{x}_2 - C_{ltx} \dot{x}_1 + (C_{ltx} + C_{2tx}) \dot{x}_2 - K_{ltx} x_1 + (K_{ltx} + K_{2tx}) x_2 &= d_{x_s}
 \end{aligned}
 \tag{ 2-4 }$$

2.2.1.2 EOMs for ϕ_y Rotation

The angular momentum equations, in the rotor body reference frame, provide the rotational equations of motion for the rotor are given by Yamamoto [15] [14] as

$$\begin{aligned}
 T_{\phi_{xr}} &= I_{d_r} \ddot{\phi}_{x_r} + I_p \omega \dot{\phi}_{y_r} \\
 T_{\phi_{yr}} &= I_{d_r} \ddot{\phi}_{y_r} - I_p \omega \dot{\phi}_{x_r} \\
 T_{\phi_{zr}} &= 0
 \end{aligned}
 \tag{ 2-5 }$$

where I_{d_r} is the transverse inertia for the rotor, I_p is the rotor spin axis inertia, ω is the rotor spin rate about the spin axis, and

$$\begin{aligned}
 T_{\phi_{xr}} &= -C_{Rty} L \dot{y}_r + C_{Rty} L \dot{y}_s - (C_{Rrx} + C_{Rty} L^2) \dot{\phi}_{x_r} + C_{Rrx} \dot{\phi}_{x_s} \\
 &\quad - K_{Rty} L y_r + K_{Rty} L y_s - (K_{Rrx} + K_{Rty} L^2) \phi_{x_r} + K_{Rrx} \phi_{x_s} + d_{\phi_{xr}}
 \end{aligned}
 \tag{ 2-6 }$$

and

$$\begin{aligned}
 T_{\phi_{yr}} &= +C_{Rtx} L \dot{x}_r - C_{Rtx} L \dot{x}_s - (C_{Rry} + C_{Rtx} L^2) \dot{\phi}_{y_r} + C_{Rry} \dot{\phi}_{y_s} \\
 &\quad + K_{Rtx} L x_r - K_{Rtx} L x_s - (K_{Rry} + K_{Rtx} L^2) \phi_{y_r} + K_{Rry} \phi_{y_s} + d_{\phi_{yr}}
 \end{aligned}
 \tag{ 2-7 }$$

Since the rest of the masses are not involved in rotations, then $\dot{H} = I\dot{\omega}$ can be used along with the small angle approximation to calculate linear but coupled equation for and ϕ_y rotation

$$\begin{aligned}
 I_{dr} \ddot{\phi}_{y_r} - I_p \omega \dot{\phi}_{x_r} - C_{Rtx} L \dot{x}_r + C_{Rtx} L \dot{x}_s + (C_{Rry} + C_{Rtx} L^2) \dot{\phi}_{y_r} - C_{Rry} \dot{\phi}_{y_s} \\
 - K_{Rtx} L x_r + K_{Rtx} L x_s + (K_{Rry} + K_{Rtx} L^2) \phi_{y_r} - K_{Rry} \phi_{y_s} = d_{\phi r} \\
 I_s \ddot{\phi}_{y_s} - C_{Rry} \dot{\phi}_{y_r} + (C_{Rry} + C_{Zry}) \dot{\phi}_{y_s} - C_{Zry} \dot{\phi}_{y_1} - K_{Rry} \phi_{y_r} + (K_{Rry} + K_{Zry}) \phi_{y_s} - K_{Zry} \phi_{y_1} = 0 \\
 I_1 \ddot{\phi}_{y_1} - C_{Zry} \dot{\phi}_{y_s} + (C_{Zry} + C_{1ry}) \dot{\phi}_{y_1} - C_{1ry} \dot{\phi}_{y_2} - K_{Zry} \phi_{y_s} + (K_{Zry} + K_{1ry}) \phi_{y_1} - K_{1ry} \phi_{y_2} = 0 \\
 I_2 \ddot{\phi}_{y_2} - C_{1ry} \dot{\phi}_{y_1} + (C_{1ry} + C_{2ry}) \dot{\phi}_{y_2} - K_{1ry} \phi_{y_1} + (K_{1ry} + K_{2ry}) \phi_{y_2} = d_{\phi s}
 \end{aligned} \tag{2-8}$$

The coupling occurs in the equation for the rotor motion due to the fact that the cm of the rotor is not collocated with the connection point of the springs/dampers. The distance, L, is used to account for translation in the x direction due to rotor rotation about the y axis at the cm and vice versa.

2.2.2 EOMs for Coupled y Translation and ϕ_x Rotation

The EOMs describing the y translational motion and the ϕ_x rotational motion of the simplified model were calculated using Figure 2-8.

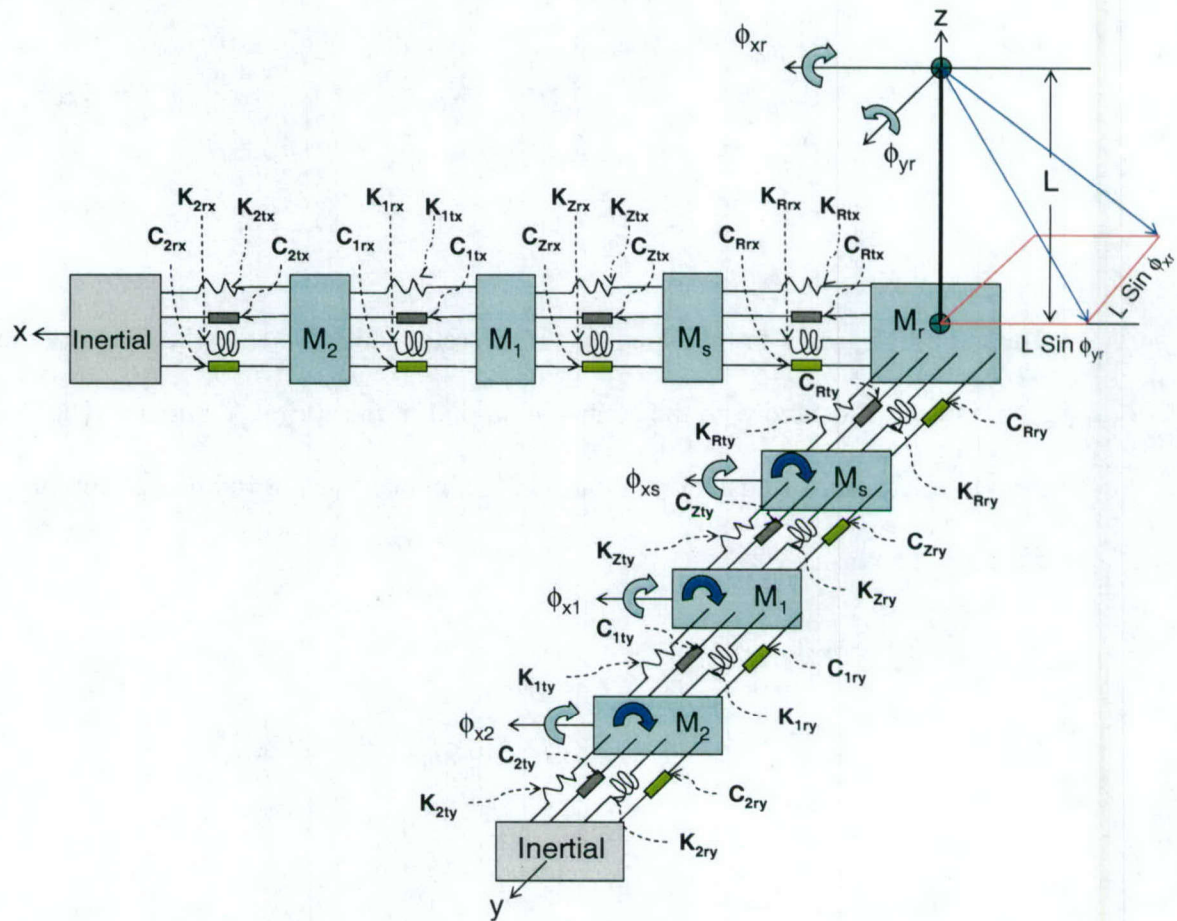


Figure 2-8. Model Used for Derivation of Y-translation and ϕ_x -rotation

2.2.2.1 EOMs for y Translation

For the y translation equations of motion,

$$F = m\ddot{y} \quad (2-9)$$

where

$$\ddot{y}_r = \frac{1}{M_r} F_{ry}, \quad \ddot{y}_s = \frac{1}{M_s} F_{sy}, \quad \ddot{y}_1 = \frac{1}{M_1} F_{1y}, \text{ and } \ddot{y}_2 = \frac{1}{M_2} F_{2y} \quad (2-10)$$

M represents each mass of the simplified model. The forces, F, are provided by the springs, dampers, and external disturbance forces (See Figure 2-8). These forces are

$$\begin{aligned} F_{ry} &= -C_{Rty} \dot{y}_r + C_{Rty} \dot{y}_s - C_{Rty} L \sin \dot{\phi}_{x_r} - K_{Rty} y_r + K_{Rty} y_s - K_{Rty} L \sin \phi_{x_r} + d_{y_r} \\ F_{sy} &= C_{Rty} \dot{y}_r - (C_{Rty} + C_{Zty}) \dot{y}_s + C_{Zty} \dot{y}_1 + C_{Rty} L \sin \dot{\phi}_{x_g} \\ &\quad + K_{Rty} y_r - (K_{Rty} + K_{Zty}) y_s + K_{Zty} y_1 + K_{Rty} L \sin \phi_{x_r} \\ F_{1y} &= C_{Zty} \dot{y}_s - (C_{Zty} + C_{1ty}) \dot{y}_1 + C_{1ty} \dot{y}_2 + K_{Zty} y_s - (K_{Zty} + K_{1ty}) y_1 + K_{1ty} y_2 \\ F_{2y} &= C_{1ty} \dot{y}_1 - (C_{1ty} + C_{2ty}) \dot{y}_2 + K_{1ty} y_1 - (K_{1ty} + K_{2ty}) y_2 + d_{y_s} \end{aligned} \quad (2-11)$$

Assuming small angle rotations allow for linear but coupled equation for y translation

$$\begin{aligned} M_r \ddot{y}_r + C_{Rty} \dot{y}_r - C_{Rty} \dot{y}_s + C_{Rty} L \dot{\phi}_{x_r} + K_{Rty} y_r - K_{Rty} y_s + K_{Rty} L \phi_{x_r} &= d_{y_r} \\ M_s \ddot{y}_s - C_{Rty} \dot{y}_r + (C_{Rty} + C_{Zty}) \dot{y}_s - C_{Zty} \dot{y}_1 - C_{Rty} L \dot{\phi}_{x_g} \\ &\quad - K_{Rty} y_r + (K_{Rty} + K_{Zty}) y_s - K_{Zty} y_1 - K_{Rty} L \phi_{x_r} = 0 \\ M_1 \ddot{y}_1 - C_{Zty} \dot{y}_s + (C_{Zty} + C_{1ty}) \dot{y}_1 - C_{1ty} \dot{y}_2 - K_{Zty} y_s + (K_{Zty} + K_{1ty}) y_1 - K_{1ty} y_2 &= 0 \\ M_2 \ddot{y}_2 - C_{1ty} \dot{y}_1 + (C_{1ty} + C_{2ty}) \dot{y}_2 - K_{1ty} y_1 + (K_{1ty} + K_{2ty}) y_2 &= d_{y_s} \end{aligned} \quad (2-12)$$

2.2.2.2 EOMs for ϕ_x Rotation

Since the rest of the masses are not involved in rotations, then $\dot{H} = I\dot{\omega}$ can be used along with the small angle approximation to calculate linear but coupled equation for and ϕ_x rotation

$$\begin{aligned}
 I_{d_r} \ddot{\phi}_{x_r} + I_p \omega \dot{\phi}_{y_r} + C_{Rty} L \dot{y}_r - C_{Rty} L \dot{y}_s + (C_{Rrx} + C_{Rty} L^2) \dot{\phi}_{x_r} - C_{Rrx} \dot{\phi}_{x_s} \\
 + K_{Rty} L y_r - K_{Rty} L y_s + (K_{Rrx} + K_{Rty} L^2) \phi_{x_r} - K_{Rrx} \phi_{x_s} = d_{\phi r} \\
 I_s \ddot{\phi}_{x_s} - C_{Rrx} \dot{\phi}_{x_r} + (C_{Rrx} + C_{Zrx}) \dot{\phi}_{x_s} - C_{Zrx} \dot{\phi}_{x_1} - K_{Rrx} \phi_{x_r} + (K_{Rrx} + K_{Zrx}) \phi_{x_s} - K_{Zrx} \phi_{x_1} = 0 \\
 I_1 \ddot{\phi}_{x_1} - C_{Zrx} \dot{\phi}_{x_s} + (C_{Zrx} + C_{1rx}) \dot{\phi}_{x_1} - C_{1rx} \dot{\phi}_{x_2} - K_{Zrx} \phi_{x_s} + (K_{Zrx} + K_{1rx}) \phi_{x_1} - K_{1rx} \phi_{x_2} = 0 \\
 I_2 \ddot{\phi}_{x_2} - C_{1rx} \dot{\phi}_{x_1} + (C_{1rx} + C_{2rx}) \dot{\phi}_{x_2} - K_{1rx} \phi_{x_1} + (K_{1rx} + K_{2rx}) \phi_{x_2} = d_{\phi s}
 \end{aligned} \tag{2-13}$$

Again, the coupling between the y and ϕ_x occurs from the distance L between the rotor cm and the location where the springs and dampers attach.

The time-varying aspect of the EOMs comes from the spin rate of the rotor, ω , (seen in equations (2-8) and (2-13)) which ramps up from 0 Hz to 0.7 Hz over a chosen time interval. Note that the z-axis translation of the VIM/CR is ignored since knowledge of the motion in the z direction is not necessary for control applications.

2.3 Model Frequency Response

Values for the various model parameters such as mass/inertia and stiffness/damping values, were selected to capture the expected physical system dynamics. Using these assumed values, the frequency response from all 8 disturbance forces to the corresponding 4 relative measurements was calculated and is shown in Figure 2-9.

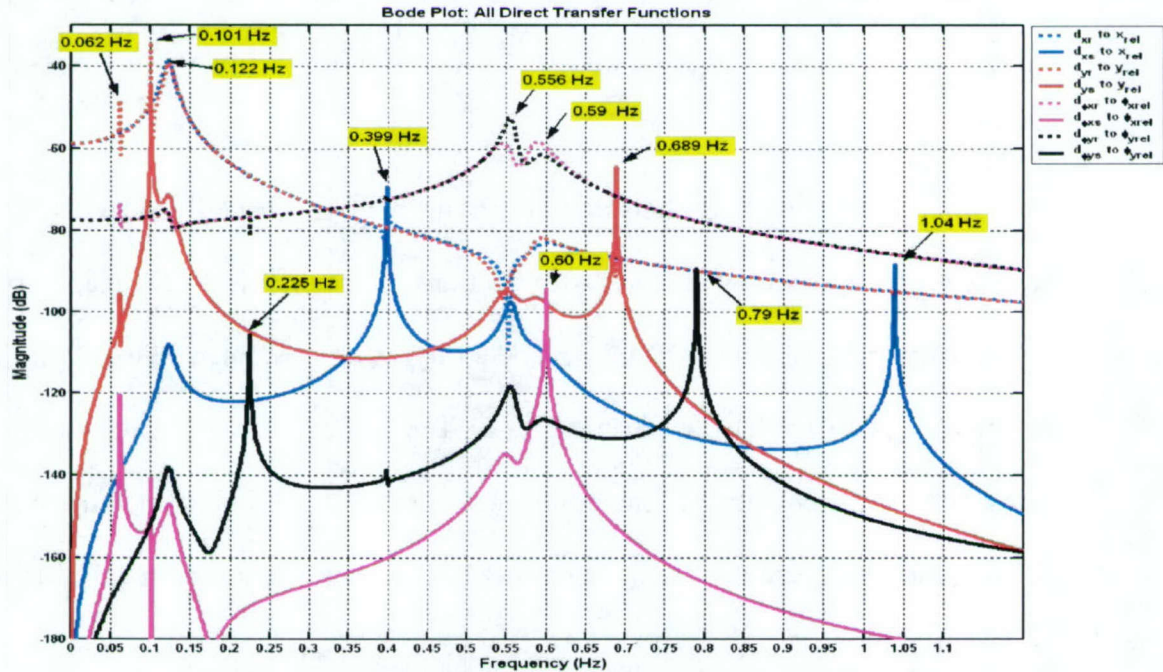


Figure 2-9. Frequency Response of Reduced System

The dashed lines show transfer functions including rotor disturbance inputs while the solid lines show transfer function including ISS disturbance inputs.

3 Solution Method

During the estimation of the centrifuge rotor states, two main problems are encountered. First, the deterministic plant inputs (4 rotor and 4 ISS disturbance inputs) are not available to the observer for use in the estimation algorithm. Secondly, the ISS disturbance inputs into the plant are applied in the form of a pulse train of jet/thruster firings rather than as a sinusoid disturbance. This could pose a problem for the chosen solution method and will be discussed later in this Chapter.

The first problem will be solved through the use of a plant model which has been augmented with disturbance states (See Sections 3.1.1 and 3.1.2). Estimation of the states for absolute rotor motion will be completed by using a Kalman Filter algorithm on this augmented plant model (See Section 3.4). The use of internal disturbance models will allow for estimation with a Kalman filter without the need for input measurements. This is vital to successful estimation, since normal Kalman filter operation requires knowledge of the inputs.

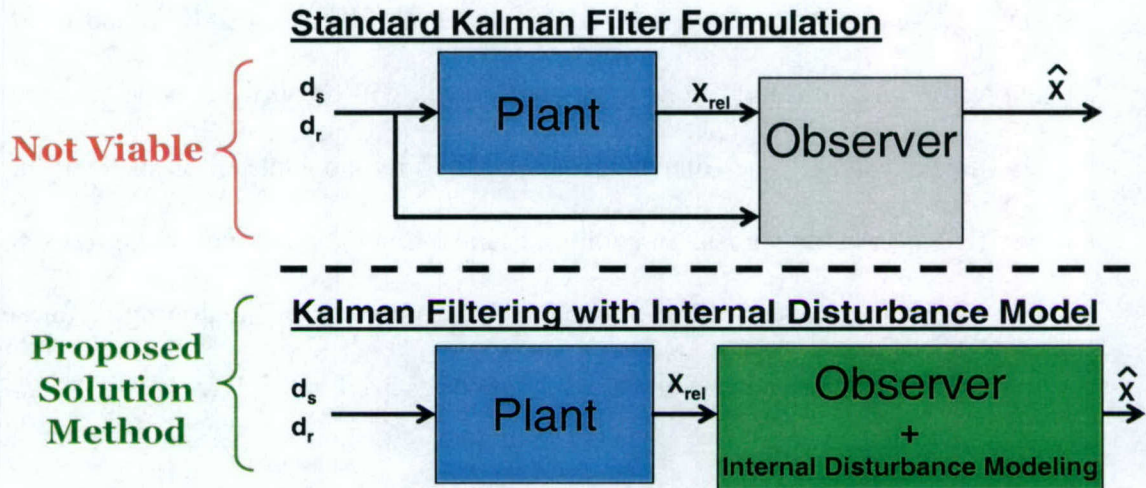


Figure 3-1. Method Comparison with Standard Kalman Filter Formulation

Figure 3-1 shows the difference between the standard Kalman filter formulation, which explicitly includes the known, deterministic inputs, and the method that is employed in this thesis, which instead models these inputs as additional filter states, to circumvent the fact that the disturbances are not available as inputs into the observer.

The second problem will be solved by using a sinusoidal approximation of the effect of the ISS pulse train disturbance on the plant dynamics, using only frequencies which result in a high gain through the plant. Frequencies where the plant attenuates the input signal are not important since they produce little effect on the measurement. Further explanation follows in Section 3.1.2.1.

3.1 Filter Model EOMs

The basic filter model, consisting of the rotor, VIM, and a 2-mass ISS flex model, has the same EOMs as the plant model (equations (2-4), (2-8), (2-12), and (2-13)), but to allow for variation, the filter model coefficients will be allowed to deviate from the plant coefficient values. The filter model is signified by the addition of an 'f' at the end of the coefficient variable names. In addition to modeling the plant within the filter, the rotor and ISS disturbances also need to be modeled. The process of integrating disturbance models into the filter model will be explained in Sections 3.1.1 and 3.1.2.

3.1.1 Derivation of Rotor Imbalance Disturbance Forces

The imbalance disturbance forces acting on the rotor have been derived as a function of the rotor mass, M_{rat} , the transverse and axial rotor inertias, I_{dr} and I_p , the distance of the center of mass (cm) from the spin axis, ϵ , the spin rate, ω , and the angle between the spin axis and the vector from the rotor tip to the rotor cm, α .

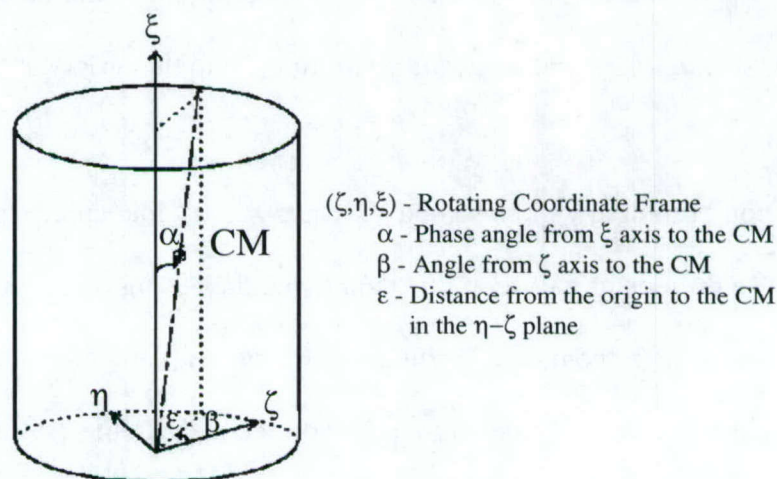


Figure 3-2. Rotor-Fixed Rotational Reference Frame

The value for the scalar parameters ε and α are used to defined a force vector in a rotor-fixed, rotating reference frame (η, ζ, ξ) , then rotated via a coordinate transformation, equation (3-1), back into the inertial reference frame (x, y, z) .

$$\begin{bmatrix} x \\ y \end{bmatrix} = \begin{bmatrix} \cos \theta & \sin \theta \\ -\sin \theta & \cos \theta \end{bmatrix} \begin{bmatrix} \eta \\ \zeta \end{bmatrix} \quad (3-1)$$

where θ equals $\omega_r t$. The rotor imbalance disturbance equation in the inertial reference frame is listed below [15].

$$\begin{aligned} d_{xr} &= M\varepsilon\omega_r^2 \cos(\omega_r t + \beta_r) & d_{\phi_{xr}} &= -(I_g - I_p)\alpha\omega_r^2 \sin(\omega_r t + \beta_r) \\ d_{yr} &= M\varepsilon\omega_r^2 \sin(\omega_r t + \beta_r) & d_{\phi_{yr}} &= (I_g - I_p)\alpha\omega_r^2 \cos(\omega_r t + \beta_r) \end{aligned} \quad (3-2)$$

Note that these imbalance disturbance forces and torques found in equation (3-2), are not available to the filter as inputs. These disturbances are modeled as second order oscillators of the form

$$\begin{aligned} \dot{z}_{1r} &= z_{2r} \\ \dot{z}_{2r} &= \omega_r^2 z_{1r} \end{aligned} \quad (3-3)$$

where the solutions to these differential equations are new states: z_{1r} and z_{2r}

$$\begin{aligned} z_{1r} &= \cos(\omega_r t + \beta_r) \\ z_{2r} &= -\sin(\omega_r t + \beta_r) \end{aligned} \quad (3-4)$$

Equations (3-2) can be rewritten in terms of these new disturbance states as

$$\begin{aligned} d_{xr} &= M\varepsilon\omega_r^2 z_{1r} & d_{\phi_{xr}} &= (I_g - I_p)\alpha\omega_r \dot{z}_{2r} \\ d_{yr} &= -M\varepsilon\omega_r^2 \dot{z}_{1r} & d_{\phi_{yr}} &= (I_g - I_p)\alpha\omega_r^2 z_{2r} \end{aligned} \quad (3-5)$$

Substituting these equations back into the equations of motion for the filter model results in a filter model with a state vector, x , of length 34 and of the form

$$x = [z \ \dot{z}]^T \quad z = [x_r \ x_s \ x_1 \ x_2 \ y_r \ y_s \ y_1 \ y_2 \ \phi_{x_r} \ \phi_{x_s} \ \phi_{x_1} \ \phi_{x_2} \ \phi_{y_r} \ \phi_{y_s} \ \phi_{y_1} \ \phi_{y_2} \ z_{1r}]$$

3.1.2 ISS Disturbance Modeling

The rotor imbalance disturbance is sinusoidal in nature due to rotor spin, while the ISS disturbance force is applied on the ISS in the form of jet impulses. The jet impulses result from the action of the ISS attitude control system [16]. The magnitude of the jet force is a constant, thus making the frequency of the jet firings and the overall on-time the only control variables.

3.1.2.1 Sinusoidal Approximation of a Pulse Train

The effect of the ISS pulse train disturbance input on the output of the plant can be represented by a Fourier series and its related fundamental frequency. A sinusoid of that fundamental frequency can be used to model the effect of the pulse train in the observer model. An example is shown in Figure 3-3 where a pulse train input at 0.399 Hz is applied to the plant, and the output is a sinusoid with a frequency of 0.399 Hz.

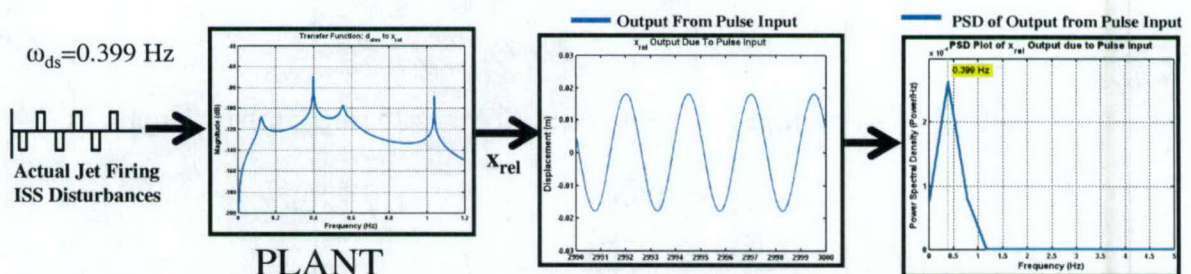


Figure 3-3. PSD of Plant Output due to Pulse Train Input is Sinusoidal

If the ISS pulse train disturbance excites the plant at a high gain frequency, then the output will have a large contribution as a result of the ISS disturbance. However, if the ISS pulse train disturbance excites the plant at a low gain frequency, then the output will have a small contribution resulting from the ISS disturbance. Therefore, it is important to determine the plant peak gain frequencies. These frequencies are determined from the frequency response plots (see Figure 3-4). These peak frequencies will now be used for ISS disturbance modeling within the filter. The discussion of the effect of the amplitude mismatch between the sinusoid and the jet firing will be conducted in Section 3.1.2.4.

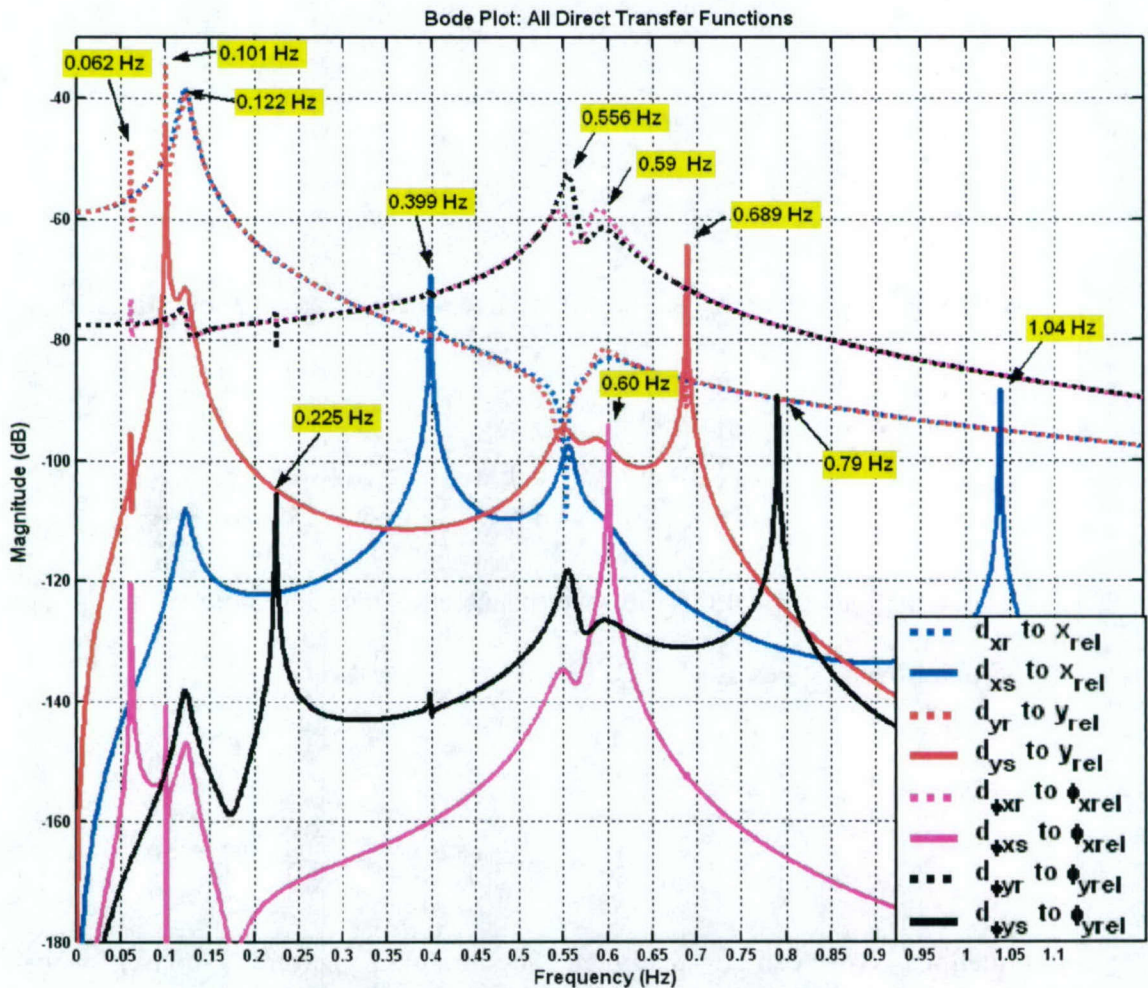


Figure 3-4. Frequency Response Plots

3.1.2.2 ISS Model 1: 4 ISS Disturbance States

Using the approach discussed in Section 3.1.2.1, an ISS disturbance model can be created representing the jet firing as a sinusoidal disturbance with single translational and single rotational disturbance frequency of ω_{dst} and ω_{dsr} , respectively, of the form:

$$\begin{aligned} d_{xs} &= F_x \cos(\omega_{dst}t + \beta_s) & d_{\phi s} &= -T_{\phi x} \sin(\omega_{dsr}t + \gamma_s) \\ d_{ys} &= F_y \sin(\omega_{dst}t + \beta_s) & d_{\phi y} &= T_{\phi y} \cos(\omega_{dsr}t + \gamma_s) \end{aligned} \quad (3-6)$$

The ISS disturbance amplitudes F_x , F_y , $T_{\phi x}$, and $T_{\phi y}$, are the known specifications of the thrusters located on the ISS. The ISS disturbance forces found in equations (3-6) are modeled as second order oscillators of the form

$$\begin{aligned} \dot{z}_{1s} &= z_{3s} \\ \dot{z}_{2s} &= z_{4s} \\ \dot{z}_{3s} &= -\omega_{dst}^2 z_{1s} \\ \dot{z}_{4s} &= -\omega_{dsr}^2 z_{2s} \end{aligned} \quad (3-7)$$

where the solutions to this set of differential equations are the new states: z_{1s} , z_{2s} , \dot{z}_{1s} , and \dot{z}_{2s} , where

$$\begin{aligned} z_{1s} &= \cos(\omega_{dst}t + B_s) & \dot{z}_{1s} &= -\omega_{dst} \sin(\omega_{dst}t + B_s) \\ z_{2s} &= \cos(\omega_{dsr}t + \gamma_s) & \dot{z}_{2s} &= -\omega_{dsr} \sin(\omega_{dsr}t + \gamma_s) \end{aligned} \quad (3-8)$$

Using equations (3-8) the ISS disturbance equations can be rewritten in term of the new ISS disturbance states as

$$\begin{aligned} d_{xs} &= F_x z_{1s} & d_{\phi s} &= \frac{T_{\phi x}}{\omega_{dsr}} \dot{z}_{2s} \\ d_{ys} &= -\frac{F_y}{\omega_{dst}} \dot{z}_{1s} & d_{\phi y} &= T_{\phi y} z_{2s} \end{aligned} \quad (3-9)$$

Equations (3-9) can be substituted back into the equations of motion for the filter model.

The resulting filter model has a state vector, \mathbf{x} , of length 38 of the form

$$x = [z \ \dot{z}]^T \quad z = [x_r \ x_s \ x_1 \ x_2 \ y_r \ y_s \ y_1 \ y_2 \ \phi_{x_r} \ \phi_{x_s} \ \phi_{x_1} \ \phi_{x_2} \ \phi_{y_r} \ \phi_{y_s} \ \phi_{y_1} \ \phi_{y_2} \ z_{1r} \ z_{2r} \ z_{1s} \ z_{2s}]$$

This ISS disturbance model will be called “ISS Model 1” for testing purposes.

3.1.2.3 ISS Model 2: 8 ISS Disturbance States

ISS Model 1 is expanded to create a new ISS disturbance model labeled “ISS Model 2”, which contains 8 ISS disturbance states for a total of 12 disturbance state, when including the rotor disturbance states. ISS Model 2 represents the ISS disturbance as sums of two sinusoidal disturbances, with two translational and two rotational disturbance frequencies of ω_{dst1} , ω_{dst2} , and ω_{dsr1} , ω_{dsr2} , respectively, of the form:

$$\begin{aligned} d_{xs1} &= F_{x1} \cos(\omega_{dst1}t + \beta_s) + F_{x2} \cos(\omega_{dst2}t + \beta_s) & d_{\phi s1} &= -T_{\phi x1} \sin(\omega_{dsr1}t + \gamma_s) - T_{\phi x2} \sin(\omega_{dsr2}t + \gamma_s) \\ d_{ys1} &= F_{y1} \sin(\omega_{dst1}t + \beta_s) + F_{y2} \sin(\omega_{dst2}t + \beta_s) & d_{\phi s1} &= T_{\phi y1} \cos(\omega_{dsr1}t + \gamma_s) + T_{\phi y2} \cos(\omega_{dsr2}t + \gamma_s) \end{aligned} \quad (3-10)$$

The two ISS disturbance amplitudes in each axis are assumed to equal the known specifications of the thrusters on the ISS (i.e. $F_x = F_{x1} = F_{x2}$, $F_y = F_{y1} = F_{y2}$, $T_{\phi x} = T_{\phi x1} = T_{\phi x2}$, and $T_{\phi y} = T_{\phi y1} = T_{\phi y2}$). The ISS disturbance forces found in equations (3-10) are modeled as second order oscillators of the form

$$\begin{aligned} \dot{z}_{1s} &= z_{5s} & \dot{z}_{5s} &= -\omega_{dst1}^2 z_{1s} \\ \dot{z}_{2s} &= z_{6s} & \dot{z}_{6s} &= -\omega_{dst2}^2 z_{2s} \\ \dot{z}_{3s} &= z_{7s} & \dot{z}_{7s} &= -\omega_{dsr1}^2 z_{3s} \\ \dot{z}_{4s} &= z_{8s} & \dot{z}_{8s} &= -\omega_{dsr2}^2 z_{4s} \end{aligned} \quad (3-11)$$

where the solutions to this set of differential equations are the new states: z_{1s} , z_{2s} , z_{3s} ,

z_{4s} , \dot{z}_{1s} , \dot{z}_{2s} , \dot{z}_{3s} , and \dot{z}_{4s} where

$$\begin{aligned}
z_{1s} &= \cos(\omega_{dst1}t + \beta_s) & \dot{z}_{1s} &= -\omega_{dst1} \sin(\omega_{dst1}t + \beta_s) \\
z_{2s} &= \cos(\omega_{dst2}t + \beta_s) & \dot{z}_{2s} &= -\omega_{dst2} \sin(\omega_{dst2}t + \beta_s) \\
z_{3s} &= \cos(\omega_{dsr1}t + \gamma_s) & \dot{z}_{3s} &= -\omega_{dsr1} \sin(\omega_{dsr1}t + \gamma_s) \\
z_{4s} &= \cos(\omega_{dsr2}t + \gamma_s) & \dot{z}_{4s} &= -\omega_{dsr2} \sin(\omega_{dsr2}t + \gamma_s)
\end{aligned} \tag{3-12}$$

The ISS force and torque inputs (3-10) can be rewritten in terms of the ISS disturbance states as

$$\begin{aligned}
d_{xs} &= F_{x1}z_{1s} + F_{x2}z_{2s} & d_{\phi xs} &= \frac{T_{\phi x1}}{\omega_{dsr1}} \dot{z}_{3s} + \frac{T_{\phi x2}}{\omega_{dsr2}} \dot{z}_{4s} \\
d_{ys} &= -\frac{F_{y1}}{\omega_{dst1}} \dot{z}_{1s} - \frac{F_{y2}}{\omega_{dst2}} \dot{z}_{2s} & d_{\phi ys} &= T_{\phi y1}z_{3s} + T_{\phi y2}z_{4s}
\end{aligned} \tag{3-13}$$

Equations (3-13) can be substituted back into the equations of motion for the observer model, increasing the number of states from 34 to 42. The resulting filter has a state vector, \mathbf{x} , of length 42 and is of the form

$$\mathbf{x} = [\mathbf{z} \ \dot{\mathbf{z}}]^T \quad \mathbf{z} = [x_r \ x_s \ x_1 \ x_2 \ y_r \ y_s \ y_1 \ y_2 \ \phi_{x_r} \ \phi_{x_s} \ \phi_{x_1} \ \phi_{x_2} \ \phi_{y_r} \ \phi_{y_s} \ \phi_{y_1} \ \phi_{y_2} \ z_{1r} \ z_{2r} \ z_{1s} \ z_{2s} \ z_{3s} \ z_{4s}]$$

3.1.2.4 PSD Difference between Sinusoid and Pulse Train

It is important to note that there is a power spectral density (PSD) difference in plant measurements (outputs) between a sinusoid disturbance and a pulse train disturbance; a sinusoidal disturbance of the same frequency as the pulse train with a small on-time creates an output with a higher PSD. The Kalman Filter determines the amplitude of the modeled disturbance sinusoid in order to get an equivalent sinusoid which would have created the same output as that from the pulse train input. Therefore, it is necessary to take into consideration the difference in the PSD during ISS disturbance state comparisons. Figure 3-5 illustrates the difference in the PSD of plant outputs when excited by a sinusoidal force

and a pulse train input force. The pulse on-time, defined as the duration per cycle for which the value is not equal to zero, is 20% of the period, and the frequencies of the sinusoid and the pulse train are the same.

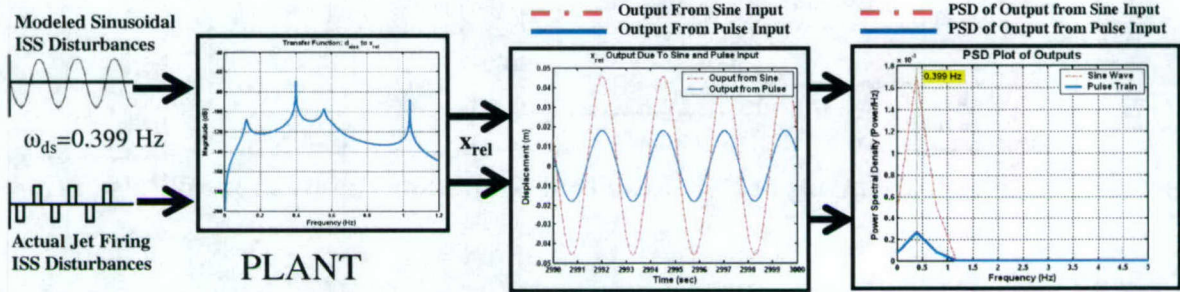


Figure 3-5. Output PSD Differential Between and Sine and Pulse Train Inputs

The power spectrum is generated by using a Fourier transform and taking the square of the magnitudes of the complex coefficients [17]. Therefore, the effect of using a pulse train rather than a sine wave can be calculated as:

$$PSD \text{ Ratio} = \frac{\sqrt{P_{\text{pulse}}}}{\sqrt{P_{\text{sine}}}} \quad (3-14)$$

where P_{sine} is the PSD due to the sine input at the excitation frequency (0.399 Hz in the example) and P_{pulse} is the PSD due to the pulse train input at the same excitation frequency.

For the example presented in Figure 3-5, the PSD ratio equals:

$$PSD \text{ Ratio} = \frac{\sqrt{P_{\text{pulse}}}}{\sqrt{P_{\text{sine}}}} = \frac{\sqrt{2.6435 * 10^{-4}}}{\sqrt{1.7073 * 10^{-3}}} = 0.3935$$

This result can be interpreted as the factor by which the original sinusoidal input amplitude would need to be multiplied by in order to get the equivalent plant output with a pulse train

input. By multiplying the original sinusoid by 0.3935, it can be shown that the PSD of the output is now exactly the same.

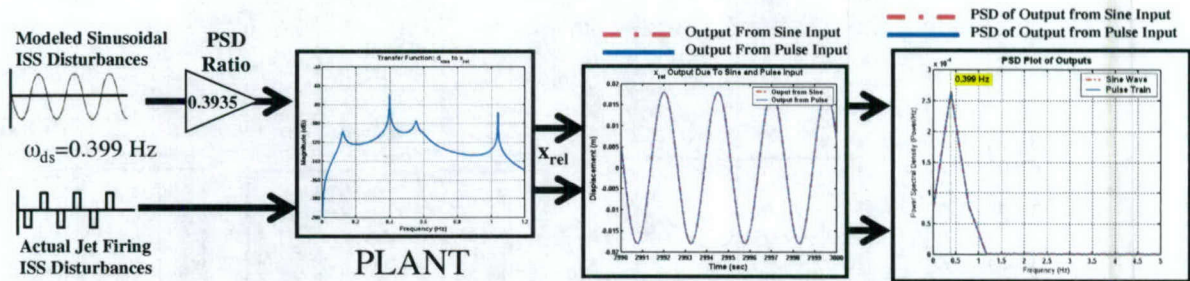


Figure 3-6. Output PSD Results of Amplitude Ratio Sine and Pulse Train Inputs

Since the ISS disturbance frequency could be any value between 0.01 Hz to 1 Hz, the entire range of frequencies was scanned to determine the actual equivalent disturbance PSD ratio for all ISS disturbance inputs.

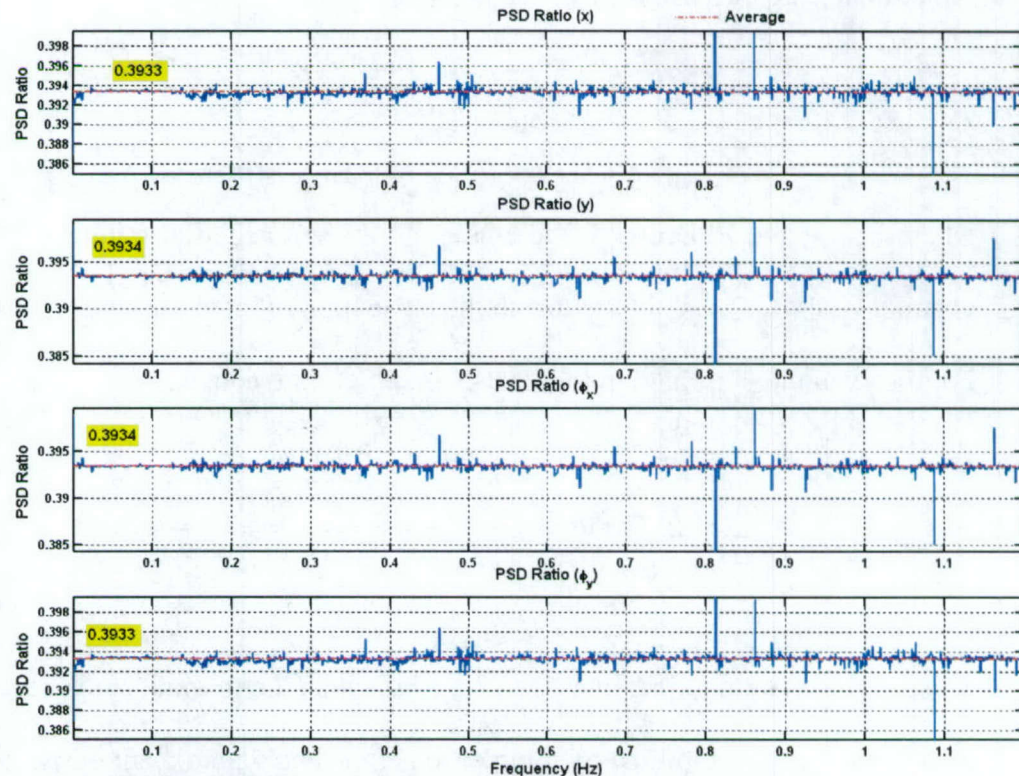


Figure 3-7. PSD Ratio Over All ISS Frequencies for All ISS Disturbance Inputs

The average PSD ratio over the range of possible ISS frequencies is equal to ~ 0.3933 for each disturbance input. Therefore, when comparing the disturbance state estimate to the actual disturbance state, the PSD ratio will have to be factored into the actual disturbance state amplitude. This is helpful in determining estimation performance.

3.2 Observability

Observability of the system is necessary in determining the viability of the Kalman filter as a solution method. The available methods used for determining plant observability include the well known Popov-Belevith-Hautus (PBH) Criterion [18]-[20] as well as a modal criterion for observability [21]. Both methods will be examined, but due to problems with ill-conditioning, the modal criterion for observability will be used to determine observability of the plant and filter models under time invariant conditions. A time varying observability test will be used to determine observability during operations such as rotor spin-up or spin-down and ISS maneuvering.

3.2.1 PBH Criterion for Observability

Consider a continuous time system described by

$$\dot{x} = Ax + Bu \quad (3-15)$$

$$y = Cx + Du \quad (3-16)$$

where x = state vector (n – vector)

y = output vector (m – vector)

A = System Dynamics ($n \times n$ matrix)

B = Input Matrix ($n \times r$ matrix)

C = Output Matrix ($m \times n$ matrix)

D = Direct Transmission Matrix ($m \times r$ matrix)

The solution to equation (3-15) is

$$x(t) = e^{At}x(0) + \int_0^t e^{A(t-\tau)}Bu(\tau)d\tau \quad (3-17)$$

and $y(t)$ is

$$y(t) = Ce^{At}x(0) + C \int_0^t e^{A(t-\tau)}Bu(\tau)d\tau + Du \quad (3-18)$$

Since the matrices A , B , C , and D are known and $u(t)$ is also known, then the last two terms on the right half side of equation (3-18) are known quantities. Therefore, they can be

subtracted from the observed value of $y(t)$, and it is sufficient to consider the unforced system described by

$$\dot{x} = Ax \quad (3-19)$$

$$y = Cx \quad (3-20)$$

Referring back to equations (3-17) and (3-18)

$$x(t) = e^{At}x(0) = \sum_{k=0}^{n-1} \alpha_k(t) A^k x(0) \quad (3-21)$$

and $y(t)$ is

$$y(t) = Ce^{At}x(0) = \sum_{k=0}^{n-1} \alpha_k(t) CA^k x(0) \quad (3-22)$$

For the system to be observable, given the output $y(t)$ over a time interval $0 \leq t \leq t_1$, $x(0)$ is uniquely determined from equation (3-22). It has been shown that for this to occur, the rank of the Observability matrix, O , of size $(n \times nm)$ must be full (i.e $\text{rank}(O) = n$). This is the so called PBH criterion for observability [18][19].

$$O = [C \quad CA \quad \dots \quad CA^{n-1}]^T \quad (3-23)$$

The problems with using the PBH criterion occur if some eigenvalues of A are greater than one while others are less than 1. Since the observability matrix, equation (3-23), requires A^{n-1} , then if the number of state, n , is large, then the observability matrix will become numerically ill-conditioned. The singular values less than 1 will trend towards zero while

the singular values greater than 1 become large and the value of n increases. Since the rank test is determined by the number of singular values above a certain tolerance (10^{-16} for Matlab rank command), as n approaches 32, the number of singular values which fall below the tolerance increases. Since the observability matrix requires A^{n-1} (A^{31} when using the plant dynamics), the rank of the observability matrix, is only 11; a rank of 32 is required for full rank.

The condition number, which is used to measure the level of ill-conditioning, is defined as the ratio of the maximum singular value to the minimum singular value. The larger the condition number, the more ill-conditioned the problem becomes. The observability matrix has a condition number of 3.432×10^{24} . This shows that with the parameters chosen for the example, a severe problem of ill-conditioning does exist. Therefore, an alternate method is needed to determine observability. The modal criterion for observability eliminates the need to compute high powers of the system dynamics.

3.2.2 Modal Criterion for Observability

The modal criterion for observability is described by Ogata [21]. Consider a system described by equations (3-19) and (3-20). Also suppose that the A matrix is diagonalizable with the use of a transformation matrix, T , such that

$$T^{-1}AT = \bar{A} \quad (3-24)$$

where \bar{A} is a diagonal matrix. Let us define

$$x = Tz \quad (3-25)$$

where z is the transformed state. In terms of the new transformed states, equations (3-19) and (3-20) become

$$\dot{z} = T^{-1}ATz = \bar{A}z \quad (3-26)$$

$$y = CTz \quad (3-27)$$

Using equations (3-21) and (3-22)

$$y(t) = CT e^{\bar{A}t} z(0) \quad (3-28)$$

or

$$y_k(t) = \sum_{i=1}^n (c_k^T T_i) e^{\lambda_i t} z_i(0) \quad (3-29)$$

where n equals the number of states, c_k^T denotes the k^{th} row in the C matrix, and λ_i denotes the i^{th} eigenvalue. If $c_k^T T_i = 0$ then the i^{th} mode is unobservable in the k^{th} output. If $CT_i = 0$ then the i^{th} mode is unobservable from all outputs.

In other words, the system is observable if none of the columns of the $m \times n$ matrix CT consist of all zero elements. This is easy to see, since with the decoupled dynamics, if the i^{th} column is found to be all zeros, then the corresponding state $z_i(0)$ will not be a part of the output equation.

If the system includes complex conjugate eigenvalues, then a modal A matrix can be created where the real eigenvalues appear on the diagonal of the matrix and the complex

conjugate eigenvalues appear in 2-by-2 blocks on the diagonal of the modal A matrix. For example, a system with eigenvalues $(\lambda_1, \lambda_2, \lambda_3)$, the modal A matrix is of the form

$$\bar{A} = \begin{bmatrix} \lambda_1 & 0 & 0 & 0 \\ 0 & \sigma & \omega & 0 \\ 0 & \omega & \sigma & 0 \\ 0 & 0 & 0 & \lambda_3 \end{bmatrix}$$

(3-30)

where $\sigma = \text{Re}(\lambda_2)$ and $\omega = \text{Im}(\lambda_2)$.

To test observability for complex conjugate eigenvalues, both the real and imaginary dot products must be zero for that mode to be unobservable. In this case, columns of all zeros in the CT matrix would come as single columns for real eigenvalues and as adjoining columns for complex conjugate pairs.

The modal condition for complete observability is also useful because using the inverse of the transform makes it possible to determine the combination of original states which cause the transformed state to be unobservable.

$$z = T^{-1}x$$

(3-31)

After determining which z states are unobservable by using the CT matrix, it is possible to determine the combination of x states which make up those unobservable z states by looking at the corresponding rows in the T^{-1} matrix.

3.2.3 Time Invariant Observability Test for Time Varying Dynamics

It is important to check observability of both the plant dynamics and the filter dynamics. If the plant is not observable, then the filter will be unable to produce accurate estimates of the plant states, even if the filter model is observable. On the other hand, if the filter model is not observable, then even if the plant is observable, the filter will be unable to produce accurate estimates. Therefore it is important to check the observability of both plant and filter models. Testing could require any combination of the time varying parameters (rotor spin rate and ISS disturbance frequencies) to be held as a constant value. Therefore, some assurance of observability is required over all possible combinations of time varying parameters.

3.2.3.1 Observability of Plant Model

The time varying components of the plant dynamics are simply functions of the rotor spin rate. In order to test the observability for all spin rates the modal observability test was performed on the plant dynamics with spin rates from 0.001 to 1 Hz, with a frequency step size of 0.001 Hz. If any of the columns of the CT matrix are all zeros (or less than a tolerance of 10^{-5}) then the system is considered unobservable. A observability plot (Figure 3-8), where 1 means that the system is observable at the given spin frequency, shows that the plant is observable for the entire range of spin rates.

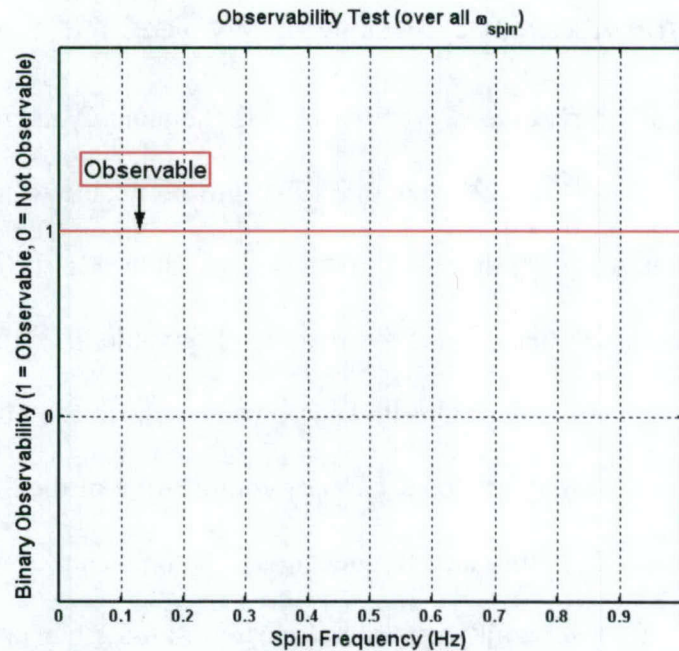


Figure 3-8. Plant Observability Test over the Entire Range of Spin Frequencies

3.2.3.2 Observability of Filter Model

The time varying components of the filter dynamics are simply functions of the rotor spin rate and the ISS disturbance frequencies. ISS disturbance frequencies were assumed to have a range of 0 to 1.2 Hz and were discretized with a frequency step size of 0.001 Hz. In order to test the observability of the filter model, the modal observability test was computed using the filter dynamics for every possible combination of time varying terms (i.e. each disturbance frequency was tested for a given spin frequency). If any of the columns of the CT matrix were all zeros (or less than a tolerance of 10^{-5}) then the system would be considered unobservable. Figure 3-9 below shows that filter dynamics are unobservable only during extremely low spin frequencies (below 0.015 Hz). This is not of concern for two main reasons: 1) At such a low spin frequency, the rotor imbalance force will be negligible and 2) Since the rotor spins up from 0 to 0.7 Hz, the spin frequency will

be under 0.015 Hz for less than 7 seconds, assuming a 300 second ramp up period, therefore the system will only be unobservable for a very short duration (see Figure 3-9).

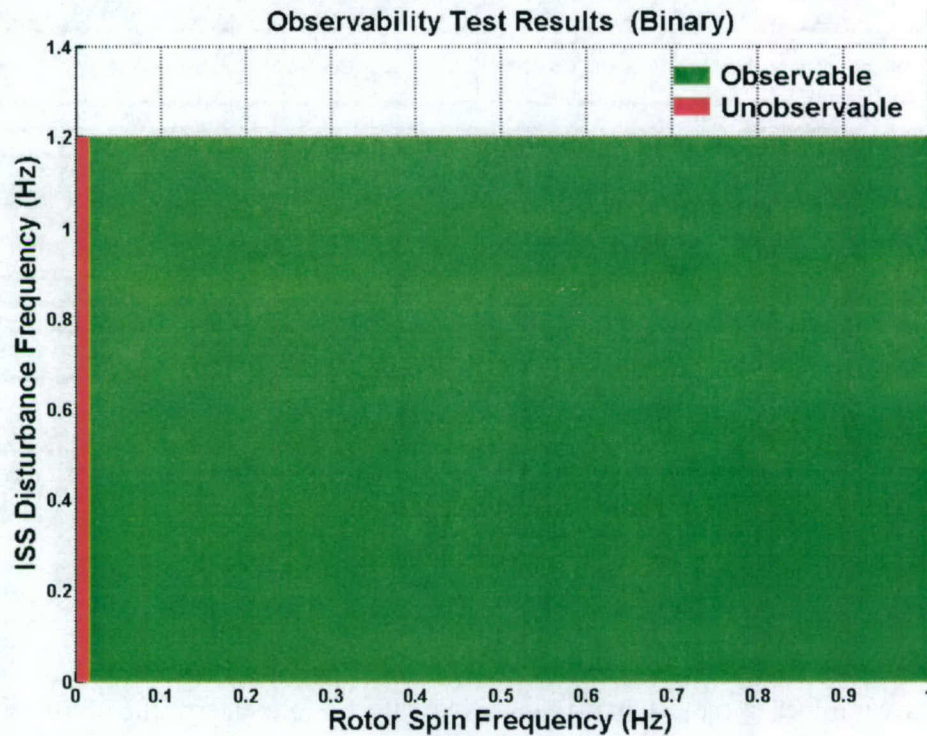


Figure 3-9. Observability Test for All Time-Varying Dynamics Combinations

3.2.3.3 Example of Fully Observable Filter Model

The following are the results of the modal observability test for a fully observable case ($\omega_r = 0.7$ Hz and all $\omega_{ds} = 0.4$ Hz). The 1-norm of each column of the CT matrix was taken to simplify data interpretation.

	1	2	3	4	5	6	7	8	9	10
Eigenvalues of A matrix	-0.11682 + 10.424i	-0.11682 - 10.424i	-0.073389 + 10.317i	-0.073389 - 10.317i	-0.18089 + 7.6069i	-0.18089 - 7.6069i	-7.3227e-5 + 6.5262i	-7.3227e-5 - 6.5262i	-2.3473e-5 + 4.9663i	-2.3473e-5 - 4.9663i
Norm of Columns of CT (w/Tolerance)	0.09188	0.09210	0.07381	0.07412	0.08462	0.08461	0.00184	0.01591	0.01150	0.02006
	11	12	13	14	15	16	17	18	19	20
Eigenvalues of A matrix	-0.0014442 + 4.3275i	-0.0014442 - 4.3275i	-0.062997 + 3.5895i	-0.062997 - 3.5895i	-0.063107 + 3.5478i	-0.063107 - 3.5478i	-0.0026649 + 2.5059i	-0.0026649 - 2.5059i	-1.877e-5 + 3.7725i	-1.877e-5 - 3.7725i
Norm of Columns of CT (w/Tolerance)	0.01318	0.19392	0.03083	0.31019	0.04175	0.29286	0.04339	0.37691	0.00210	0.00364
	21	22	23	24	25	26	27	28	29	30
Eigenvalues of A matrix	-0.043358 + 1.619i	-0.043358 - 1.619i	-0.0046068 + 1.3913i	-0.0046068 - 1.3913i	-0.00016548 + 0.38928i	-0.00016548 - 0.38928i	-0.036858 + 0.78154i	-0.036858 - 0.78154i	-0.033126 + 0.76038i	-0.033126 - 0.76038i
Norm of Columns of CT (w/Tolerance)	0.40752	0.40720	0.42679	0.37970	0.44470	0.19488	0.71313	0.37802	0.76313	0.41044
	31	32	33	34	35	36	37	38		
Eigenvalues of A matrix	-0.0012268 + 0.63498i	-0.0012268 - 0.63498i	5.5511e-17 + 3.7699i	5.5511e-17 - 3.7699i	7.0777e-16 + 0.6346i	7.0777e-16 - 0.6346i	0 + 4.3982i	0 - 4.3982i		
Norm of Columns of CT (w/Tolerance)	0.50741	0.07915	0.00007	0.00003	0.37055	0.05411	0.00119	0.00118		

Table 3-1. 1- Norm of the Columns of the Modal Observability Matrix (CT) for a Fully Observable Case

Any number in the CT matrix that is less than a tolerance value of 10^{-5} was set to zero. The 1-norm of the rows of the CT matrix, shown in Table 3-1, contains no zero values and is therefore fully observable.

3.2.3.4 Example of Unobservable Filter Model

The following are the results of the modal observability test for an unobservable case ($\omega_r = 0.01$ Hz and all $\omega_{ds} = 0.7$ Hz). Similar to the observable test case, the 1-norm of each column of the CT matrix was taken to simplify data interpretation.

	1	2	3	4	5	6	7	8	9	10
Eigenvalues of A matrix	-0.0805 + 10.336i	-0.0805 - 10.336i	-0.0801 + 10.335i	-0.0801 - 10.335i	-7.38e-005 + 6.5262i	-7.38e-005 - 6.5262i	-3.33e-005 + 4.9663i	-3.33e-005 - 4.9663i	-0.00149 + 4.3278i	-0.00149 - 4.3278i
Norm of Columns of CT (w/Tolerance)	0.06352	0.08756	0.06335	0.08746	0.00076	0.01465	0.00364	0.04355	0.01654	0.18903
	11	12	13	14	15	16	17	18	19	20
Eigenvalues of A matrix	-0.00213 + 2.5051i	-0.00213 - 2.5051i	-0.0977 + 3.3792i	-0.0977 - 3.3792i	-0.0663 + 3.4423i	-0.0663 - 3.4423i	-0.128 + 3.6429i	-0.128 - 3.6429i	-0.0906 + 3.6235i	-0.0906 - 3.6235i
Norm of Columns of CT (w/Tolerance)	0.01778	0.35617	0.13410	0.22749	0.10347	0.24106	0.10366	0.24204	0.05677	0.26287
	21	22	23	24	25	26	27	28	29	30
Eigenvalues of A matrix	-0.000217 + 1.4112i	-0.000217 - 1.4112i	-2.07e-005 + 3.7725i	-2.07e-005 - 3.7725i	-0.0351 + 0.7686i	-0.0351 - 0.7686i	-0.0364 + 0.78016i	-0.0364 - 0.78016i	-0.00014 + 0.39094i	-0.00014 - 0.39094i
Norm of Columns of CT (w/Tolerance)	0.01993	0.07976	0.01219	0.01677	0.73708	0.00972	0.75301	0.01150	0.40435	0.00686
	31	32	33	34	35	36	37	38		
Eigenvalues of A matrix	-0.0011 + 0.63506i	-0.0011 - 0.63506i	6.24e-017 + 3.7699i	6.24e-017 - 3.7699i	2.44e-016 + 0.062832i	2.44e-016 - 0.062832i	1.38e-016 + 0.6346i	1.38e-016 - 0.6346i		
Norm of Columns of CT (w/Tolerance)	0.45802	0.03761	0.00032	0.00024	0	0	0.33446	0.04833		

Table 3-2. Modal 1- Norm of the Columns of the Modal Observability Matrix (CT) for an Unobservable Case

Also, the same 10^{-5} tolerance was used in order to determine zero values. The table including the 1-norm of the columns of the CT matrix, shown in Table 3-2, does contain values of zero. Therefore, zero column vectors exist in the CT matrix, resulting in transformed states 37 through 40 being unobservable. Equation (3-31) is used to solve for the x state combinations which result in the unobservable transformed states. The rows of the T^{-1} matrix which account for the unobservable transformed states can be found in Table 3-3 below. The x state combinations which make up the z states can be calculated using Table 3-3.

	x state	x states 1-16	17	x states 18-35	36	x states 37,38
			z_{1r}		\dot{z}_{1r}	
z state	z_{35}	0	1.002	0	0	0
	z_{36}		0		15.947	

Table 3-3. Rows of the T^{-1} Matrix which Account For Unobservable Z States

Therefore,

$$z_{35} = 1.002 z_{1r}$$

$$z_{36} = 15.947 \dot{z}_{1r}$$

This shows that none of the rotor disturbance states can be observed at low spin rates. This finding is reasonable because since the rotor disturbance amplitude is a function of the square of the spin rate, ω_r^2 , a small spin rate would equal a very small disturbance amplitude; essentially, there is nothing to be observed.

3.2.4 Time Variant Observability Test

Under conditions of spin-up or ISS maneuvering, the time invariant observability test is not sufficient in determining observability. An observability test is required which takes into account the time-varying system dynamics. Gelb discusses observability under the assumption of a time-invariant system [23], however, his approach applies to time-varying systems as well. Consider the discrete system

$$\dot{x} = Ax, \quad x(t_0) = x_0 \quad (3-32)$$

$$y = Cx \quad (3-33)$$

The solution to (3-32) is

$$x(t) = \Phi(t, t_0) x_0 \quad (3-34)$$

where $\Phi(t, t_0)$ is the solution to the matrix differential equation

$$\frac{d}{dt}(\Phi(t, t_0)) = A(t)\Phi(t, t_0) \quad (3-35)$$

where

$$\Phi(t_0, t_0) = I \quad (3-36)$$

Using equations (3-33) and (3-35)

$$\begin{aligned}
 y(t_0) &= C(t_0)\Phi(t_0, t_0)x_0 = C(t_0)x_0 \\
 y(t_1) &= C(t_1)\Phi(t_1, t_0)x_0 \\
 y(t_2) &= C(t_2)\Phi(t_2, t_0)x_0 \\
 &\vdots \\
 y(t_{n-1}) &= C(t_{n-1})\Phi(t_{n-1}, t_0)x_0
 \end{aligned}$$

(3-37)

or

$$\begin{bmatrix} y(t_0) \\ y(t_1) \\ \vdots \\ y(t_{n-1}) \end{bmatrix} = \begin{bmatrix} C(t_0) \\ C(t_1)\Phi(t_1, t_0) \\ \vdots \\ C(t_{n-1})\Phi(t_{n-1}, t_0) \end{bmatrix} \underbrace{x_0}_{\substack{n \times 1}}$$

$Z: n \times m \times n$

(3-38)

where n is the number of states and m is the number of measurements. The condition for which x_0 is observable for the measurement times t_0, t_1, \dots, t_{n-1} is that

$$\text{rank}(Z) = n$$

(3-39)

Matlab and Simulink can be used to numerically calculate $\Phi(t, t_0)$, using the following algorithm

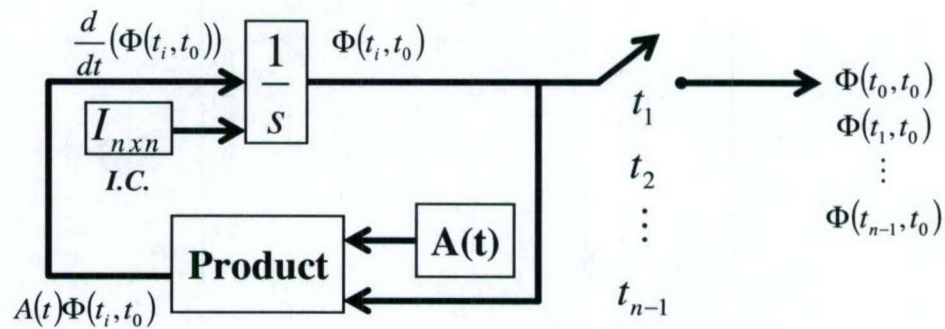


Figure 3-10. Numerical Solution for $\Phi(t, t_0)$

where $A(t)$ is the time varying dynamics and the Φ matrices are captured at each time step,

i. Using the algorithm described in Figure 3-10 and equation (3-38), the plant, the filter using ISS Model 1, and the filter using ISS Model 2 are all full rank and therefore conditionally observable.

3.3 Introduction to Optimal Linear Filtering

Now that it has been proven that the system is observable, a filter can be used to estimate the necessary rotor states. The term *filter* refers to the estimation of state at the present moment using previous measurements. An *unbiased* estimate is one whose expected value is the same as the expected value of the quantity being estimated. A *minimum variance* estimate has the property that its error variance is less than or equal to that of any other unbiased estimate. A *consistent* estimate is one which converges to the true value as the number of measurement increase. By these definitions provided by Gelb [23], we are looking for an *unbiased, minimum variance, consistent* filter.

When a controller requires state feedback, but the available measurements do not include all necessary states, there must be a method of estimating the missing states that contains minimal error. This requires the following [24]:

- The ability to define a state-estimate error metric to be minimized in estimation
- A knowledge of measurement error statistics, dynamic system models, and system input statistics
- Algorithms for using this information to compute minimum-error state estimates

The Kalman Filter is one such suitable algorithm for state estimation.

3.4 Advanced Optimal Linear Filtering: The Kalman Filter

In 1960, R. E. Kalman published his paper entitled, "A New Approach to Linear Filtering and Prediction Problems," describing the use of a recursive filter to solve the Weiner problem for gauss-markov sequences through the use of state-space representation from the viewpoint of conditional distributions and expectations [25]. The Kalman filter is powerful because it not only supports estimation of the past, present, and future, but can do so even if the modeled system is not known precisely. The following concise derivation is from Welch and Bishop [26].

A discrete time process, with a state vector $x \in \mathfrak{R}^n$ is governed by the following linear stochastic difference equation

$$x_k = A_{k-1}x_{k-1} + Bu_{k-1} + w_{k-1} \quad (3-40)$$

with a measurement output vector $z \in \mathfrak{R}^m$

$$z_k = Cx_k + v_k \quad (3-41)$$

where w_k and v_k are process noise and measurement noise, respectively. These noise terms are assumed to be white noise, having a Gaussian distribution with a mean of zero and a covariance of Q and R , where Q is the process noise covariance and R is the measurement noise covariance.

$$\begin{aligned} p(w) &\sim N(0, Q) \\ p(v) &\sim N(0, R) \end{aligned} \quad (3-42)$$

The A, B, and C matrices from equations (3-40) and (3-41) are standard discrete-time state space matrices, with the following dimensions: $A \in \mathfrak{R}^{n \times n}$, $B \in \mathfrak{R}^{n \times r}$, $C \in \mathfrak{R}^{m \times n}$. The input vector has the dimension $u \in \mathfrak{R}^r$.

Given that

$$\begin{aligned}\hat{x}_k^- &\equiv \text{a priori state estimate at time step } k, \text{ given knowledge of the} \\ &\quad \text{process prior to step } k \\ \hat{x}_k &\equiv \text{a posteriori state estimate at step } k \text{ given measurement } z_k\end{aligned}$$

where the a priori, e_k^- , and a posteriori, e_k , state estimate errors are

$$\begin{aligned}e_k^- &= x_k - \hat{x}_k^- \\ e_k &= x_k - \hat{x}_k\end{aligned}\tag{ 3-43 }$$

Therefore the a priori estimate error covariance, P_k^- , and the a posteriori estimate error covariance, P_k , are

$$P_k^- = E[e_k^- e_k^{-T}] \quad P_k = E[e_k e_k^T]\tag{ 3-44 }$$

Also, the Kalman filter works in such a way that it sets the estimated state's value at the expected value of the actual state.

$$\hat{x}_k = E[x_k]\tag{ 3-45 }$$

Therefore, it is important to point out that the Kalman filter maintains the first two moments of the state distribution found in equation (3-44) and equation (3-45) above. Because of this, the a posteriori state estimate, \hat{x}_k , reflects the mean of the state distribution and the a posteriori estimate error covariance reflects the variance of the state distribution

[23]. In other words, the conditional probability density function of x_k , conditioned on a value of z_k , is defined as

$$\begin{aligned} p(x_k | z_k) &\sim N(E[x_k], E[(x_k - \hat{x}_k)(x_k - \hat{x}_k)^T]) \\ &= N(\hat{x}_k, P_k) \end{aligned} \quad (3-46)$$

To derive the Kalman filter equations we begin with the goal of finding an equation that computes \hat{x}_k as a linear combination of \hat{x}_k^- and a weighted difference between the actual measurement, z_k , and a measurement prediction $C\hat{x}_k^-$.

$$\hat{x}_k = \hat{x}_k^- + K_k (z_k - C\hat{x}_k^-) \quad (3-47)$$

where the term multiplied by the gain, K_k , is the measurement residual. If the measurement residual is equal to zero (the difference between estimated output and actual output is zero) then the a priori state estimate does not need to be altered before it becomes the state estimate at time step k . The $n \times m$ matrix K_k , called the Kalman Gain, is used to minimize the a posteriori error covariance, P_k , found in equation (3-44).

Given equation (3-43) and by using equation (3-47) you get

$$e_k = x_k - \hat{x}_k - K_k (z_k - C_k \hat{x}_k^-) \quad (3-48)$$

Substituting equation (3-48) into equation (3-44) you get

$$P_k = E[(x_k - \hat{x}_k - K_k (z_k - C_k \hat{x}_k^-))(x_k - \hat{x}_k - K_k (z_k - C_k \hat{x}_k^-))^T] \quad (3-49)$$

After performing the indicated expectation, then taking the derivative of the sum of the diagonal terms of the result with respect to k , and setting that result equal to zero, the equation can be solved for the Kalman Gain.

$$K_k = P_k^- C_k^T (C_k P_k^- C_k^T + R)^{-1} \quad (3-50)$$

A more rigorous derivation of the Kalman gain is provided by Gelb [23] and by Mangoubi [22] and follows below. Gelb begins with the following assumed form of a linear, recursive estimator

$$\hat{x}_k = K_k' x_k^- + K_k z_k \quad (3-51)$$

where K_k and K_k' are time-varying weighting matrices to be defined later.

Given that

$$\begin{aligned} \hat{x}_k^- &= x_k + e_k^- \\ \hat{x}_k &= \hat{x}_k^- + e_k \end{aligned} \quad (3-52)$$

by substituting equations (3-41) and (3-52) into equation (3-51) results in the following definition for a posteriori error at time step k .

$$e_k = [K_k' + K_k C_k - I] x_k + K_k' e_k^- + K_k v_k \quad (3-53)$$

Since v_k is defined as white noise with a mean of zero, the expectation of $v_k = 0$. Then, if the expectation of the a priori estimation error equals zero ($E[e_k^-] = 0$) then the estimator is unbiased (i.e. $E[e_k] = 0$) for any state vector if the bracketed terms in equation (3-53) are equal to zero. Therefore

$$[K_k' + K_k C_k - I] = 0 \quad (3-54)$$

and K_k' must be defined as

$$K_k' = I - K_k C_k \quad (3-55)$$

Rearranging the terms in equation (3-52) and substituting them into equation (3-53) results in

$$\begin{aligned} \hat{x}_k - x_k &= [I - K_k C_k + K_k C_k + I]x_k + [I - K_k C_k](\hat{x}_k^- - x_k) + K_k v_k \\ \hat{x}_k &= [I - K_k C_k](\hat{x}_k^- - x_k) + K_k v_k + x_k \\ &= [I - K_k C_k]\hat{x}_k^- - [I - K_k C_k]x_k + K_k v_k + x_k \\ &= [I - K_k C_k]\hat{x}_k^- - x_k + K_k C_k x_k + K_k v_k + x_k \\ &= [I - K_k C_k]\hat{x}_k^- + K_k [C_k x_k + v_k] \end{aligned} \quad (3-56)$$

By substituting equation (3-41) into equation (3-56) the state update is obtained.

$$\begin{aligned} \hat{x}_k &= [I - K_k C_k]\hat{x}_k^- + K_k z_k \\ \text{or} \\ \hat{x}_k &= \hat{x}_k^- + K_k [z_k - C_k \hat{x}_k^-] \end{aligned} \quad (3-57)$$

Using equation (3-41), (3-52), and (3-57) the error dynamics are

$$e_k = [I - K_k C_k]e_k^- + K_k v_k \quad (3-58)$$

This equation for e_k is used in order to update the error covariance P_k defined in equation (3-44).

$$P_k = E[((I - K_k C_k)e_k^- + K_k v_k)((I - K_k C_k)e_k^- + K_k v_k)^T] \quad (3-59)$$

Expansion of this equation leads to

$$P_k = E[(I - K_k C_k)e_k^- e_k^{-T} (I - K_k C_k)^T + (I - K_k C_k)e_k^- v_k^T K_k^T + K_k v_k e_k^{-T} (I - K_k C_k)^T + K_k v_k v_k^T K_k^T] \quad (3-60)$$

By definition

$$E[e_k^- e_k^{-T}] = P_k^- \quad (3-61)$$

and

$$E[v_k v_k^T] = R_k \quad (3-62)$$

Since measurement errors are uncorrelated

$$E[e_k^- v_k^T] = E[v_k e_k^{-T}] = 0 \quad (3-63)$$

By substituting equations (3-61), (3-62), and (3-63) into equation (3-60) the error covariance update is

$$P_k = (I - K_k C_k)P_k^- (I - K_k C_k)^T + K_k R_k K_k^T \quad (3-64)$$

The selection of K_k is used to minimize the weighted sum of the diagonal elements of this error covariance matrix. Therefore, the cost function is

$$J_k = E[e_k^T S e_k] \quad (3-65)$$

where S is any positive semidefinite matrix (i.e. I). Hence the cost function is just the trace of the error covariance matrix, which would be the same as minimizing the length of the estimation error vector.

$$J_k = \text{trace}[P_k] \quad (3-66)$$

To determine the value of K_k that provides a minimum, it is necessary to create the Jacobian of the cost function with respect to the gain and set it equal to zero. Since it is known that [23]

$$\frac{\partial}{\partial A} [\text{trace}(ABA^T)] = 2AB \quad (3-67)$$

then

$$0 = -2(I - K_k C_k) P_k^- C_k^T + 2K_k R_k \quad (3-68)$$

Solving for K_k results in

$$K_k = P_k^- C_k^T [C_k P_k^- C_k^T + R_k]^{-1} \quad (3-69)$$

Gelb notes that the value of K_k calculated by using this equation is optimal and can be proven so through the examination of the Hessian of the cost function (i.e. Hessian of J_k is positive semidefinite).

$$\left| \frac{\partial^2 J_k}{\partial \hat{x}^2} \right| \geq 0 \quad (3-70)$$

Using equation (3-69) and equation (3-64), the optimized value of the estimation error covariance matrix is calculated as

$$\begin{aligned} P_k &= P_k^- - P_k^- C_k^T [C_k P_k^- C_k^T + R_k]^{-1} C_k P_k^- \\ &= [I - K_k C_k] P_k^- \end{aligned}$$

(3-71)

The state estimation and error covariance are extrapolated from one time step to another by

$$\begin{aligned} \hat{X}_k^- &= A_{k-1} \hat{X}_{k-1} \\ P_k^- &= A_{k-1} P_{k-1} A_{k-1}^T + Q_{k-1} \end{aligned}$$

(3-72)

It is helpful to see the discrete time Kalman filter variables in a graphical timing diagram.

This helps to visually understand the steps needed in Kalman filtering.

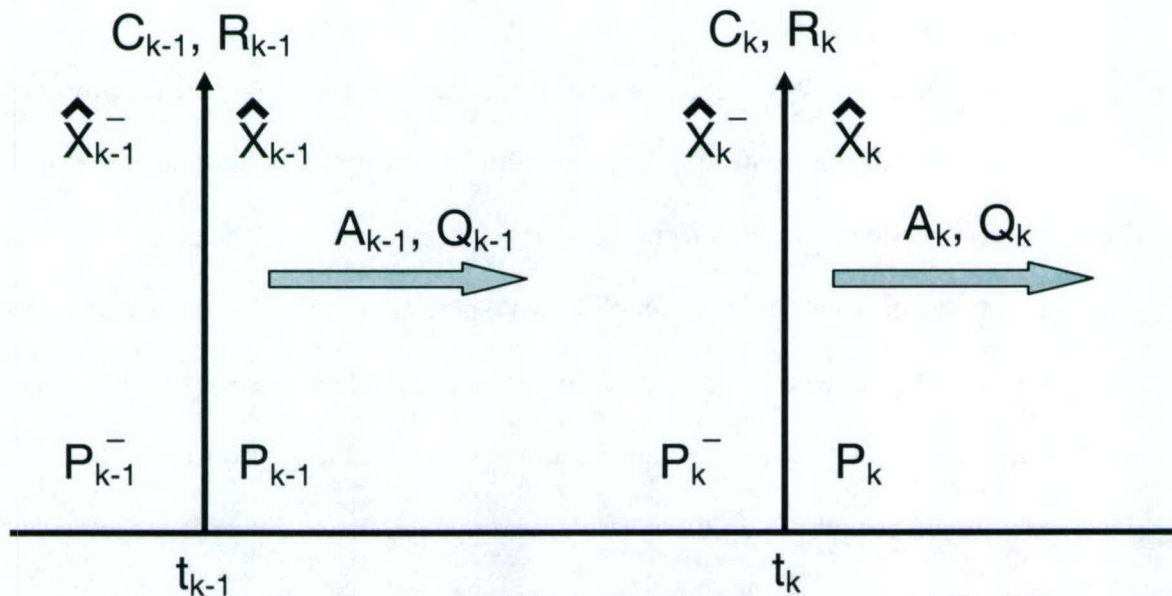


Figure 3-11. Discrete Kalman Filter Timing Diagram [23]

A summary of the discrete time Kalman Filter Equations can be found below.

Kalman Filter Equations		
	System Model	$x_k = A_{k-1}x_{k-1} + w_{k-1}, \quad w_{k-1} \sim N(0, Q_k)$
	Measurement Model	$z_k = C_k x_k + v_k, \quad v_k \sim N(0, R_k)$
	Initial Conditions	$E[x(0)] = \hat{x}_0, \quad E[(x(0) - \hat{x}_0)(x(0) - \hat{x}_0)^T] = P_0$
	Other Assumptions	$E[w_k v_j^T] = 0 \text{ for all } j, k$
Time Update	State Estimation Extrapolation	$\hat{x}_k^- = A_{k-1} \hat{x}_{k-1} + w_{k-1}$
	Error Covariance Extrapolation	$P_k^- = A_{k-1} P_{k-1} A_{k-1}^T + Q_{k-1}$
Measurement Update	Kalman Gain Matrix	$K_k = P_k^- C_k^T [C_k P_k^- C_k^T + R_k]^{-1}$
	State Estimate Update	$\hat{x}_k = \hat{x}_k^- + K_k [z_k - C_k \hat{x}_k^-]$
	Error Covariance Update	$P_k = [I - K_k C_k] P_k^-$

Table 3-4. Summary of Discrete Kalman Filter Equations [23]

As Welsh and Bishop [26] describe it, the Kalman filter estimates a process by using a form of feedback control; the filter estimates the process state at some time and then obtains feedback in the form of noisy measurements. Therefore, the Kalman filter equations can be divided into a two stage algorithm, a time update group and a measurement update group. The time update portion involves the forward projection of the current state and error covariance estimates to gain the a priori estimates needed for the measurement update. In the measurement update, the so called feedback occurs allowing for changes based on the new measurements. This new knowledge improves upon the a priori estimates and forms the improved a posteriori estimates.

Welsh and Bishop [26] liken this algorithm to a predictor (time update) corrector (measurement update) algorithm. Gelb has also named the two stages of the Kalman filter algorithm in a similar fashion as the extrapolation stage (time update) and the update stage (measurement update). The time update equation can be found in rows 5 and 6 of Table 3-4 and the measurement update equations can be found in rows 7, 8, and 9 of Table 3-4.

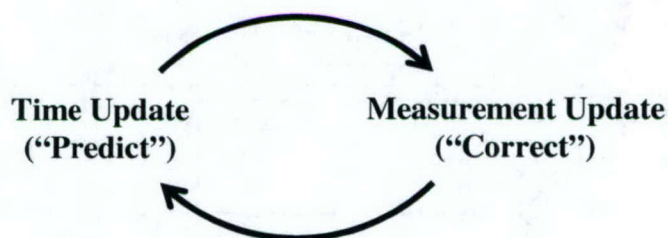


Figure 3-12. Predictor - Corrector Model [26]

Notice that the time update equations project the state and error covariance estimates forward from time step $k-1$ to k , while the measurement update equations all work at time step k . In the measurement update the first step is to calculate a new Kalman gain K_k . The next step is to take a measurement of the process to get z_k . Then with this measurement, an a posteriori state estimate, \hat{x}_k , can be calculated. Then the final step of the Kalman filter algorithm iteration is to calculate the a posteriori error covariance matrix. The next iteration starts by using the last iteration's a posteriori estimates as the new iteration's a priori estimate. The recursive nature of the Kalman filter algorithm provides a large computational improvement on the Wiener filter, which is designed to operate on all of the data directly for each estimate [26].

A block diagram of the plant and estimator can be found in Figure 3-13, which shows the State Estimate Extrapolation and the State Estimate Update as listed in Table 3-4.

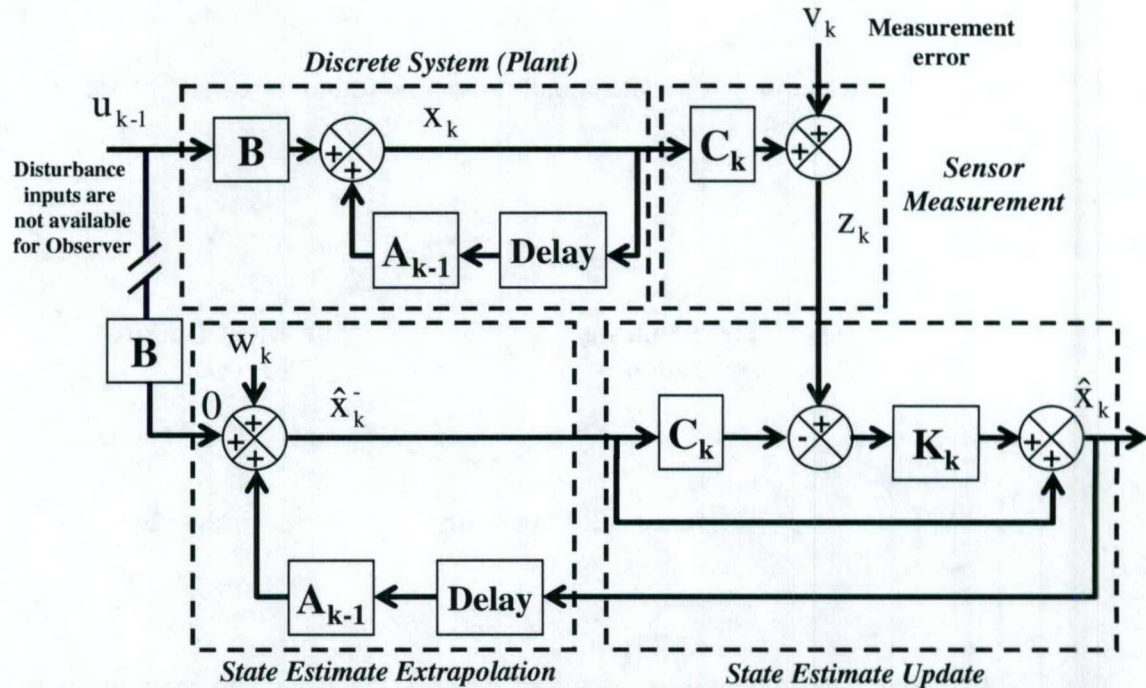


Figure 3-13. Block Diagram of Discrete System and State Estimator

The Kalman gain, K_k , in Figure 3-13 is calculated using the equations from Table 3-4 and is shown in Figure 3-14. It is important to note that in the example used in this thesis, the deterministic input into the estimator is a zero vector since no disturbance measurements are available for state estimation. Figure 3-14 shows the Error Covariance Extrapolation, Error Covariance Update, and the Kalman Gain Computation as shown in Table 3-4.

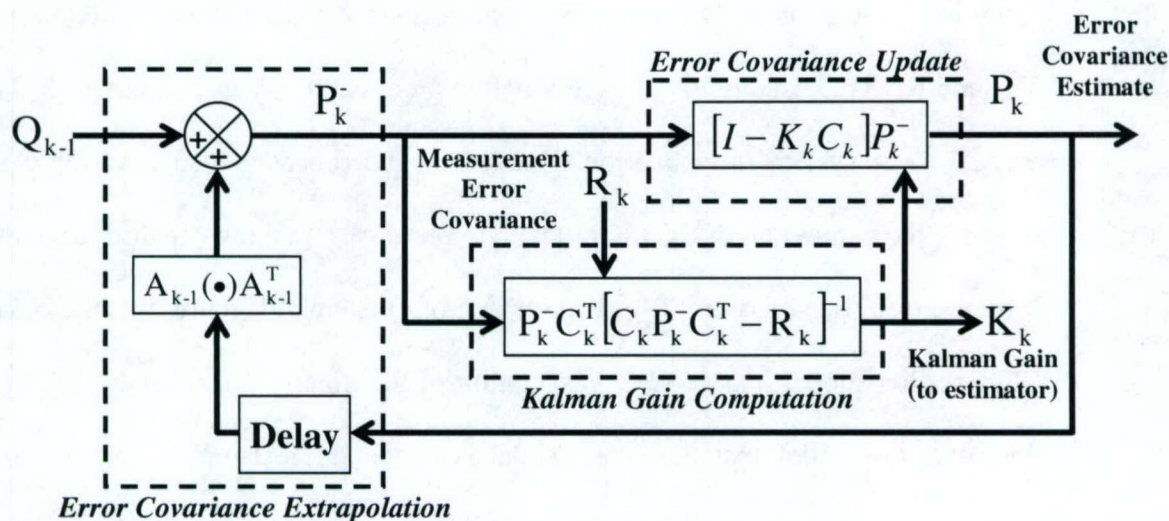


Figure 3-14. Block Diagram Kalman Gain Computation

The measurement noise covariance, R_k , is usually known since some measurements are taken. This allows for the calculation of R_k prior to the operation of the filter or at the beginning of the operation in some off-line process. On the other hand, the measurement of the process noise covariance is more difficult to calculate. This is reasonable due to the fact that there is no way to observe the process that is being estimating; if there was, there would be no need for estimation in the first place. However, acceptable results can result if one "injects" enough uncertainty into the process via the selection of Q [26]. This statement may seem vague, but it is important to understand that the process noise covariance is specific to each application. Therefore, performance will change for different values of Q . Common engineering techniques were used to find an initial value for Q (see Section 3.5), which remained constant throughout the testing process in order to standardize the results.

Albeit the limitations for Q , superior filter performance can still be achieved through tuning of Q and R . This usually involves an off-line process, involving a separate Kalman Filter, referred to as system identification. Increasing the process noise covariance effectively increases the bandwidth of the filter, which improves its tracking capabilities at the expense of more noise transmission [27]. If the value of Q is small it represents the belief that the Kalman filter model is a good representation of the plant. If the value of Q is large that represents our belief that the filter model is a poor representation and that trust in the measurement must be increased. In the special case where both Q and R are constants, both the estimation covariance and the Kalman gains are guaranteed to stabilize quickly and remain constant.

3.5 Initial Kalman Filter Parameter Calculations

Standard engineering methods were used in the determination of unknown initial measurement noise covariance, R , process noise covariance, Q , and error covariance, P . The initial Q matrix was set equal to a diagonal matrix representing a standard deviation of 5% of the steady state amplitude, A_{ss} , for the corresponding state.

$$Q = \text{diag}(A_{ss} * 0.05)^2 \quad (3-73)$$

The steady state amplitudes can be calculated prior to filter operation through time domain simulations of the filter model.

The initial R matrix was set equal a diagonal matrix representing a standard deviation of 2% of the steady state amplitude for the corresponding plant state.

$$R = \text{diag}(A_{ss} * 0.02)^2 \quad (3-74)$$

The initial P matrix was set to equal a diagonal matrix, whose elements represent the square of three times the steady state amplitude for each state.

$$P = \text{diag}(A_{ss} * 3)^2 \quad (3-75)$$

Since there is no knowledge of the plant's initial conditions, the initial conditions for the observer model were set to zero, even though the actual initial conditions applied to the plant were not. The initial conditions were set to equal the product of the steady state amplitude and a random number, rand, defined by a Gaussian distribution with a mean of zero and a standard deviation of 1. Using this distribution allowed for the initial conditions to be 180° out of phase.

$$x_{0_env} = A_{ss} * \text{rand} \quad (3-76)$$

4 Results

Three different sets of tests were performed: 1) The first set of tests were conducted to verify the performance of disturbance modeling within the filter model, ISS Model 1, 2) The second set of tests show the increased range of disturbance frequencies under which the Kalman filter is able to operate by using an expanded ISS disturbance model, ISS Model 2 and 3) The third set of tests included Monte Carlo analysis to determine robustness and investigate factors which have the most influence on the estimation error. These factors include differences between the plant and filter models (parameter variation), imbalance disturbance amplitude variation, and ISS disturbance frequency variation.

4.1 Performance Measures

Performance will be evaluated by using different metrics to include a measure of percent amplitude error in estimation, the duration of error, estimation error standard deviation, and time to convergence.

4.1.1 Estimation Percent Amplitude Error

Estimation percent amplitude error is defined as the ratio of the 2-norm of the error over the 2-norm of the actual state at steady state multiplied by 100%

$$\% \text{ amplitude error} = \frac{\|x - \hat{x}\|_2}{\|x\|_2} * 100 \% = \frac{\|x_{err}\|_2}{\|x\|_2} * 100 \%$$

(4-1)

where x is the actual state, \hat{x} is defined as the estimated state, and the error, x_{err} , is defined as the difference between the actual state and the estimated state.

4.1.2 Error Duration

Corresponding to the percent amplitude error there is also an “error duration”, which measures the time that is spent within a certain percent amplitude error range with respect to the duration of the simulation. The percent amplitude estimation error, which is calculated at each time step, is collected into bins which divide the total range of percent amplitude estimation error (0 to 100%) equally (e.g., bin 1: 0 to 5%, bin 2: 6 to 10%, bin 3: 11 to 15%, etc). Dividing the number of occurrences in a given bin by the total number of simulation data point collected gives the percent of simulation time that resulted in an error within that bin’s range. See Figure 4-1 for an example of the error duration plot.

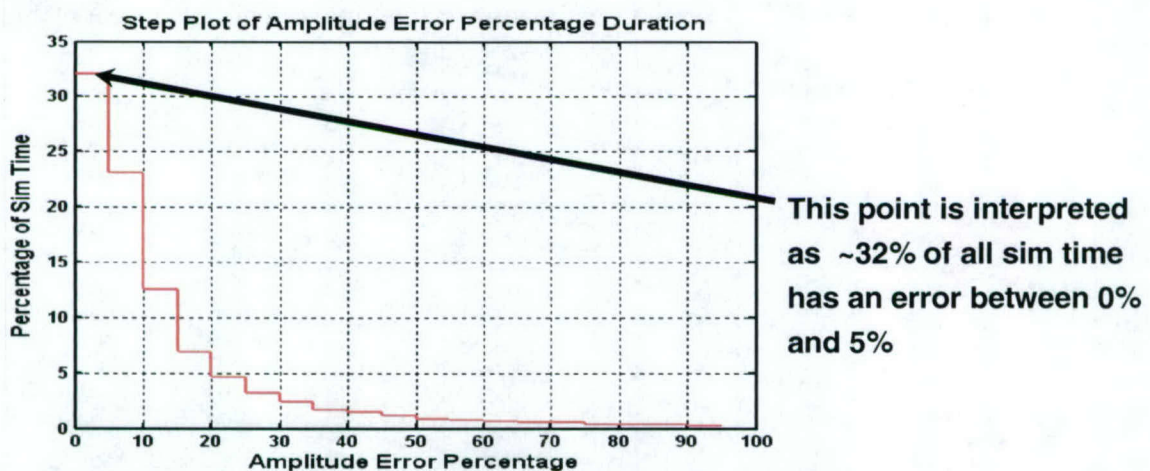


Figure 4-1. Example of Error Duration Performance Metric

While the percent amplitude error measures the error magnitude, the error duration provides insight to the severity of the estimation error. For instance a time history of brief but large error spikes may produce a large percent amplitude error, but looking at the error duration plot will show that the estimation error is relatively benign and may still be acceptable to slower controllers with appropriate robustness.

4.1.3 Estimation Error Standard Deviation Envelope

Yet another useful metric is the estimation error standard deviation envelope created by plotting the \pm square root of the error covariance, P , time history for a given state [27][28][29]. Plotting the amplitude error and the estimation envelope provides an indication of how often the error is outside of one standard deviation of the expected or predicted error values. From this plot, the percent of time the error spends outside of the estimation envelope can be calculated to assess the quality of the estimation. Figure 4-2 is an example plot of estimation error with the superimposed error standard deviation envelope for a case of excellent estimation, while an example of unacceptable estimation can be found in Figure 4-3.

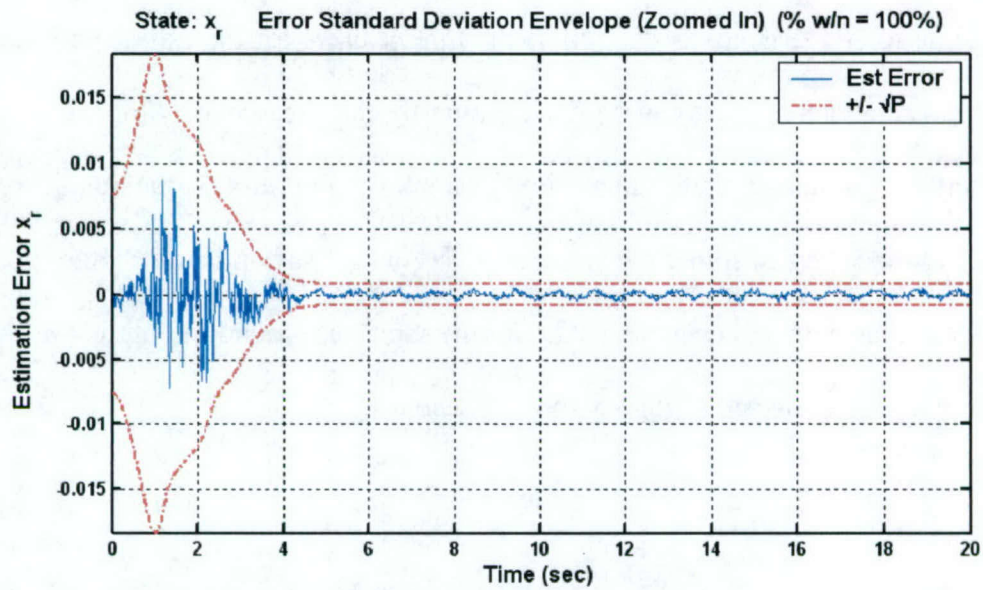


Figure 4-2. Example Plot of Estimation Error and Error Standard Deviation Envelope for Excellent Estimation (100% within bounds)

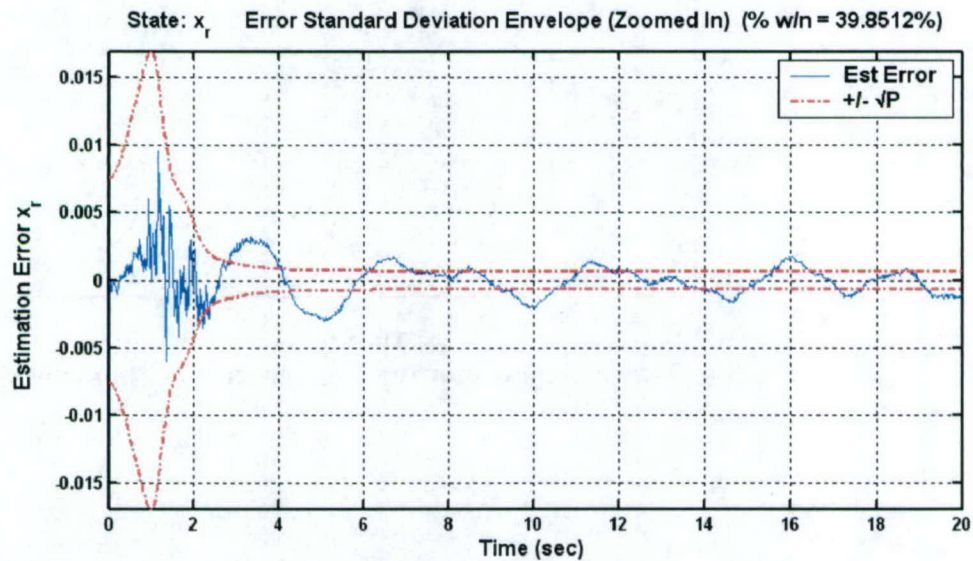


Figure 4-3. Example Plot of Estimation Error and Standard Deviation Envelope for Unacceptable Estimation (~40% within bounds)

4.1.4 Time to Convergence

Time to convergence is defined as the time it takes for the estimated state to converge to the actual state. This can be determined by the time it takes for the error covariance to settle to a steady state value. For example in Figure 4-3, the square root of the error covariance settles sometime between ~3 seconds. As confirmed by the time history plot of the actual state and estimated state for the same case found in Figure 4-4, the state estimate converges to the actual state within 2.5 seconds.

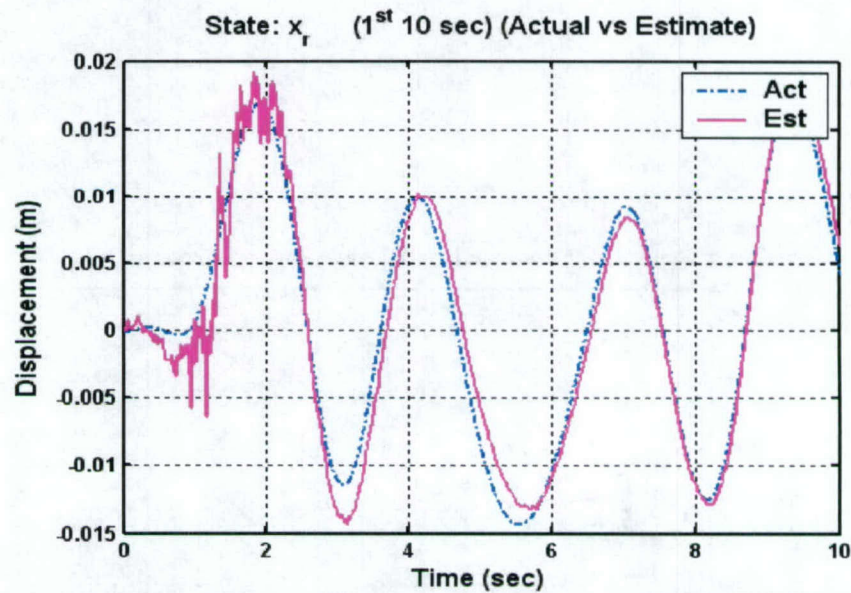


Figure 4-4. Time History Showing Convergence within 2.5 Seconds

4.2 ISS Disturbance Models Used for Testing

The first ISS disturbance model, called “ISS Model 1” is the 4 state ISS disturbance model described by equations (3-6) through (3-9) in Section 3.1.2.2. This model captures one translational ISS disturbance frequency (ω_{dst}) and one rotational disturbance frequency (ω_{dsr}).

The second ISS disturbance model, called “ISS Model 2” is the 8 state ISS disturbance model described by equations (3-10) through (3-13) in Section 3.1.2.3. ISS Model 2 represents the ISS disturbance as sums of two sinusoidal disturbances, with two translational and two rotational disturbance frequencies of ω_{dst1} , ω_{dst2} , and ω_{dsr1} , ω_{dsr2} , respectively.

4.3 ISS Model 1 Test: Performance

The first set of tests attempt to answer two important questions: 1) Will disturbance modeling, of both the rotor disturbance and/or the ISS disturbance, inside the observer model, allow for estimation of absolute rotor states from relative measurement corrupted by sensor noise? 2) How much of an improvement is made over an observer with no disturbance modeling within the observer model?

To answer these two questions, the same disturbances will be applied to: 1) an observer model with rotor and ISS disturbances modeling, 2) an observer model with only rotor

disturbance modeling, 3) an observer model with only ISS disturbance modeling, and 4) an observer model with no disturbance modeling.

4.3.1 ISS Model 1 Test Set-Up

Testing parameters will be chosen using two different ratios: 1) Frequency Ratio (FR) and 2) Amplitude Ratio (AR). FR is the ratio of the ISS disturbance frequency, ω_{ds} , to the rotor disturbance frequency, ω_{dr} , as shown in equation (4-2).

$$FR = \frac{\omega_{ds}}{\omega_{dr}} \quad (4-2)$$

This ratio is used as a guide to identify worst case conditions. A worst case scenario for separating a single relative measurement into its components will occur when those components have similar frequency content. Therefore, after the rotor disturbance frequencies have been chosen, testing will occur such that the ISS disturbance frequency will be 90%, 100%, and 110% of the rotor disturbance frequency.

The rotor disturbance frequencies were chosen to equal the peak mode for each of the following transfer functions from ISS disturbance inputs to relative measurements: 1) ISS disturbance in the x-axis to relative measurement in the x-axis (d_{xs} to x_{rel}), 2) ISS disturbance in the y-axis to relative measurement in the y-axis (d_{ys} to y_{rel}), 3) ISS disturbance about the x-axis to relative measurement about the x-axis ($d_{\phi xs}$ to ϕ_{xrel}), and 4) ISS disturbance about the y-axis to relative measurement about the y-axis ($d_{\phi ys}$ to ϕ_{yrel}). See Figure 4-5 for Bode plots and peak frequencies used to determine testing frequencies.

The “dof of focus” will be determined by using the peak mode in a certain axis. For example, the dof of focus will be in the x-axis when a 0.399 Hz disturbance is used.

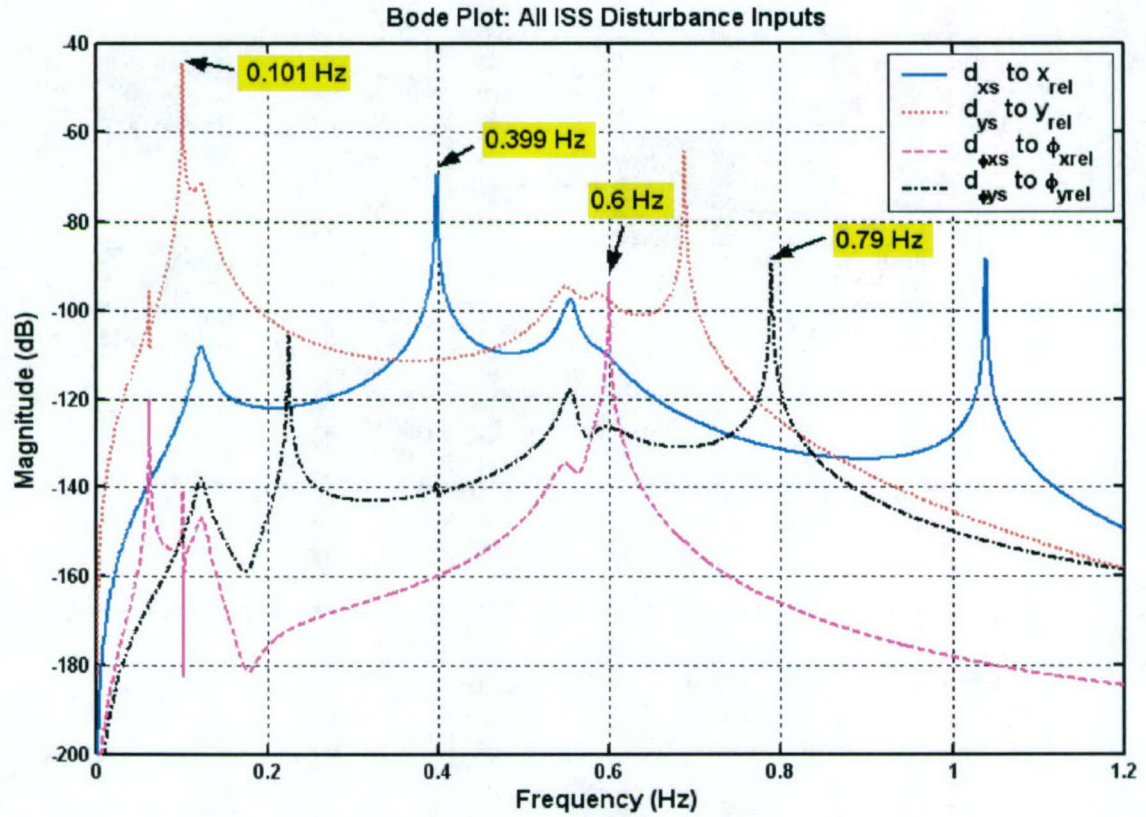


Figure 4-5. Bode Plot Used to Determine Testing Frequencies

AR is the output contribution ratio or the ratio of the relative measurement content due to the rotor disturbance, y_{rel_dr} , and due to ISS disturbance, y_{rel_ds} .

$$AR = \frac{y_{rel_ds}}{y_{rel_dr}} \quad (4-3)$$

Since the system is linear, superposition can be used. First, the relative motion is measured when only the rotor disturbances act on the plant. Then the relative motion is measured when only the ISS disturbances act on the plant. The amplitude of the ISS disturbances, F_s ,

are adjusted until the ratio of the plant output due to only ISS disturbance, is 10% and 100% of the plant output due to only rotor disturbances. See Figure 4-6 below. Note that all other disturbance amplitudes are set to 1. See Table 4-1 for further explanation.

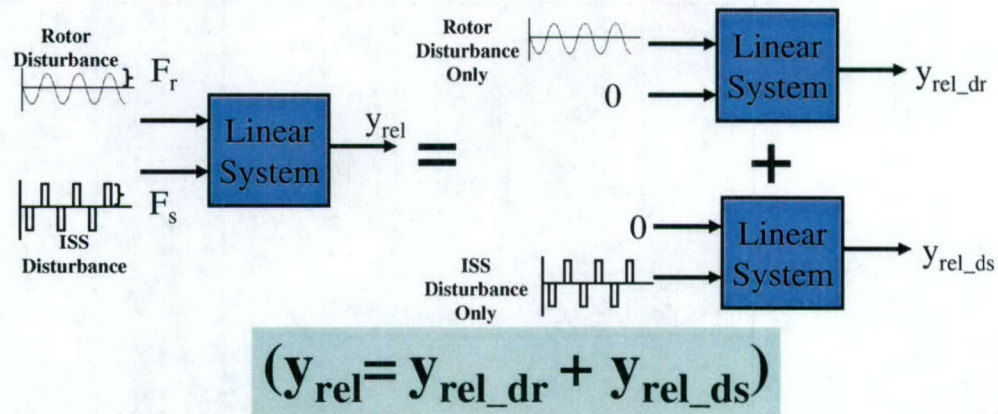


Figure 4-6. Amplitude Ratio Components

Figure 4-7 shows a flow chart describing the method used for determining the ISS disturbance force amplitudes necessary to produce the desired ARs.

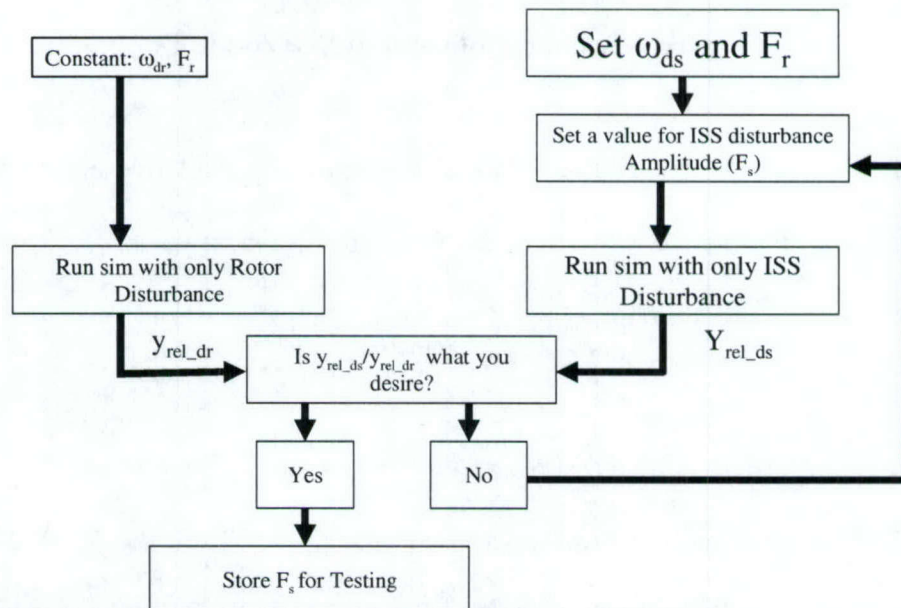


Figure 4-7. Flow Chart to Determine F_s Necessary for Desired Amplitude Ratios

With the rotor disturbance frequencies determined from Figure 4-5, the F_s values were determined to get the desired AR. Table 4-1 contains the parameters used for testing ISS Model 1.

Dof of Focus	Disturbance Frequencies			AR	ISS Force/Torque Amplitudes			
	FR	ω_{ds} (Hz)	ω_{dr} (Hz)		F_{xs} (N)	F_{ys} (N)	$T_{\phi xs}$ (Nm)	$T_{\phi ys}$ (Nm)
x	0.9	0.359	0.399	0.1	819.18	1	1	1
x	0.9	0.359	0.399	1	8192.2	1	1	1
x	1.0	0.399	0.399	0.1	9.9342	1	1	1
x	1.0	0.399	0.399	1	99.316	1	1	1
x	1.1	0.439	0.399	0.1	608.06	1	1	1
x	1.1	0.439	0.399	1	6081.2	1	1	1
y	0.9	0.091	0.101	0.1	1	22.272	1	1
y	0.9	0.091	0.101	1	1	222.73	1	1
y	1.0	0.101	0.101	0.1	1	0.45137	1	1
y	1.0	0.101	0.101	1	1	4.5132	1	1
y	1.1	0.111	0.101	0.1	1	9.1608	1	1
y	1.1	0.111	0.101	1	1	91.66	1	1
ϕ_x	0.9	0.540	0.600	0.1	1	1	118340	1
ϕ_x	0.9	0.540	0.600	1	1	1	1183800	1
ϕ_x	1.0	0.600	0.600	0.1	1	1	950.29	1
ϕ_x	1.0	0.600	0.600	1	1	1	9508	1
ϕ_x	1.1	0.660	0.600	0.1	1	1	152230	1
ϕ_x	1.1	0.660	0.600	1	1	1	1522900	1
ϕ_y	0.9	0.711	0.790	0.1	1	1	1	30856
ϕ_y	0.9	0.711	0.790	1	1	1	1	308650
ϕ_y	1.0	0.790	0.790	0.1	1	1	1	181.8
ϕ_y	1.0	0.790	0.790	1	1	1	1	1818.4
ϕ_y	1.1	0.869	0.790	0.1	1	1	1	39414
ϕ_y	1.1	0.869	0.790	1	1	1	1	394250

Table 4-1. Testing Parameters Determined for Desired FR and AR

4.3.2 ISS Model 1 Test Results

As a summary of the data presented later in this section, Table 4-2 below helps to clearly show the conclusions that can be drawn with the examination of all test cases, which is: All disturbance modeling is necessary in order to perform good estimation. Table 4-2 shows the percent amplitude error in estimation for a case where all disturbances are modeled within the filter and a case where none of the disturbances are modeled, where each percent error value was given for the case where $AR = FR = 1$ for the given dof of focus.

Dof of Focus	Percent Amplitude Error	
	All Disturbance Models	No Disturbance Models
x	2.86%	39.95%
y	0.18%	30.33%
ϕ_x	0.43%	91.47%
ϕ_y	1.45%	59.67%

Table 4-2. Percent Amplitude Error in Estimation between a Filter Model with All Disturbances Modeled and a Filter Model with No Disturbance Modeling

Table 4-2 shows that without all disturbance modeling, estimation within acceptable error bounds is not possible. The rest of this section will go into further detail and give data for the different levels of disturbance modeling fidelities, but the conclusion that all disturbance modeling is necessary is still the same.

A comparison of the results from using all disturbance models versus only rotor disturbance model for each test case can be found in Table 4-3.

Dof of Focus	Disturbance Frequencies			ISS Force/Torque Amplitudes					Percent Amplitude Error							
	FR	ω_{ds} (Hz)	ω_{dr} (Hz)	AR	F_{xs} (N)	F_{ys} (N)	T_{xss} (Nm)	T_{yys} (Nm)	x_r		y_r		ϕ_{xr}		ϕ_{yr}	
									All d Models	No d_{iss}	All d Models	No d_{iss}	All d Models	No d_{iss}	All d Models	No d_{iss}
x	0.9	0.359	0.399	0.1	819.18	1	1	1	5.42	14.24	3.94	4.15	1.02	1.02	1.45	1.45
x	0.9	0.359	0.399	1	8192.2	1	1	1	11.32	32.94	3.26	3.28	1.24	1.24	1.80	1.80
x	1.0	0.399	0.399	0.1	9.9342	1	1	1	3.47	3.47	4.01	4.01	0.98	0.98	1.38	1.38
x	1.0	0.399	0.399	1	99.316	1	1	1	2.86	2.98	4.44	4.44	0.91	0.91	1.42	1.42
x	1.1	0.439	0.399	0.1	608.06	1	1	1	4.14	11.14	4.02	4.21	1.01	1.01	1.37	1.37
x	1.1	0.439	0.399	1	6081.2	1	1	1	7.60	44.43	4.38	4.47	1.25	1.25	1.37	1.37
y	0.9	0.091	0.101	0.1	1	22.272	1	1	1.10	1.11	0.47	3.94	1.10	4.94	1.26	1.26
y	0.9	0.091	0.101	1	1	222.73	1	1	1.17	1.17	2.42	23.52	2.19	5.20	1.42	1.42
y	1.0	0.101	0.101	0.1	1	0.45137	1	1	1.09	1.09	0.20	0.24	0.80	0.81	1.24	1.24
y	1.0	0.101	0.101	1	1	4.5132	1	1	1.10	1.10	0.18	0.63	0.64	0.87	1.24	1.24
y	1.1	0.111	0.101	0.1	1	9.1608	1	1	1.09	1.09	0.32	2.06	0.85	2.00	1.28	1.28
y	1.1	0.111	0.101	1	1	91.66	1	1	1.13	1.13	1.51	13.90	1.22	2.56	1.59	1.59
ϕ_x	0.9	0.540	0.600	0.1	1	1	118340	1	2.46	2.57	0.50	0.65	0.66	3.80	1.40	1.45
ϕ_x	0.9	0.540	0.600	1	1	1	1183800	1	0.31	0.32	0.11	0.13	0.15	0.78	0.88	0.94
ϕ_x	1.0	0.600	0.600	0.1	1	1	950.29	1	6.27	6.37	3.90	3.99	1.09	1.25	1.25	1.25
ϕ_x	1.0	0.600	0.600	1	1	1	9508	1	1.80	1.80	0.34	0.35	0.43	0.56	0.93	0.93
ϕ_x	1.1	0.660	0.600	0.1	1	1	152230	1	2.03	2.03	0.40	0.40	0.53	2.82	1.55	1.60
ϕ_x	1.1	0.660	0.600	1	1	1	1522900	1	0.29	0.30	0.09	0.09	0.13	0.60	0.95	1.00
ϕ_y	0.9	0.711	0.790	0.1	1	1	1	30856	3.15	7.28	3.83	6.80	1.28	1.43	1.50	6.98
ϕ_y	0.9	0.711	0.790	1	1	1	1	308650	4.82	9.48	4.14	6.37	1.46	1.76	1.39	14.95
ϕ_y	1.0	0.790	0.790	0.1	1	1	1	181.8	2.86	2.87	3.87	3.88	1.20	1.20	1.39	1.47
ϕ_y	1.0	0.790	0.790	1	1	1	1	1818.4	2.96	2.97	3.80	3.80	1.07	1.07	1.45	1.54
ϕ_y	1.1	0.869	0.790	0.1	1	1	1	39414	3.20	3.64	3.76	3.80	1.31	1.44	1.51	5.85
ϕ_y	1.1	0.869	0.790	1	1	1	1	394250	4.12	4.53	4.00	4.08	1.60	1.78	1.44	10.72

Table 4-3. Comparison between Using All Disturbance Models and Only Rotor Disturbance Model: Test Results

The percent amplitude error resulting from the use of all disturbance models is always less than or equal to the percent amplitude error resulting from using a disturbance model that does not include ISS disturbance. This is true for every rotor state and every test case. Test cases where the percent amplitude error is the same, or similar, for both disturbance modeling fidelities occurs only when the AR is small (i.e. rows where AR = 0.1) or if the frequency of the disturbances is not a peak mode frequency in that dof (i.e. all non highlighted results). This is reasonable since these two cases (small AR and non-peak

mode excitation) would cause a small response, therefore it would be expected that ISS disturbance modeling is not necessary for those cases.

A comparison of the results from using all disturbance models versus only ISS disturbance model for each test case can be found in Table 4-4.

Dof of Focus	Disturbance Frequencies			AR	ISS Force/Torque Amplitudes				Percent Amplitude Error							
	FR				F_{xx} (N)	F_{yy} (N)	$T_{\theta_{xx}}$ (Nm)	$T_{\theta_{yy}}$ (Nm)	x_r		y_r		ϕ_x		ϕ_y	
		ω_{dx} (Hz)	ω_{dy} (Hz)						All d Models	No d,	All d Models	No d,	All d Models	No d,	All d Models	No d,
x	0.9	0.359	0.399	0.1	819.18	1	1	1	5.42	60.38	3.94	113.95	1.02	23.32	1.45	31.34
x	0.9	0.359	0.399	1	8192.2	1	1	1	11.32	49.57	3.26	79.24	1.24	19.28	1.80	24.97
x	1.0	0.399	0.399	0.1	9.9342	1	1	1	3.47	119.09	4.01	93.95	0.98	23.96	1.38	31.30
x	1.0	0.399	0.399	1	99.316	1	1	1	2.86	55.19	4.44	128.49	0.91	20.70	1.42	32.25
x	1.1	0.439	0.399	0.1	608.06	1	1	1	4.14	61.94	4.02	117.45	1.01	23.28	1.37	30.97
x	1.1	0.439	0.399	1	6081.2	1	1	1	7.60	70.35	4.38	125.85	1.25	23.70	1.37	27.53
y	0.9	0.091	0.101	0.1	1	22.272	1	1	1.10	11.49	0.47	117.97	1.10	1164.70	1.26	97.72
y	0.9	0.091	0.101	1	1	222.73	1	1	1.17	6.13	2.42	238.83	2.19	499.13	1.42	41.11
y	1.0	0.101	0.101	0.1	1	0.45137	1	1	1.09	15.26	0.20	57.16	0.80	1209.10	1.24	127.06
y	1.0	0.101	0.101	1	1	4.5132	1	1	1.10	13.31	0.18	30.33	0.64	831.74	1.24	119.59
y	1.1	0.111	0.101	0.1	1	9.1608	1	1	1.09	12.63	0.32	97.20	0.85	1234.60	1.28	98.37
y	1.1	0.111	0.101	1	1	91.66	1	1	1.13	9.94	1.51	256.85	1.22	571.91	1.59	62.17
ϕ_x	0.9	0.540	0.600	0.1	1	1	118340	1	2.46	42.09	0.50	7.16	0.66	108.09	1.40	27.25
ϕ_x	0.9	0.540	0.600	1	1	1	1183800	1	0.31	3.98	0.11	1.29	0.15	20.89	0.88	18.03
ϕ_x	1.0	0.600	0.600	0.1	1	1	950.29	1	6.27	109.91	3.90	52.42	1.09	133.67	1.25	22.95
ϕ_x	1.0	0.600	0.600	1	1	1	9508	1	1.80	30.96	0.34	4.16	0.43	92.67	0.93	17.99
ϕ_x	1.1	0.660	0.600	0.1	1	1	152230	1	2.03	33.45	0.40	5.62	0.53	98.85	1.55	29.88
ϕ_x	1.1	0.660	0.600	1	1	1	1522900	1	0.29	3.12	0.09	1.04	0.13	17.38	0.95	15.93
ϕ_y	0.9	0.711	0.790	0.1	1	1	1	30856	3.15	83.30	3.83	79.40	1.28	26.99	1.50	124.09
ϕ_y	0.9	0.711	0.790	1	1	1	1	308650	4.82	93.78	4.14	55.64	1.46	23.48	1.39	152.23
ϕ_y	1.0	0.790	0.790	0.1	1	1	1	181.8	2.86	75.62	3.87	83.80	1.20	25.91	1.39	29.75
ϕ_y	1.0	0.790	0.790	1	1	1	1	1818.4	2.96	45.89	3.80	82.75	1.07	20.85	1.45	61.52
ϕ_y	1.1	0.869	0.790	0.1	1	1	1	39414	3.20	45.08	3.76	80.46	1.31	24.03	1.51	79.70
ϕ_y	1.1	0.869	0.790	1	1	1	1	394250	4.12	72.97	4.00	51.58	1.60	24.83	1.44	146.92

Table 4-4. Comparison between Using All Disturbance Models and Only ISS Disturbance Model: Test Results

The percent amplitude error resulting from the use of all disturbance models is always less than or equal to the percent amplitude error resulting from using a disturbance model that does not include rotor disturbance. This is true for every rotor state and every test case. By

comparing Table 4-3 to Table 4-4, it is evident that the rotor disturbance modeling is most important in reducing the percent amplitude error.

A comparison of the results from using all disturbance models versus no disturbance models for each test case can be found in Table 4-5.

Dof of Focus	Disturbance Frequencies				ISS Force/Torque Amplitudes				Percent Amplitude Error							
	FR	α_{1s} (Hz)	α_{2s} (Hz)	AR	F_{xs} (N)	F_{ys} (N)	$T_{\phi ss}$ (Nm)	$T_{\psi ss}$ (Nm)	x_r		y_r		ϕ_{xr}		ϕ_{yr}	
									All d Models	No d Models	All d Models	No d Models	All d Models	No d Models	All d Models	No d Models
x	0.9	0.359	0.399	0.1	819.18	1	1	1	5.42	60.88	3.94	113.96	1.02	23.32	1.45	31.35
x	0.9	0.359	0.399	1	8192.2	1	1	1	11.32	56.74	3.26	79.24	1.24	19.28	1.80	24.97
x	1.0	0.399	0.399	0.1	9.9342	1	1	1	3.47	58.07	4.01	117.71	0.98	22.93	1.38	31.44
x	1.0	0.399	0.399	1	99.316	1	1	1	2.86	39.95	4.44	130.59	0.91	20.65	1.42	32.13
x	1.1	0.439	0.399	0.1	608.06	1	1	1	4.14	62.08	4.02	117.44	1.01	23.28	1.37	30.97
x	1.1	0.439	0.399	1	6081.2	1	1	1	7.60	79.74	4.38	125.85	1.25	23.70	1.37	27.53
y	0.9	0.091	0.101	0.1	1	22.272	1	1	1.10	11.55	0.47	117.97	1.10	1170.30	1.26	127.01
y	0.9	0.091	0.101	1	1	222.73	1	1	1.17	6.24	2.42	238.83	2.19	497.87	1.42	376.26
y	1.0	0.101	0.101	0.1	1	0.45137	1	1	1.09	12.74	0.20	57.16	0.80	1236.90	1.24	99.28
y	1.0	0.101	0.101	1	1	4.5132	1	1	1.10	12.42	0.18	30.33	0.64	850.12	1.24	91.66
y	1.1	0.111	0.101	0.1	1	9.1608	1	1	1.09	12.60	0.32	97.20	0.85	1239.10	1.28	101.46
y	1.1	0.111	0.101	1	1	91.66	1	1	1.13	9.81	1.51	256.85	1.22	577.49	1.59	414.95
ϕ_x	0.9	0.540	0.600	0.1	1	1	118340	1	2.46	42.17	0.50	6.88	0.66	106.97	1.40	26.18
ϕ_x	0.9	0.540	0.600	1	1	1	1183800	1	0.31	3.98	0.11	1.28	0.15	20.74	0.88	17.88
ϕ_x	1.0	0.600	0.600	0.1	1	1	950.29	1	6.27	111.26	3.90	57.58	1.09	132.93	1.25	21.86
ϕ_x	1.0	0.600	0.600	1	1	1	9508	1	1.80	31.18	0.34	4.90	0.43	91.47	0.93	17.87
ϕ_x	1.1	0.660	0.600	0.1	1	1	152230	1	2.03	33.48	0.40	5.46	0.53	96.71	1.55	28.72
ϕ_x	1.1	0.660	0.600	1	1	1	1522900	1	0.29	3.12	0.09	1.04	0.13	17.20	0.95	15.76
ϕ_y	0.9	0.711	0.790	0.1	1	1	1	30856	3.15	43.01	3.83	82.92	1.28	25.32	1.50	51.10
ϕ_y	0.9	0.711	0.790	1	1	1	1	308650	4.82	86.70	4.14	56.65	1.46	22.58	1.39	136.43
ϕ_y	1.0	0.790	0.790	0.1	1	1	1	181.8	2.86	76.93	3.87	83.73	1.20	26.23	1.39	28.12
ϕ_y	1.0	0.790	0.790	1	1	1	1	1818.4	2.96	46.15	3.80	82.87	1.07	21.04	1.45	59.67
ϕ_y	1.1	0.869	0.790	0.1	1	1	1	39414	3.20	42.50	3.76	81.66	1.31	25.14	1.51	56.61
ϕ_y	1.1	0.869	0.790	1	1	1	1	394250	4.12	71.13	4.00	51.89	1.60	24.50	1.44	140.08

Table 4-5. Comparison between Using All Disturbance Models and Only ISS Disturbance Model: Test Results

The percent amplitude error resulting from the use of all disturbance models is always less than or equal to the percent amplitude error resulting from using no disturbance modeling. This is true for every rotor state and every test case. This is expected because without

disturbance modeling, the filter model has no knowledge of the disturbances that act on the plant.

The time history plots of one case (x_r with $AR = 1$ and $FR = 0.9$) are used to highlight the need for full disturbance modeling within the filter model. The results for all different disturbance modeling fidelity levels can be found in Table 4-6.

Percent Amplitude Error (x_r)			
All Disturbances Models	Only Rotor Disturbance Model	Only ISS Disturbance Model	No Disturbance Models
11.32%	32.94%	49.57%	56.74%

Table 4-6. Performance Verification Test Case for x_r ($AR = 1$, $FR = 0.9$)

It can be concluded from the results shown in Table 4-6 that both the rotor disturbance and ISS disturbance models are necessary for improving estimation capabilities. The rotor disturbance seems to have the highest effect on improving estimation capabilities. A possible explanation of this may be the facts that: 1) the rotor disturbance in the filter model is collocated with the relative measurement sensor, 2) due to the 'nature' or the plant being used, the relative measurement is mostly comprised of the rotor motion. In explanation of fact 2, the plant is stiff everywhere except between the shroud and the rotor (see Figure 2-2). Consequently, regardless of whether the disturbance is acting on the rotor or the outside mass of ISS flex model, the majority of the relative motion will come from the motion of the rotor. The frequency content of the sensor measurement, x_{rel} , shows that the rotor motion, which is at a frequency of 0.399 Hz, is more important than the shroud motion, which is at a frequency of 0.356 Hz.

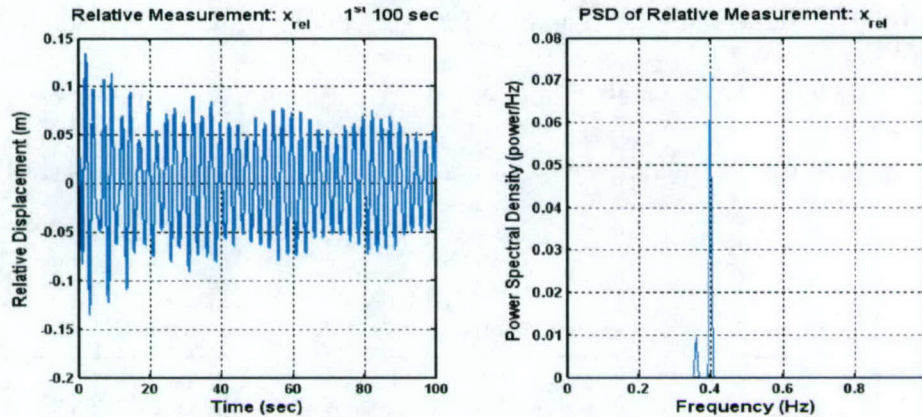


Figure 4-8. Sensor Measurement x_{rel} Time History (left) and PSD (right)

From this reasoning, one would expect that marginal estimation could be achieved when a rotor disturbance model exists, regardless of whether or not the ISS disturbance model is implemented, as long as sensor measurement content does not include a large component with the ISS disturbance frequency. The Kalman gains for the rotor disturbance model can adjust in order to compensate for the excess motion caused by the “unknown” disturbance source; the ISS disturbance is “unknown” to the filter since it is not modeled within the filter. With this said, the rotor-disturbance-only model can be improved upon with the modeling of the ISS disturbance, especially for the case where the relative measurement contains motion at the ISS disturbance frequency. Another compensation method would be to force the motion of the shroud to minimize the difference between the estimated relative measurement and the actual relative measurement. Error in shroud state estimation is of no concern since it is not an ABS controller input.

The following plots show for each level of disturbance modeling fidelity: 1) A comparison of the 1st 10 seconds (left) and the last 10 seconds (right) of the actual and estimated value of x_r (Figure 4-9 through Figure 4-12). 2) The actual amplitude error and the error bounds produced by the square root of the error covariance value (Figure 4-13 through Figure 4-16).

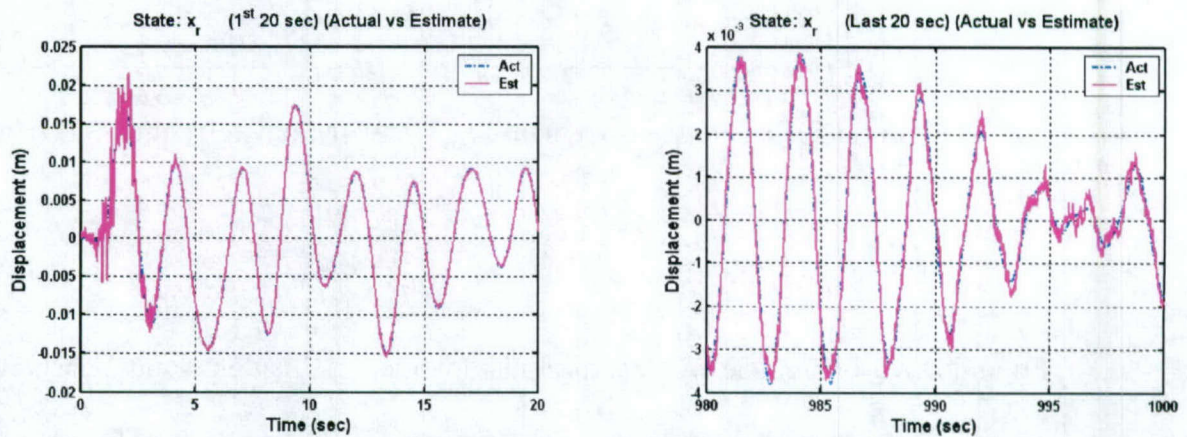


Figure 4-9. Results of Implementation of All Disturbance Models

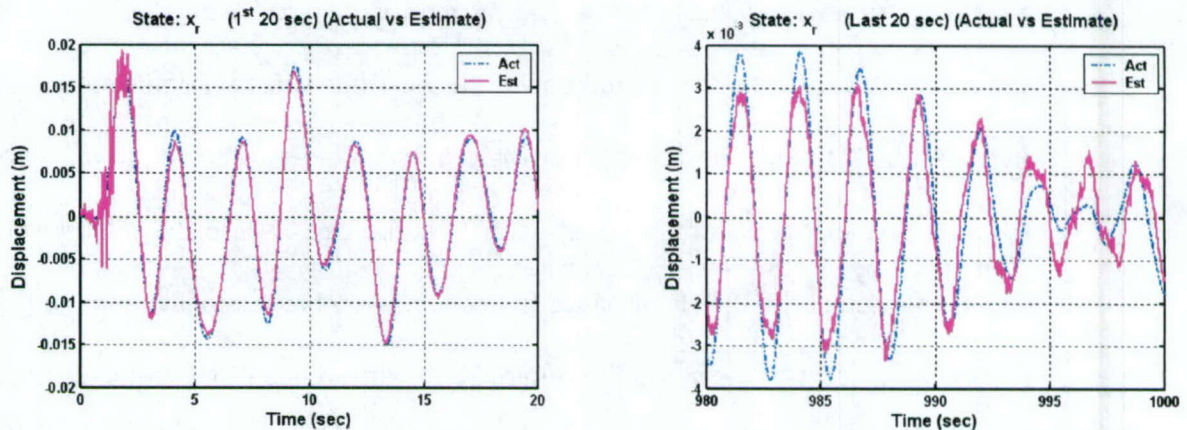


Figure 4-10. Results of Implementation of Only Rotor Disturbance Model

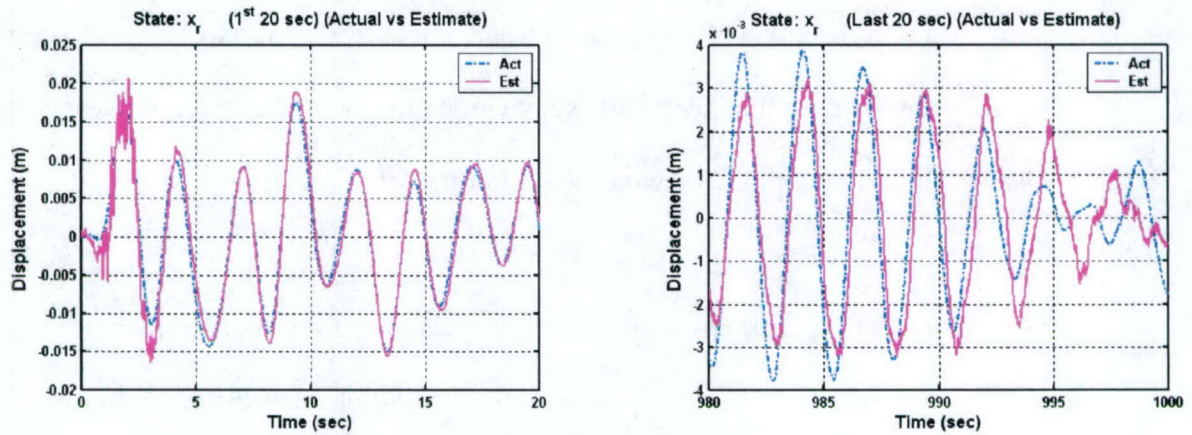


Figure 4-11. Results of Implementation of Only ISS Disturbance Model

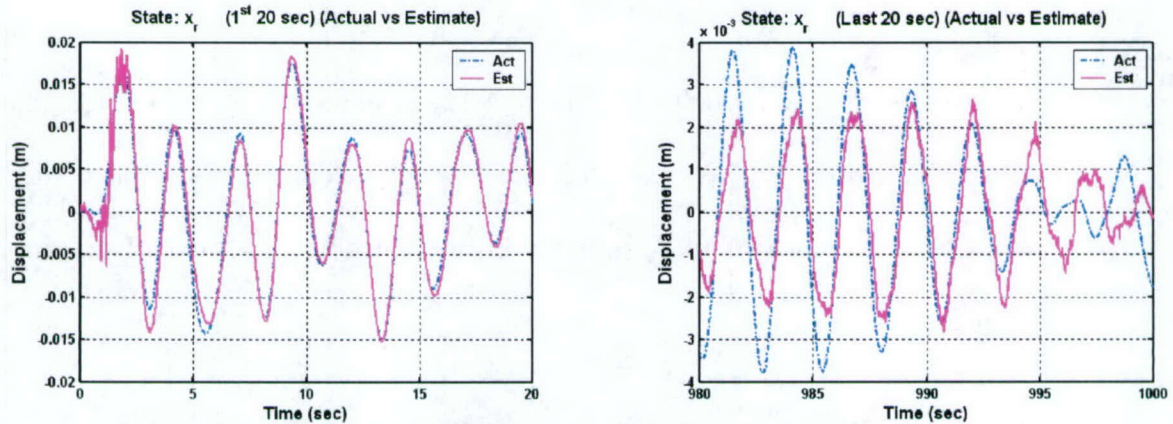


Figure 4-12. Results of Implementation of No Disturbance Models

The Kalman filter estimate converges very quickly (within 5 seconds) to the actual state in all four different disturbance modeling fidelity levels. As expected, when all of the disturbances that are applied to the plant are being modeled within the filter model, good estimation is achieved (Figure 4-9). Also, the estimation error is well within the one standard deviation envelope 100% of the time (Figure 4-13).

The lack of ISS disturbance modeling in the Only Rotor Disturbance Model (Figure 4-10) creates amplitude error between the actual and the estimated rotor state. The estimation error cycles in and out of being within one standard deviation of expected error (Figure 4-14). This shows that there are some problems with the filter process when no ISS disturbance is being modeled within the filter model.

When the rotor disturbance is not modeled within the filter model, there seems to be some phase error due to the lack of information of the rotor disturbance within the filter model (Figure 4-11). This causes the cycling estimation error (Figure 4-15) to stray further from the error standard deviation envelope and for longer periods of time when compared to the result for the Only Rotor Disturbance Model results shown in Figure 4-14.

The No Disturbance Models test (Figure 4-12) resulted in both phase error and amplitude error, which combined to create the largest error. Poor estimation as evidenced by the increased occurrence of the estimation error exceeding the standard deviation envelope (Figure 4-16).

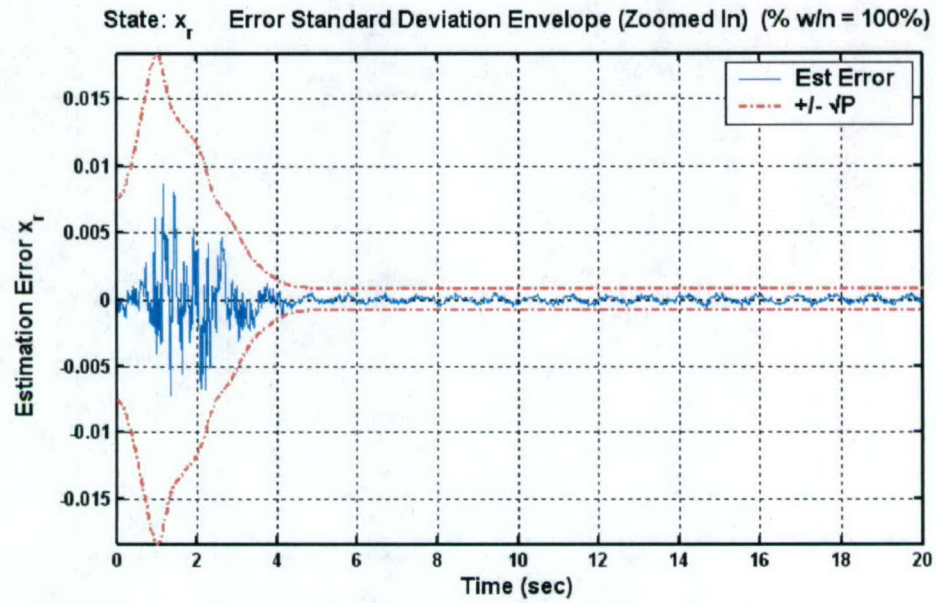


Figure 4-13. Standard Deviation Envelope Resulting from Implementation of All Disturbance Models

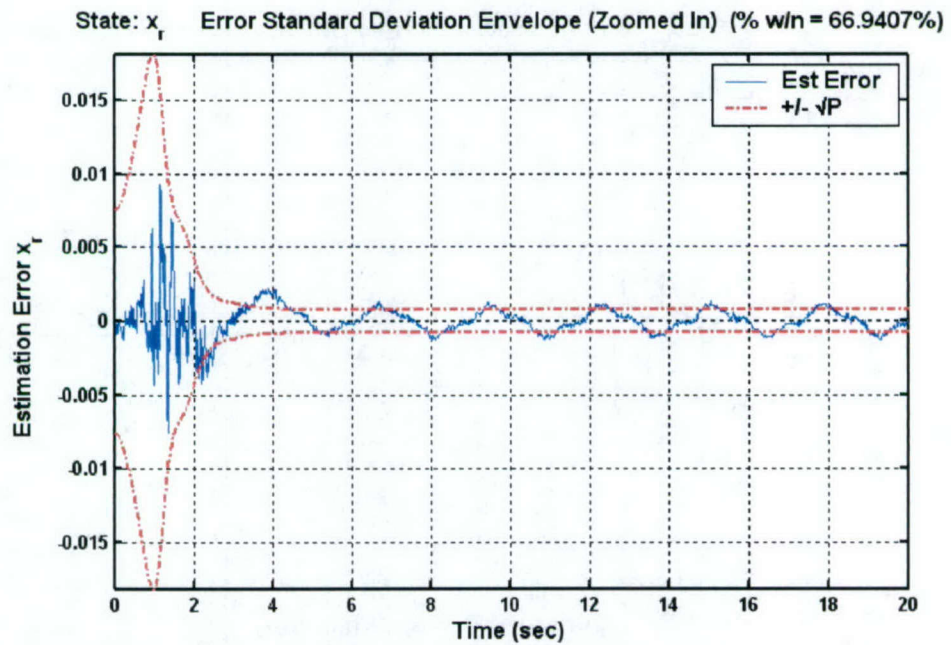


Figure 4-14. Standard Deviation Envelope Resulting from Implementation of Only Rotor Disturbance Model

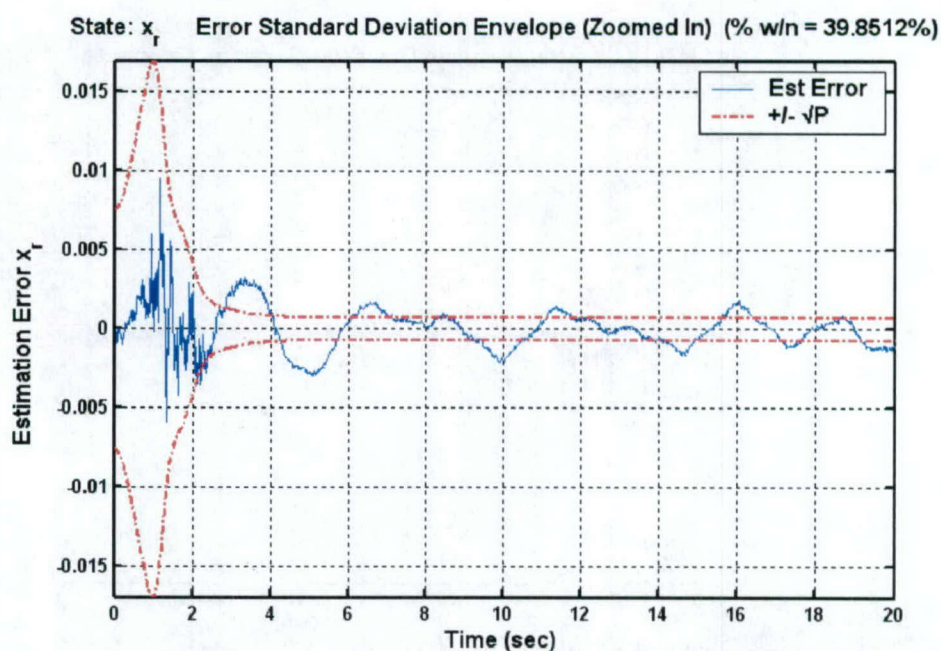


Figure 4-15. Standard Deviation Envelope from Implementation of Only ISS Disturbance Model

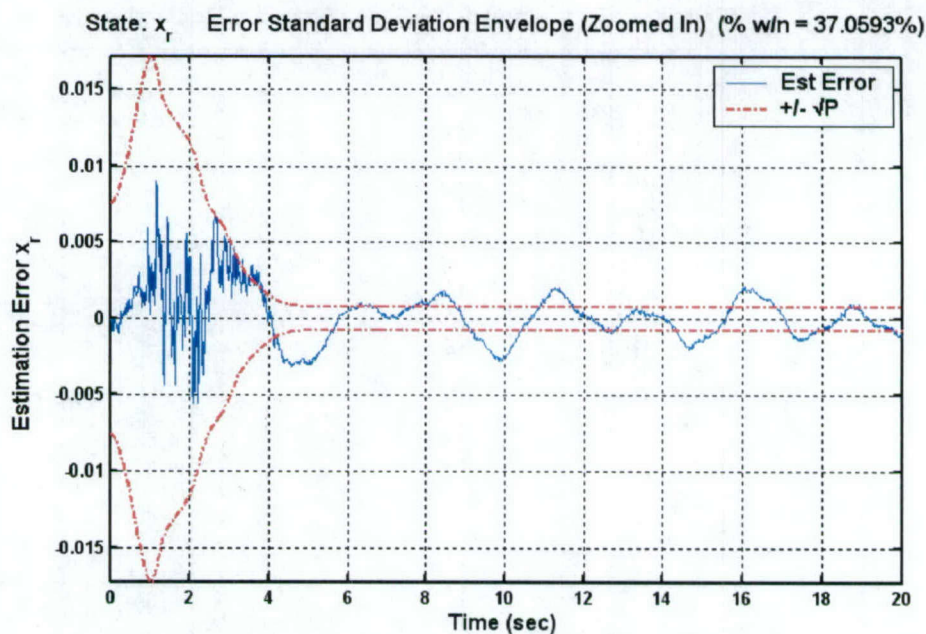


Figure 4-16 Standard Deviation Envelope from Implementation of No Disturbance Models

The error duration plots continue to prove that without the use of all disturbance models within the filter, poor estimation will result.

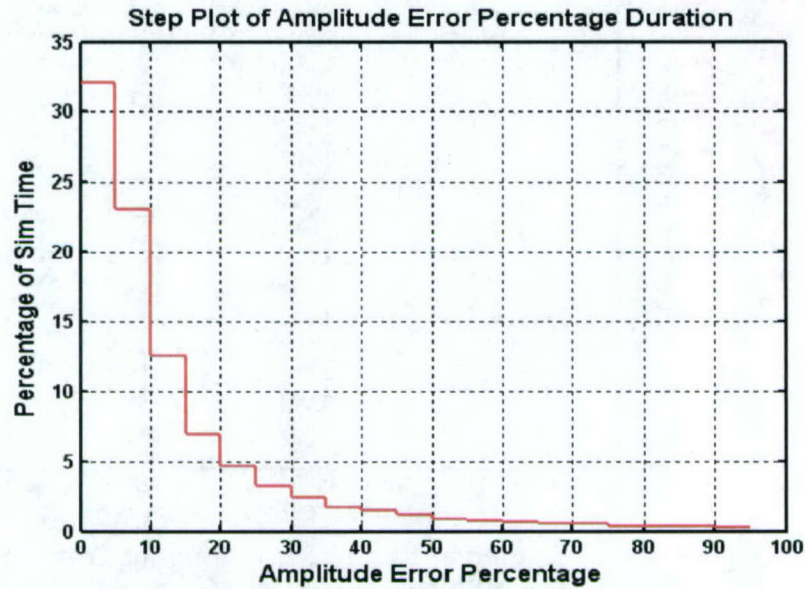


Figure 4-17. Duration of Error of x_r Estimation from Implementation of All Disturbance Models

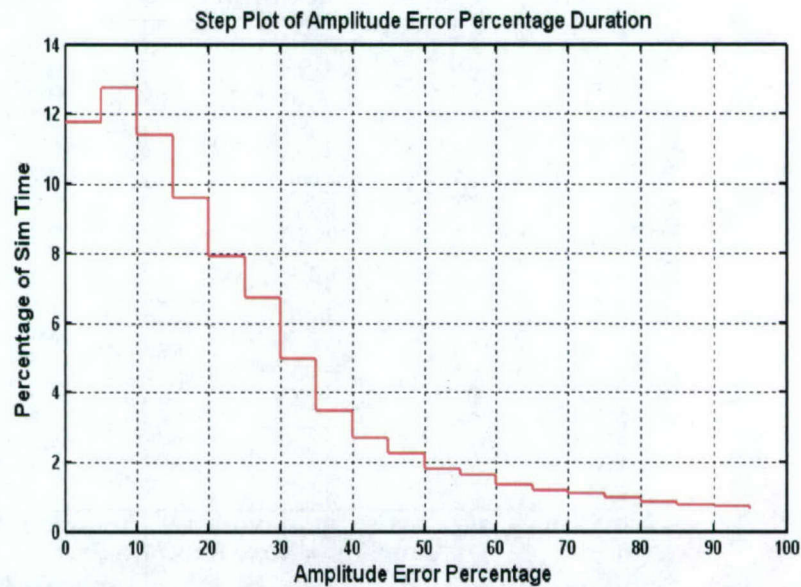


Figure 4-18. Duration of Error of x_r Estimation from Implementation of Only Rotor Disturbance Model

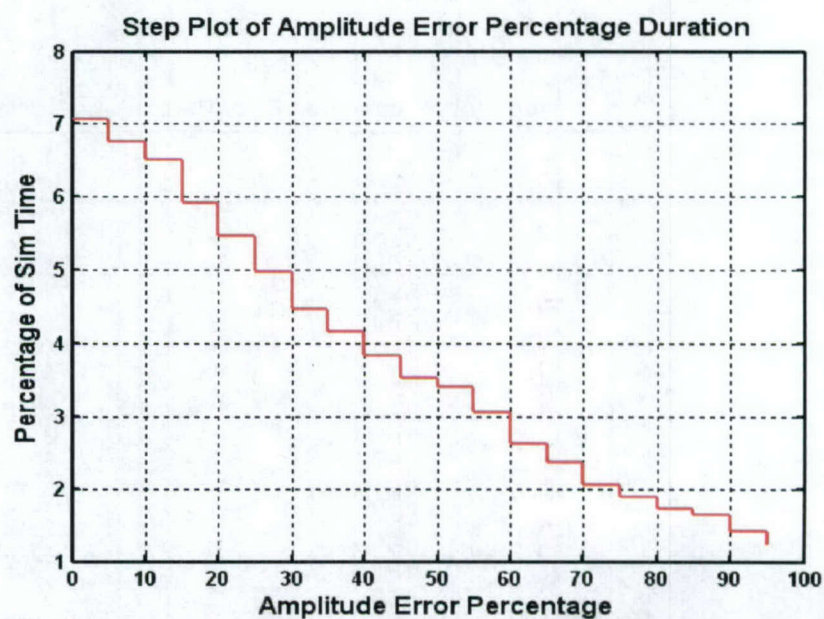


Figure 4-19. Duration of Error of x_r Estimation from Implementation of Only ISS Disturbance Model

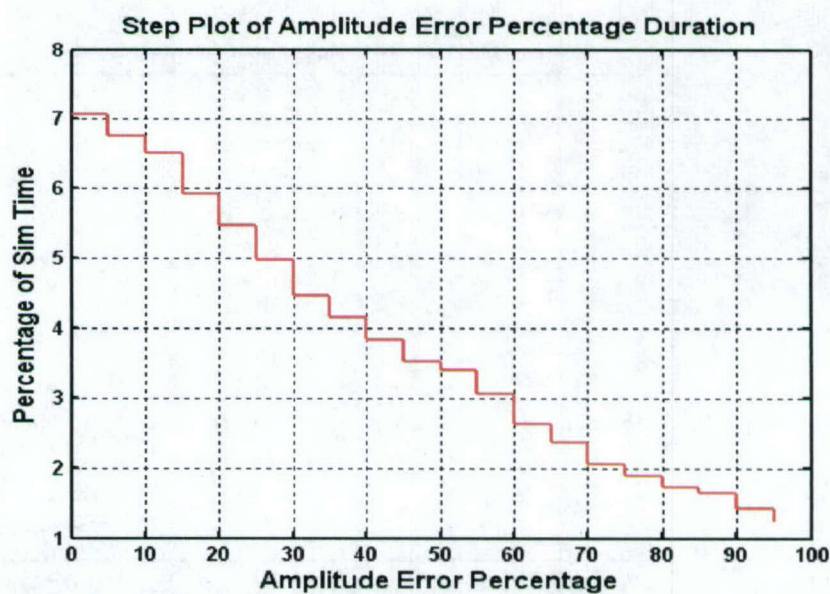


Figure 4-20. Duration of Error of x_r Estimation from Implementation of No Disturbance Models

As the disturbance modeling fidelity decreases, the percent amplitude error durations become more distributed. For instance, when all disturbances are modeled, ~55% of the simulation time had an error of under 10%, while only ~14% of the simulation time was under 10% error when using no disturbance models.

4.3.3 ISS Model 2 Testing: Increased Disturbance Frequency Range Test

These tests attempt to answer the question: Will the use of additional disturbance states increase the range of ISS disturbance frequencies under which the Kalman filter is able to operate? This question is answered by comparing the performance of ISS Model 1 to ISS Model 2. The rotor disturbance frequency was set to 0.399 Hz, when focusing on x and ϕ_y dofs, and set to 0.101 Hz when focusing on y and ϕ_x dofs. These frequencies are the peak modes in the following transfer functions: ISS disturbance in the x -axis to x_{rel} measurement (d_{xs} to x_{rel}) and ISS disturbance in the y -axis to y_{rel} measurement (d_{ys} to y_{rel}), respectively. See Figure 4-21 for more details. Since the peak frequencies are being used, the coupled motions (x and ϕ_y) and (y and ϕ_x) will have the greatest amplitude when excited by those frequencies with respect to the other degrees of freedom. Each axis will be examined separately to help provide clear result from which sound conclusions can be drawn.

4.4 ISS Model 2 Test Set-Up

The ISS translation and rotational disturbance frequencies for each test can be found in Table 4-7. In summary, the ISS translational disturbance frequencies were set to 90% of the rotor disturbance frequency for Test A and 110% of the rotor disturbance frequency for test B.

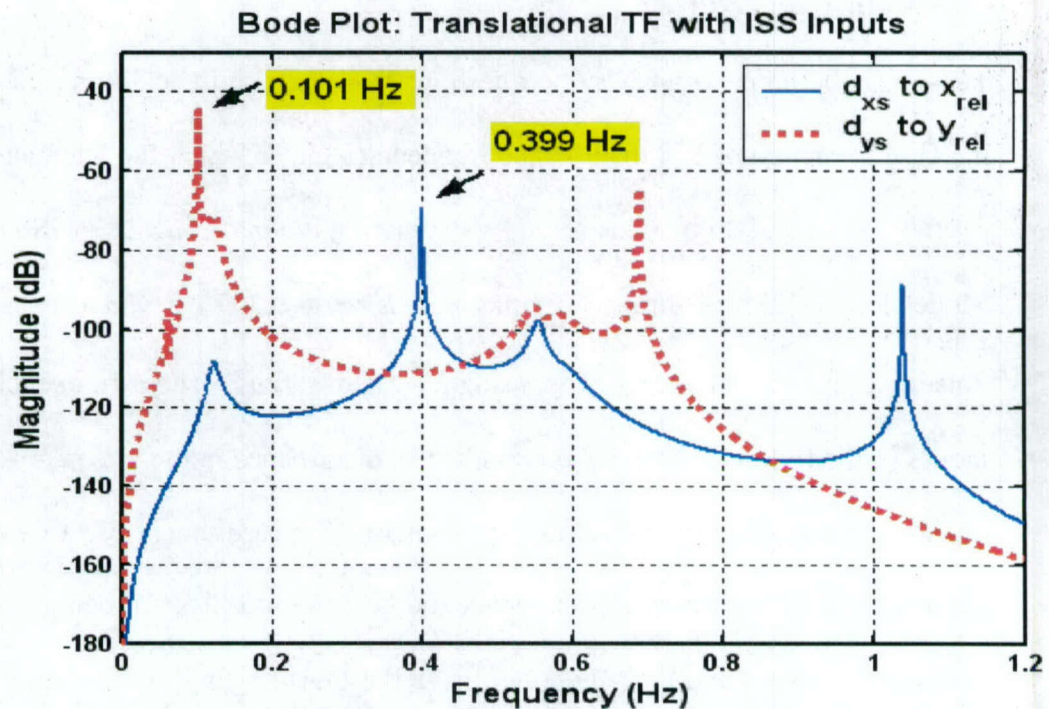


Figure 4-21. Bode Plots Used For Rotor Disturbance Frequencies

As for the rotational ISS disturbance frequencies, when focusing on x and ϕ_y , the rotational ISS disturbance frequency was centered on the peak mode frequency (0.79 Hz) of the transfer function from the rotational ISS disturbance about the y axis to the ϕ_{yrel} measurement ($d_{\phi_{ys}}$ to ϕ_{yrel}). The rotational ISS disturbance frequency was set to 90% of this peak value (0.711 Hz) for Test A and 110% of this peak value (0.869 Hz) for Test B.

When focusing on y and ϕ_x , the rotational ISS disturbance frequency was centered on the peak mode frequency (0.6 Hz) of the transfer function from the rotational ISS disturbance about the y axis to the ϕ_{yrel} measurement ($d_{\phi_{ys}}$ to ϕ_{yrel}). The rotational ISS disturbance frequency was set at 90% of this peak value (0.54 Hz) for Test A and 110% of this peak value (0.66 Hz) for Test B.

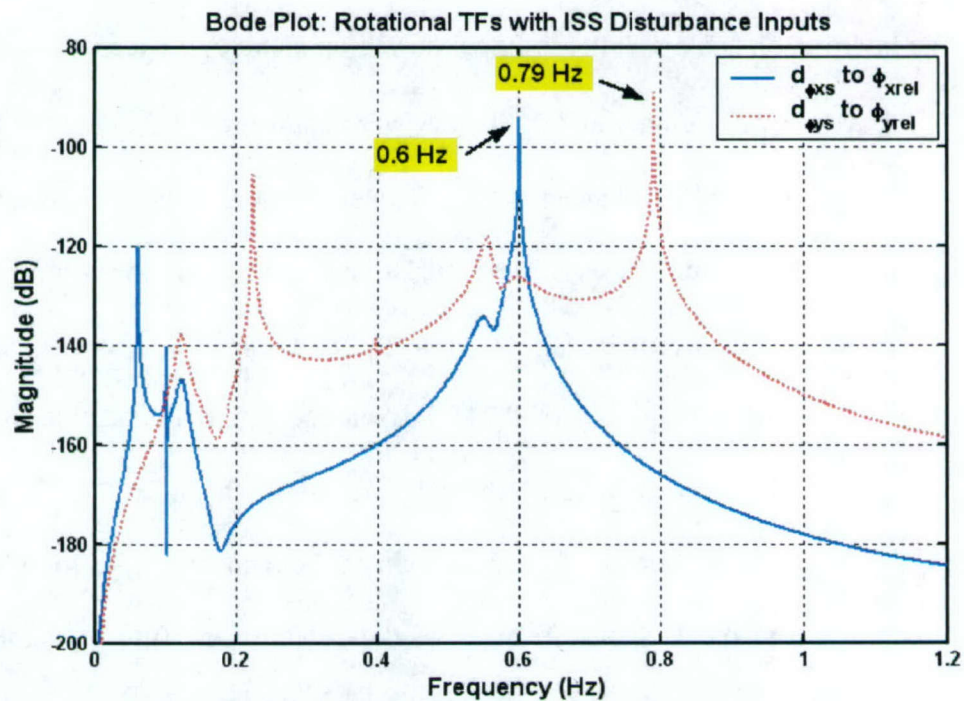


Figure 4-22. Bode Plots Used For ISS Rotational Disturbance Center Frequencies

ISS Model 2 has both “90%” and “110%” frequencies modeled, while ISS Model 1 has only the “90%” frequencies modeled. All of these frequencies are summarized in Table 4-7. A second set of tests were run incorporating a rotor spin-up from 0 to 0.7 Hz over 300 seconds.

Units: Hz		Rotor Spin Frequency (ω_{spin})	ISS disturbance Frequencies Applied to Plant		ISS Model 1 (4 d_{ISS} Filter States)		ISS Model 2 (8 d_{ISS} Filter States)			
			ω_t applied	ω_r applied	90% Frequencies		Both 90% and 110% Frequencies			
					ω_{dst1}	ω_{dsr1}	ω_{dst1}	ω_{dst2}	ω_{dsr1}	ω_{dsr2}
x and ϕ_y	Test A (90% Freq)	0.399	0.359	0.711	0.359	0.711	0.359	0.439	0.711	0.869
	Test B (110% Freq)		0.439	0.869						
y and ϕ_x	Test A (90% Freq)	0.101	0.091	0.54	0.091	0.54	0.091	0.111	0.54	0.66
	Test B (110% Freq)		0.111	0.66						
x and ϕ_y (w/spin-up)	Test A (90% Freq)	0.399	0.359	0.711	0.359	0.711	0.359	0.439	0.711	0.869
	Test B (110% Freq)		0.439	0.869						
y and ϕ_x (w/spin-up)	Test A (90% Freq)	0.101	0.091	0.54	0.091	0.54	0.091	0.111	0.54	0.66
	Test B (110% Freq)		0.111	0.66						

Table 4-7. Test Matrix

To interpret of Table 4-7, the testing focusing on x and ϕ_y proceeded as follows:

- 1) Focusing on x and ϕ_y , Test A was conducted by exciting the 32 state plant with 4 rotor disturbances with a frequency equal to the spin rate (0.399 Hz), and 4 ISS disturbances. The translational ISS disturbances are pulse trains with a frequency of 0.359 Hz while the rotational ISS disturbances are pulse trains with a frequency of 0.711 Hz. These two frequencies have been labeled the “90%” frequencies. The relative measurement, x_{rel} , is fed into two different Kalman Filters. The first Kalman filter includes the rotor disturbance model and the ISS (disturbance) Model 1 within the filter dynamics. ISS Model 1 contains information about the two ISS disturbance frequencies applied (0.359 and 0.711 Hz, the 90% frequencies). The second Kalman Filter includes the rotor disturbance model and the ISS (disturbance) Model 2 within the filter dynamics. ISS Model 2 contains knowledge of the same two ISS disturbance frequencies as modeled in ISS Model 1, the 90% frequencies, but also contains information about 2 additional ISS disturbance frequencies (0.439 and 0.869 Hz, the 110% frequencies). State estimation error, x_{4err} for ISS Model 1 and

x_{8err} for ISS Model 2, are computed by taking the difference from the estimated states from ISS Model 1, \hat{x}_4 , and the estimated states from ISS Model 2, \hat{x}_8 , and actual state, x , in order to determine performance.

- 2) Again focusing on x and ϕ_y , Test B was conducted by exciting the 32 state plant with 4 rotor disturbances with a frequency equal to the spin rate (0.399 Hz), and 4 ISS disturbances as was done in Test A, but this time, the translational ISS disturbance pulse trains are input at a frequency of 0.439 Hz while the rotational ISS disturbances are input at a frequency of 0.869 Hz. These two frequencies have been named the “110%” frequencies. The output of the plant, the relative measurement (x_{rel}), is fed into the same two Kalman Filters as in Test A, and the process used to determine performance is also the same

These same two tests are also run while focusing on y and ϕ_x dofs. The testing algorithm is shown in Figure 4-23.

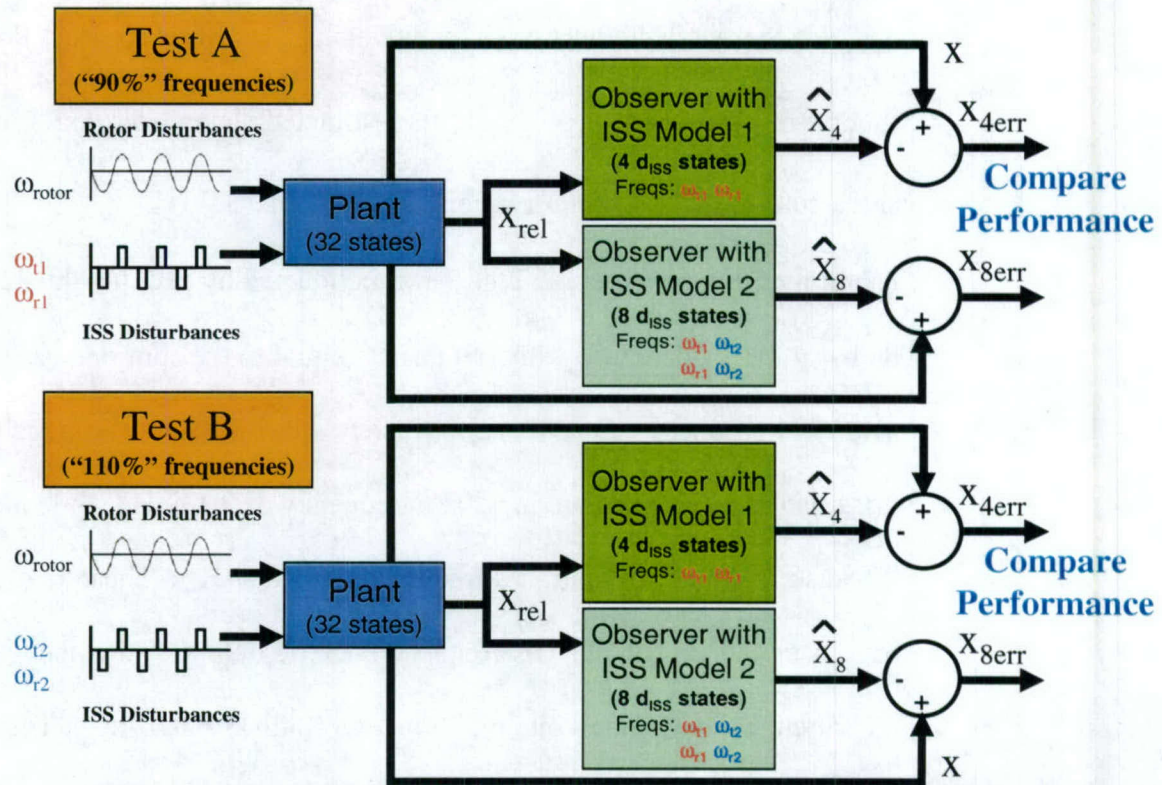


Figure 4-23. Testing Algorithm for Improving Operational Bandwidth

The expectation for Test A is that both Kalman filters should produce similar errors. ISS Model 2 may have slightly higher error due to the fact that it is modeling a disturbance frequency that does not exist, but the filter gains that error state so the amplitude of the force with the unapplied frequency is very small. For Test B, the expectation is that the error in ISS Model 2 should be much less than in ISS Model 1. This is due to the fact that ISS Model 1 does not have the "110%" ISS disturbance frequency information modeled within the filter dynamics, while the ISS Model 2 does. See Figure 4-24 for a logic flow diagram that sums up the previous discussion.

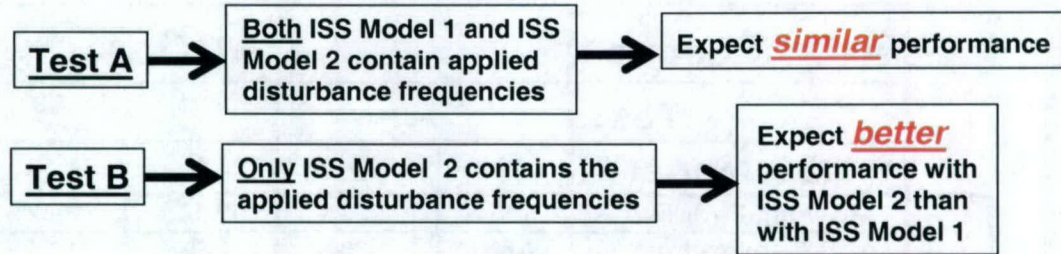


Figure 4-24. Logic Flow Diagram for Testing Regimen

The test results found in Section 4.4.1 confirm this hypothesis.

4.4.1 ISS Model 2 Test Results: Focusing on x and ϕ_y

When focusing on x and ϕ_y , the following frequencies were used for Test A and Test B.

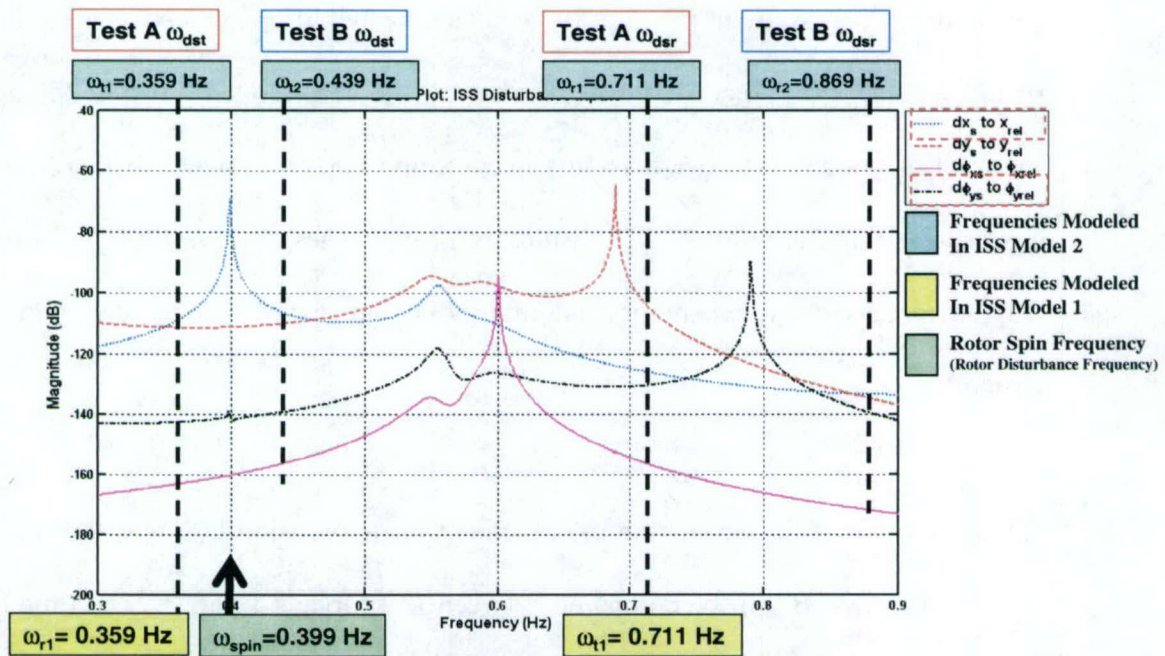


Figure 4-25. Disturbance Frequencies Used when Focusing on x and ϕ_y

The results from focusing on coupled x and ϕ_y rotor motion, without spin-up, can be found in Table 4-8.

	Axis of Focus :	x and ϕ_y				
	Test:	A		B		
	ISS Model #:	1	2	1	2	% imp
Rotor States	% Amp Error (x_r)	6.57%	6.85%	17.18%	3.62%	78.93%
	% Amp Error (y_r)	1.52%	1.53%	1.20%	1.18%	2.16%
	% Amp Error (ϕ_{xr})	0.74%	0.74%	1.08%	1.03%	5.01%
	% Amp Error (ϕ_{yr})	1.21%	1.13%	7.02%	0.67%	90.44%

Table 4-8. Test Results Focusing on x and ϕ_y (no spin-up)

As predicted, the percent amplitude error, calculated with equation (4-1), is nearly identical for both ISS Model 1 and ISS Model 2 for the Test A case. Also as expected, during Test B, ISS Model 2 shows a percent amplitude error improvement over ISS Model 1 for all rotor states, and the largest improvements are for the x_r and ϕ_{yr} dofs as predicted. The percent improvement (% imp) is calculated as the difference between the ISS Model 1 result and the ISS Model 2 result divided by the ISS Model 1 result, therefore it is a measure of percent improvement in percent amplitude error over the ISS Model 1 error. This shows that the range of ISS disturbance frequencies that the filter will operate under can be increased by expanding and improving the disturbance model within the filter dynamics.

As an example of the estimation improvement made by using ISS Model 2, the estimation of x_r during Test B will be compared between ISS Models 1 and 2. The time history plot comparisons are shown in Figure 4-26 and Figure 4-27, the estimation error envelope comparisons are shown in Figure 4-28 and Figure 4-29, and the error duration comparisons are shown in Figure 4-30 and Figure 4-31

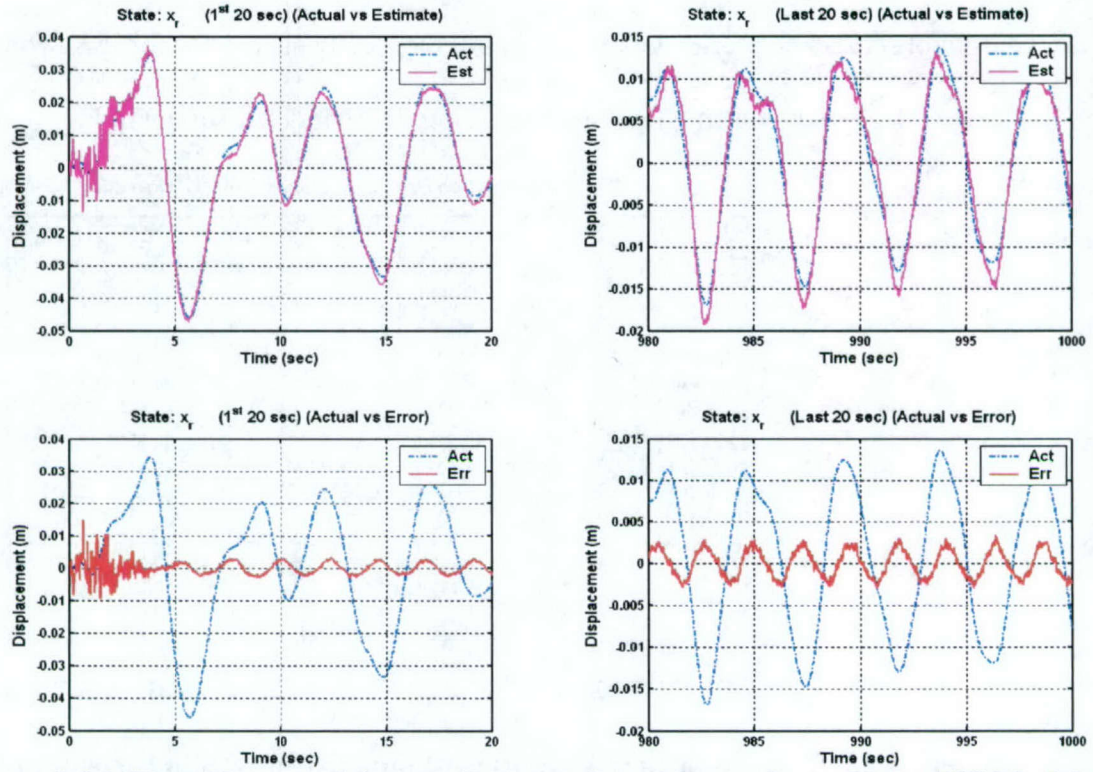


Figure 4-26. Time History of Actual, Estimated, and Error for x_r Using ISS Model 1

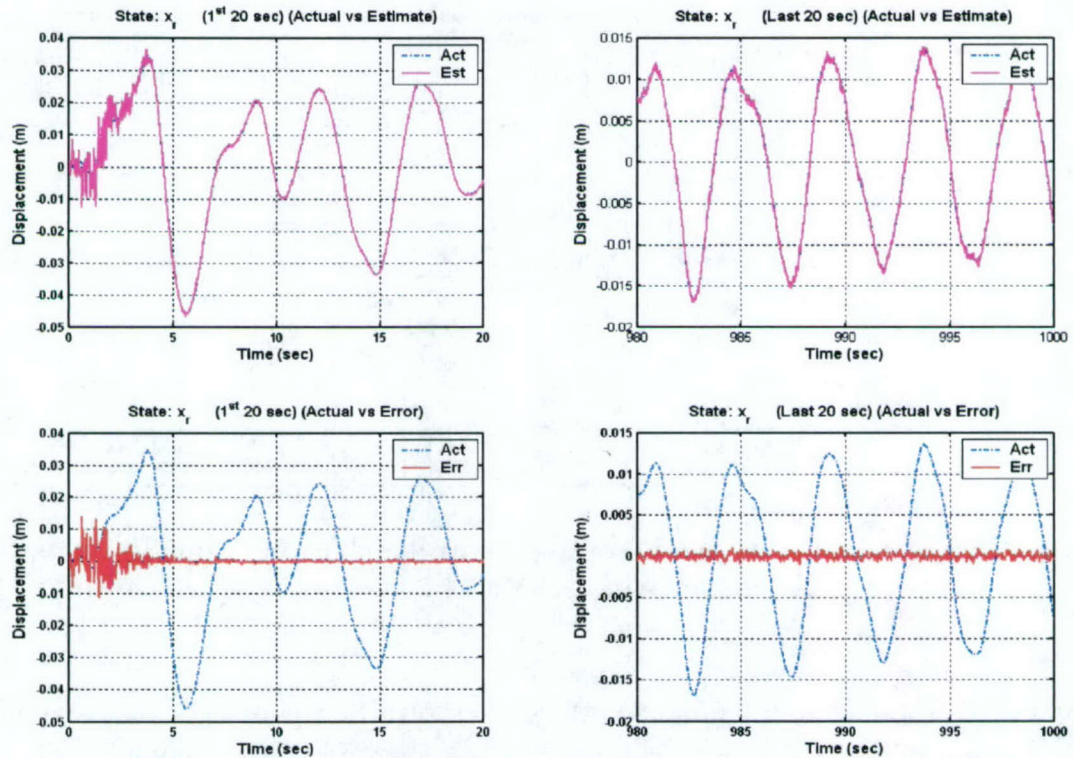
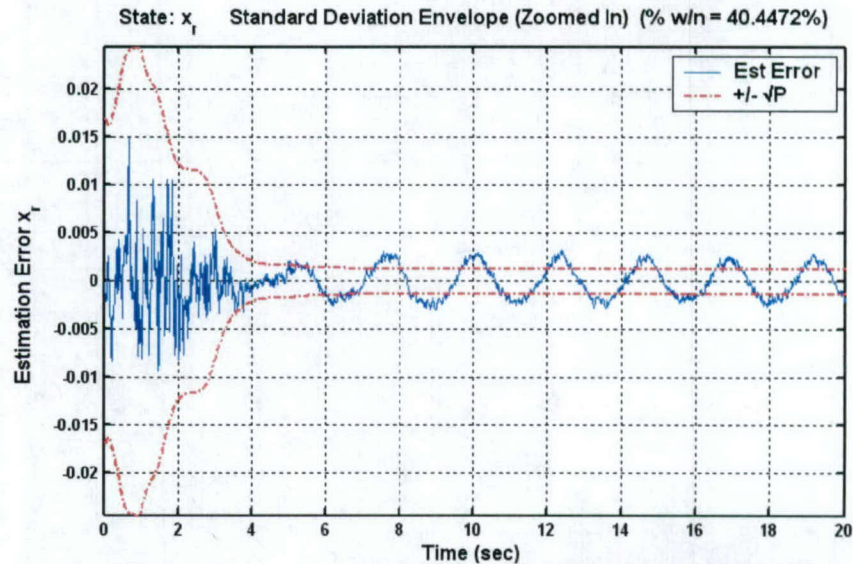
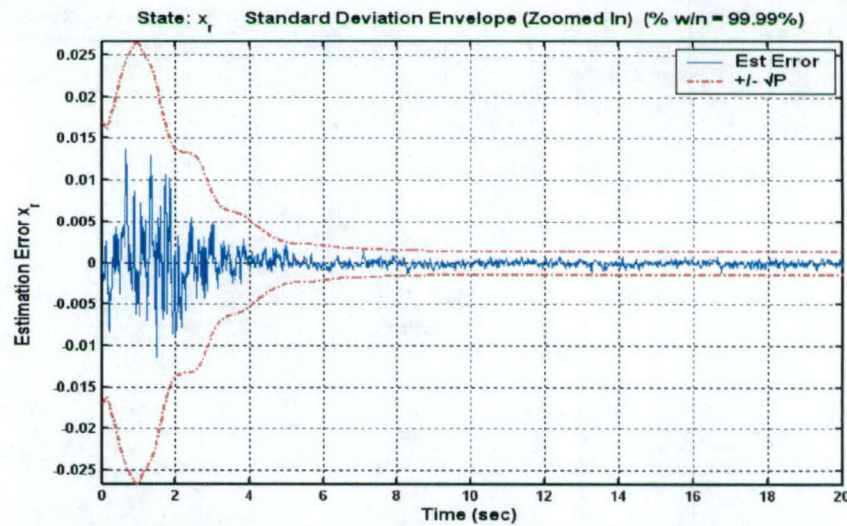


Figure 4-27. Time History of Actual, Estimated, and Error for x_r Using ISS Model 2

Both observers converge very quickly, but the steady state error for ISS Model 2, shown in Figure 4-27, is much smaller than when using ISS Model 1, shown in Figure 4-26.



**Figure 4-28. Estimation Error and Error Standard Deviation Envelope of x_r
Estimation with ISS Model 1**



**Figure 4-29. Estimation Error and Error Standard Deviation Envelope of x_r
Estimation with ISS Model 2**

The estimation error for ISS Model 1, shown in Figure 4-28, stays within the standard deviation envelope only 40.44% of the time while the estimation error for ISS Model 2,

shown in Figure 4-29, stays within the standard deviation envelope nearly 100% of the time, showing the superior estimation capabilities when using ISS Model 2.

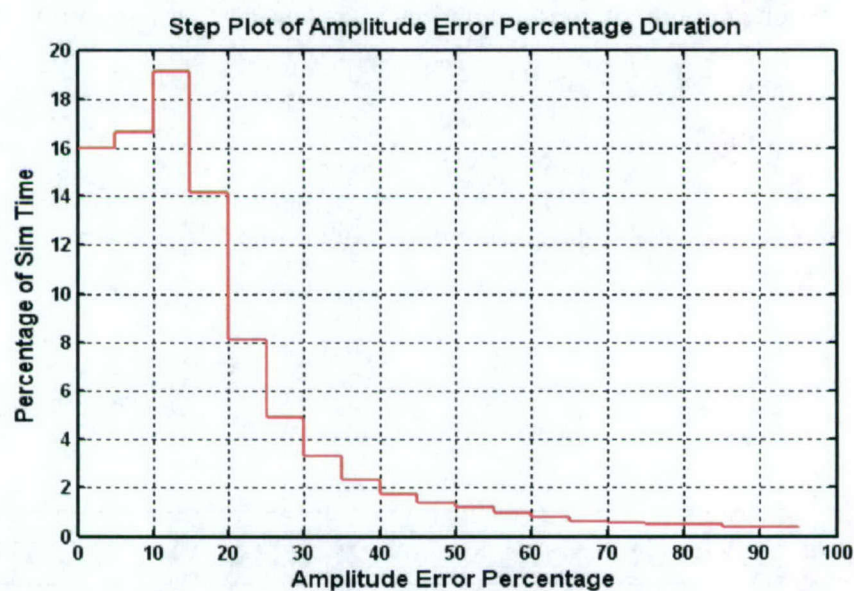


Figure 4-30. Duration of Error of x_r Estimation with ISS Model 1

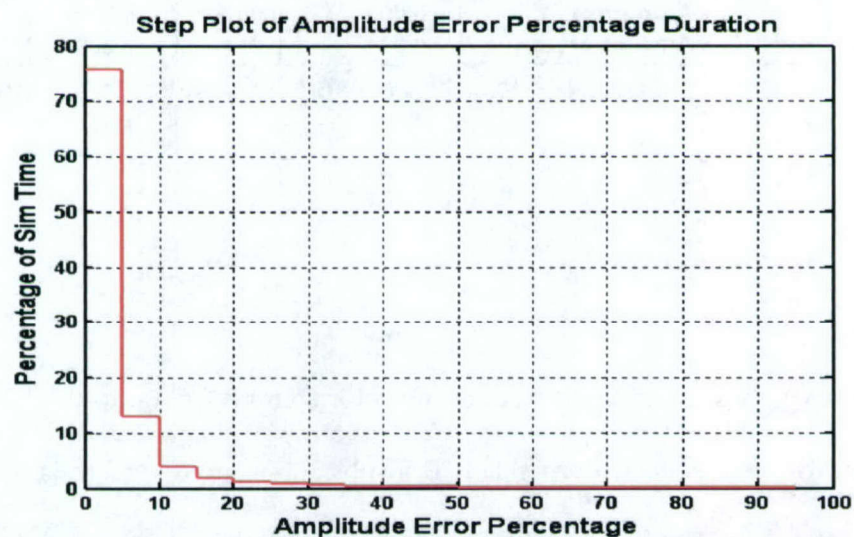


Figure 4-31. Duration of Error of x_r Estimation with ISS Model 2

Figure 4-31 shows that state estimation is close at all times when using ISS Model 2. In fact over 75% of the simulation time has an estimation amplitude error less than 5%, and nearly 100% of the simulation time experiences an error of less than 20%. However, when using ISS Model 1, Figure 4-30, there is a greater distribution of error durations. In fact, a significant amount of the simulation time has a resulting estimation amplitude error of greater than 30%.

Results with a rotor spin-up can be found in Table 4-9 below.

	Axis of Focus :	x and ϕ_y w/ spin-up				
	Test:	A		B		
	ISS Model #:	1	2	1	2	% imp
Rotor States	% Amp Error (x_r)	20.20%	20.89%	50.53%	9.14%	81.90%
	% Amp Error (y_r)	0.01%	0.01%	0.05%	0.01%	89.42%
	% Amp Error (ϕ_{xr})	0.00%	0.00%	0.00%	0.00%	20.00%
	% Amp Error (ϕ_{yr})	2.84%	2.75%	7.30%	1.57%	78.45%

Table 4-9. Results Focusing on x and ϕ_y (with spin-up)

The hypothesis also holds true during rotor spin-up from 0 to 0.7 Hz over 300 seconds. In fact, for rotor state x_r during Test B a substantial improvement is made from an amplitude error of 50.53% to an amplitude error of 9.14% with the use of ISS Model 2. The large percent improvement values for y_r and ϕ_{xr} , should be disregarded as it is a numerical

artifact, meaning that the values are very small and therefore any small changes will produce a large improvement, even though the actual improvement is minuscule.

As an example of the estimation improvement made by using ISS Model 2 with time-varying inputs and dynamics, the estimation of x_r during Test B will be compared between ISS Models 1 and 2. The time history plot comparisons are shown in Figure 4-32 and Figure 4-33, the estimation error envelope comparisons are shown in Figure 4-34 and Figure 4-35, and the error duration comparisons are shown in Figure 4-36 and Figure 4-37.

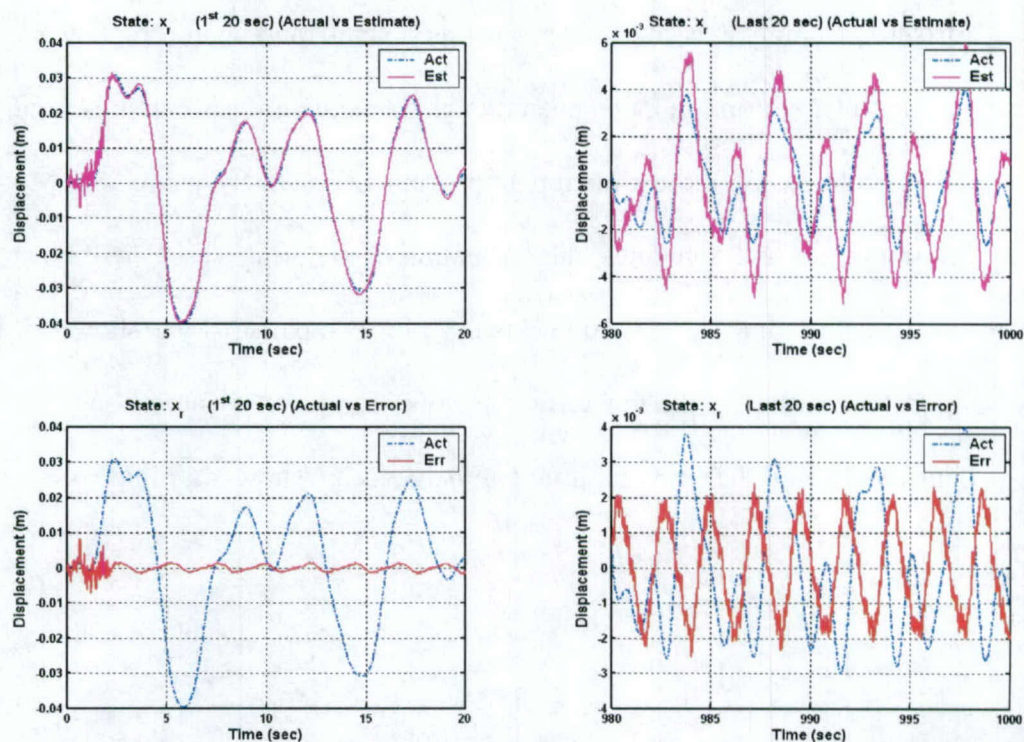


Figure 4-32. Time History of Actual, Estimated, and Error for x_r Using ISS Model 1 (with rotor spin-up)

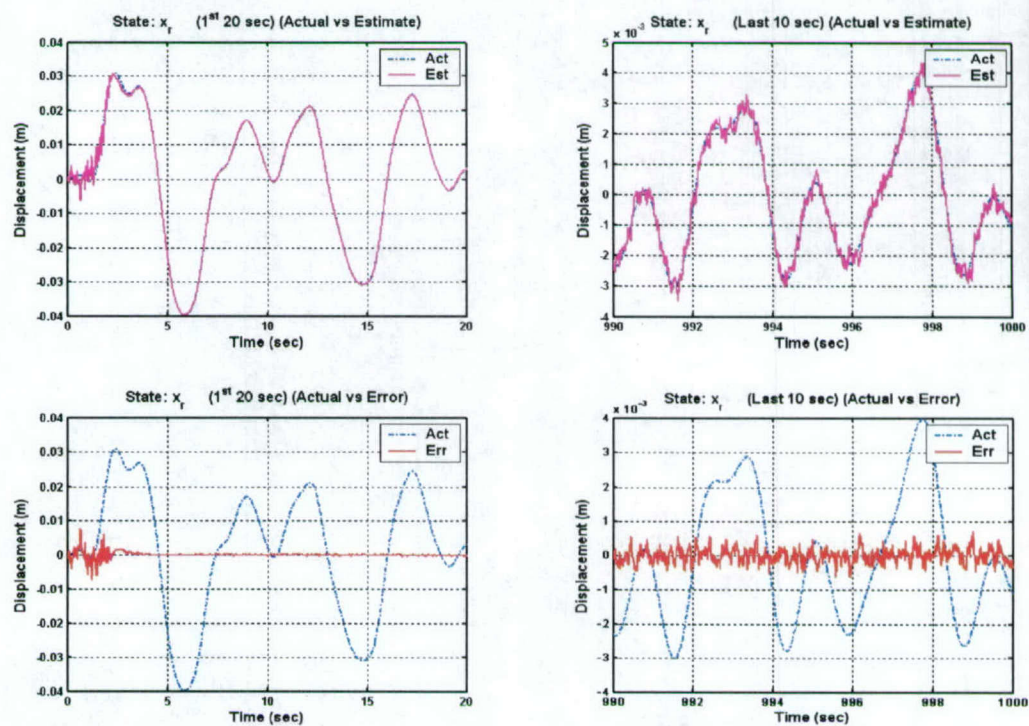


Figure 4-33. Time History of Actual, Estimated, and Error for x_r Using ISS Model 2 (with rotor spin-up)

Both observers converge very quickly, but the steady state error for ISS Model 2, Figure 4-33, is much smaller than when using ISS Model 1, Figure 4-32. The error when using ISS Model 1 is mainly due to amplitude estimation error rather than phase estimation error.

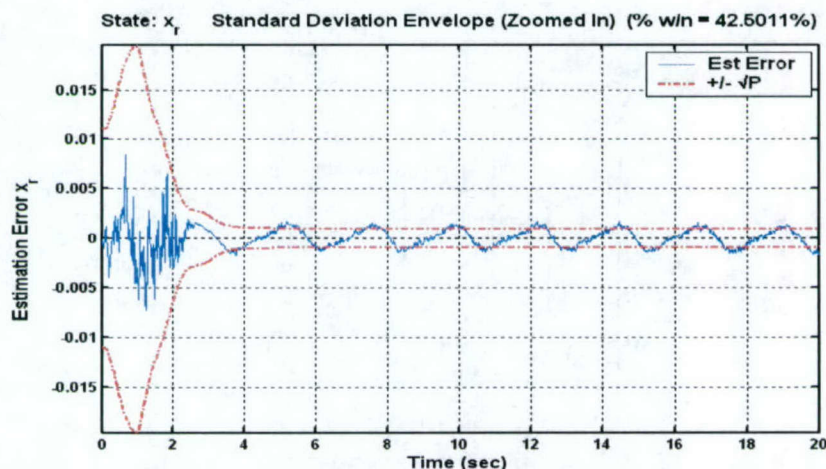


Figure 4-34. Estimation Error and Error Standard Deviation Envelope of x_r Estimation with ISS Model 1 (with rotor spin-up)

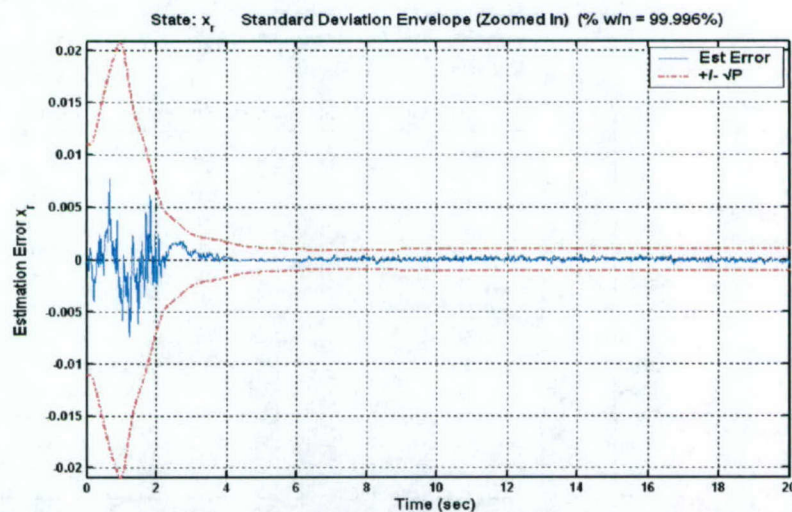


Figure 4-35. Estimation Error and Error Standard Deviation Envelope of x_r Estimation with ISS Model 2 (with rotor spin-up)

The estimation error for ISS Model 1, Figure 4-34, stays within the standard deviation envelope only 42.5% of the time while the estimation error for ISS Model 2, Figure 4-35, stays within the standard deviation envelope nearly 100% of the time, showing the superior estimation capabilities when using ISS Model 2.

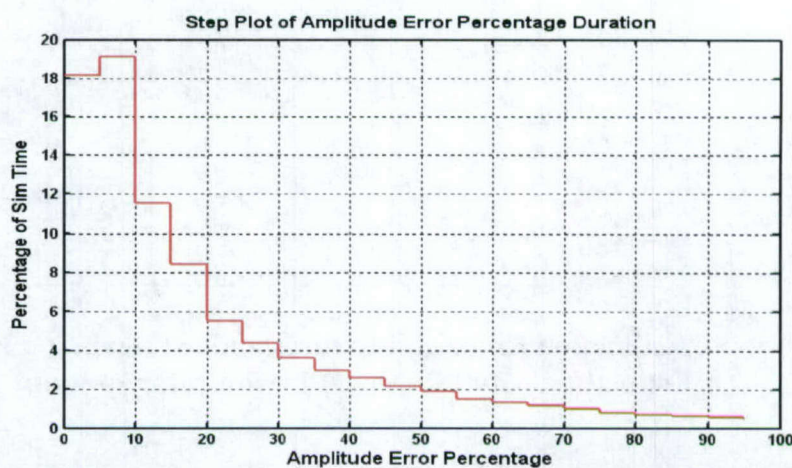


Figure 4-36. Duration of Error of x_r Estimation with ISS Model 1 (with rotor spin-up)

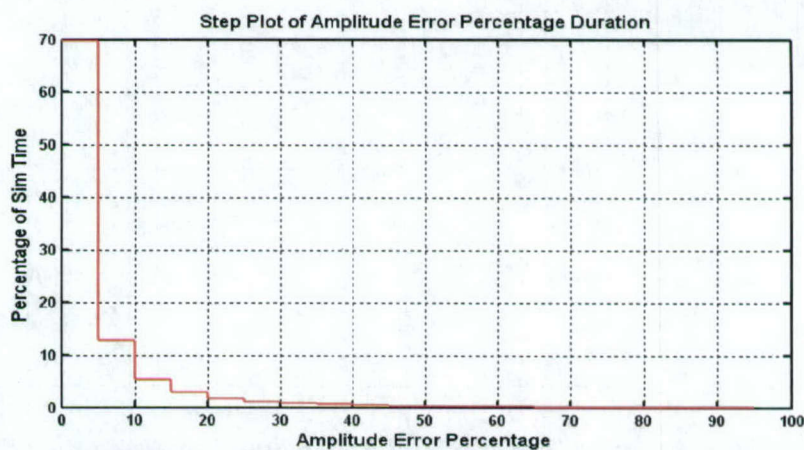


Figure 4-37. Duration of Error of x_r Estimation with ISS Model 2 (with rotor spin-up)

Figure 4-37 shows that state estimation is close at all times when using ISS Model 2. In fact nearly 70% of the simulation time has an estimation amplitude error less than 5%, and nearly 100% of the simulation time experiences an error of less than 20%. However, when using ISS Model 1, Figure 4-38, there is a greater distribution of error durations. In fact, a significant amount of the simulation time has a resulting estimation amplitude error of greater than 30%

4.4.2 ISS Model 2 Test Results: Focusing on y and ϕ_x

When focusing on y and ϕ_x , the following frequencies were used for Test A and Test B.

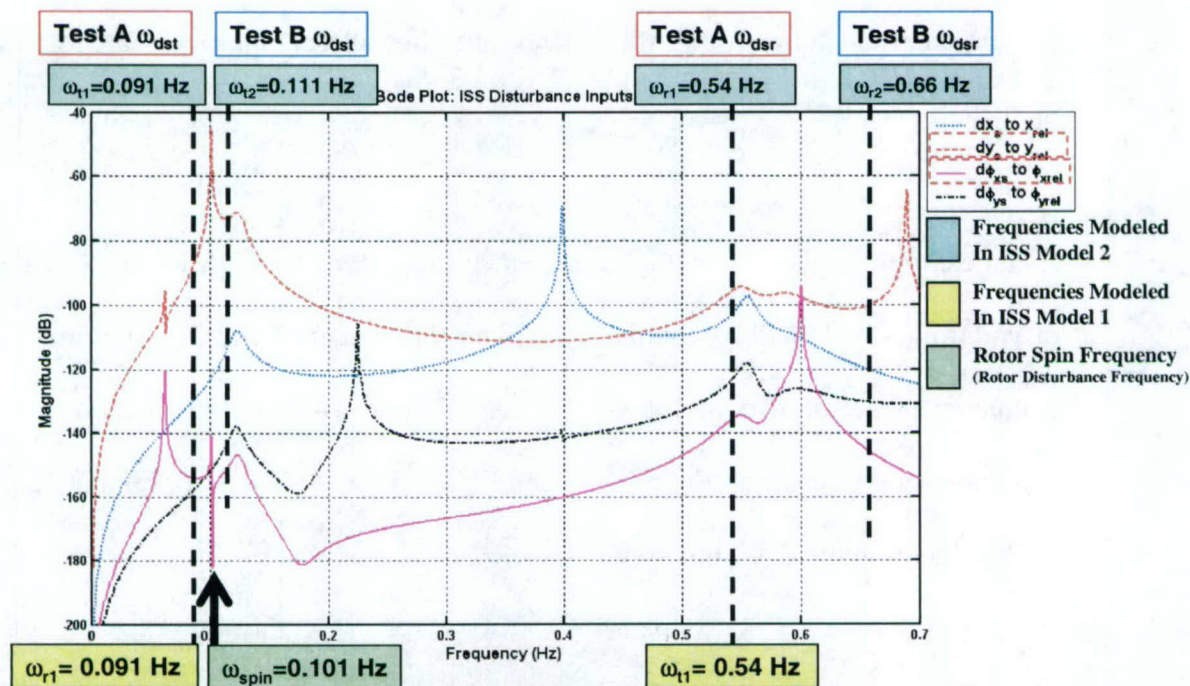


Figure 4-38. Disturbance Frequencies used when focusing on y and ϕ_x

The results from focusing on coupled y and ϕ_x rotor motion, without spin-up, can be found in Table 4-10.

	Axis of Focus :	y and ϕ_x				
	Test:	A		B		
	ISS Model #:	1	2	1	2	% imp
Rotor States	% Amp Error (x_r)	2.79%	2.79%	2.01%	2.00%	0.24%
	% Amp Error (y_r)	0.61%	0.75%	4.72%	0.78%	83.38%
	% Amp Error (ϕ_{xr})	0.58%	0.58%	3.67%	0.44%	87.99%
	% Amp Error (ϕ_{yr})	0.91%	0.92%	0.60%	0.59%	0.41%

Table 4-10. Results Focusing on y and ϕ_x (no spin-up)

Again as predicted, the percent amplitude error is nearly identical for the Test A case for both ISS Model 1 and ISS Model 2. Also, the Test B shows an improvement, in the percent amplitude error for all rotor states, and shows large improvements for y_r and ϕ_{xr} as predicted.

As an example of the estimation improvement made by using ISS Model 2, the estimation of y_r during Test B will be compared between ISS Models 1 and 2. The time history plot comparisons are shown in Figure 4-39 and Figure 4-40, the estimation error envelop comparisons are shown in Figure 4-41 and Figure 4-42, and the error duration comparisons are shown in Figure 4-43 and Figure 4-44.

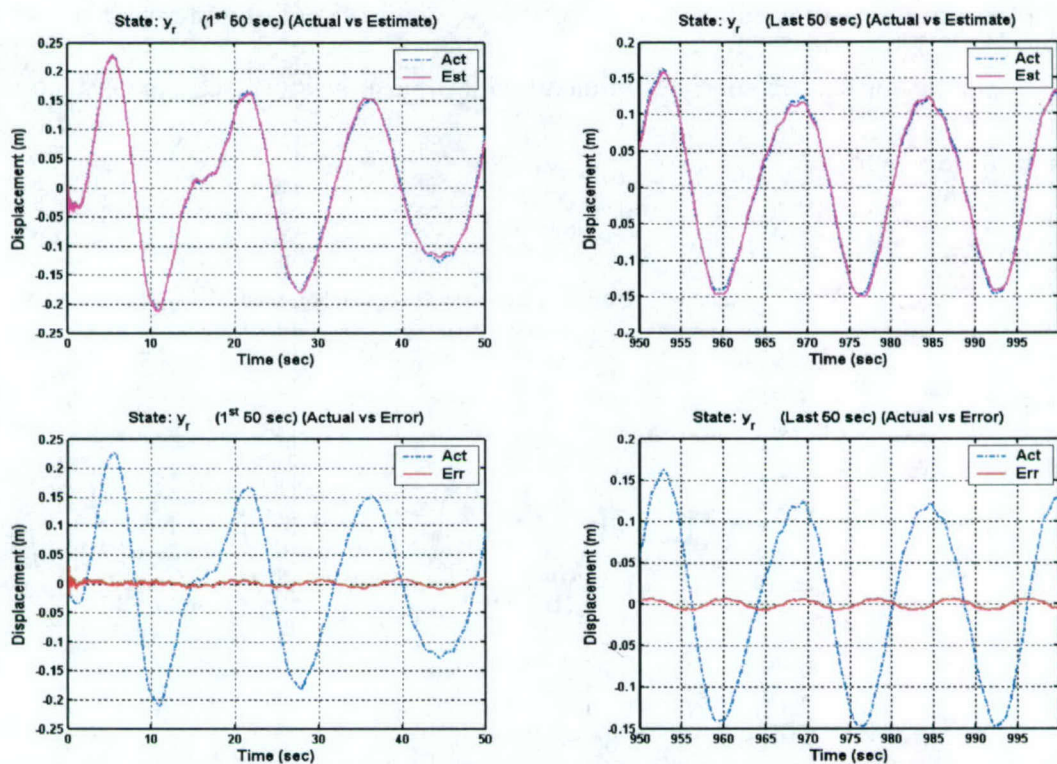


Figure 4-39. Time History of Actual, Estimated, and Error for y_r Using ISS Model 1

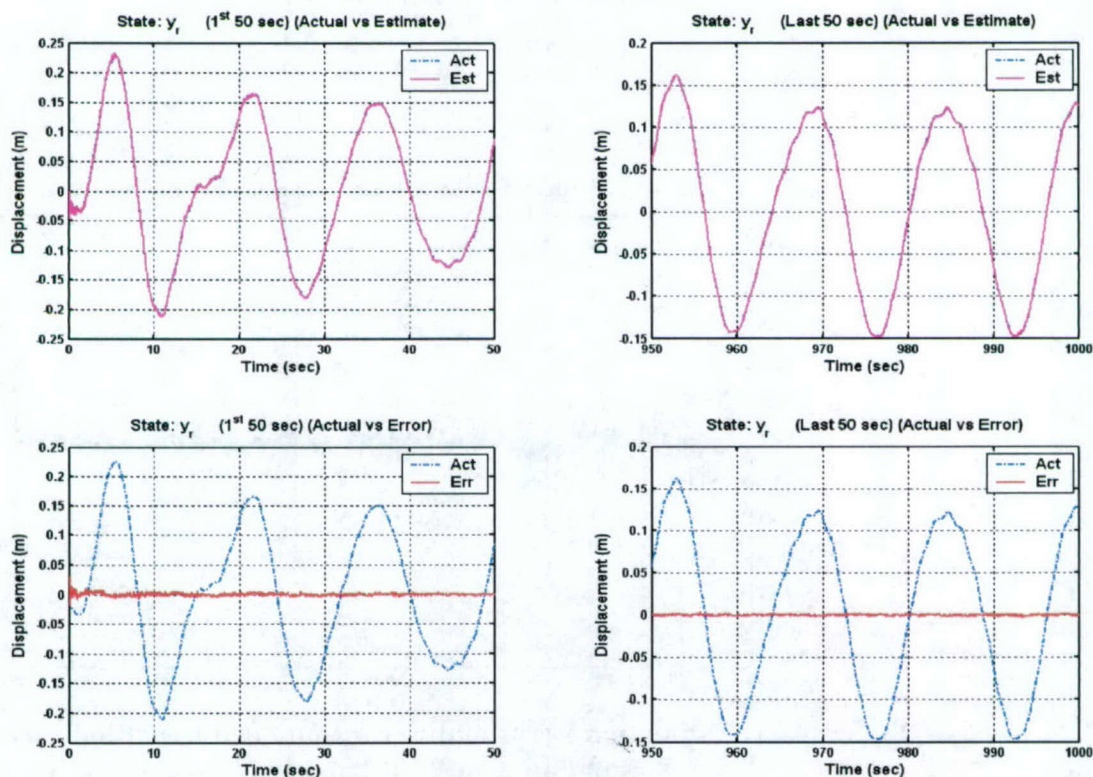


Figure 4-40. Time History of Actual, Estimated, and Error for y_r Using ISS Model 2

Event though the estimation using ISS Model 1 is good, Figure 4-40 shows that the steady state error can be nearly eliminated with the use of increased disturbance modeling found in ISS Model 2.

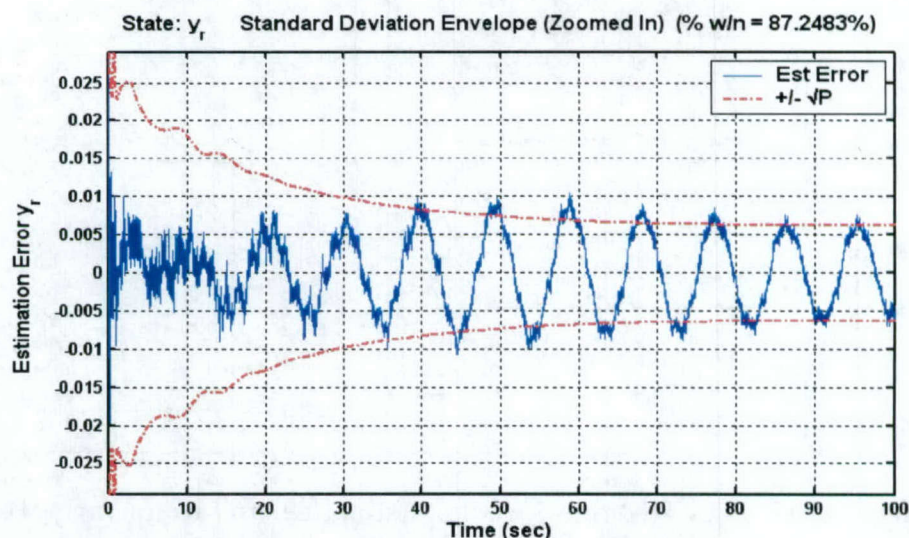


Figure 4-41. Estimation Error and Error Standard Deviation Envelope of y_r Estimation with ISS Model 1

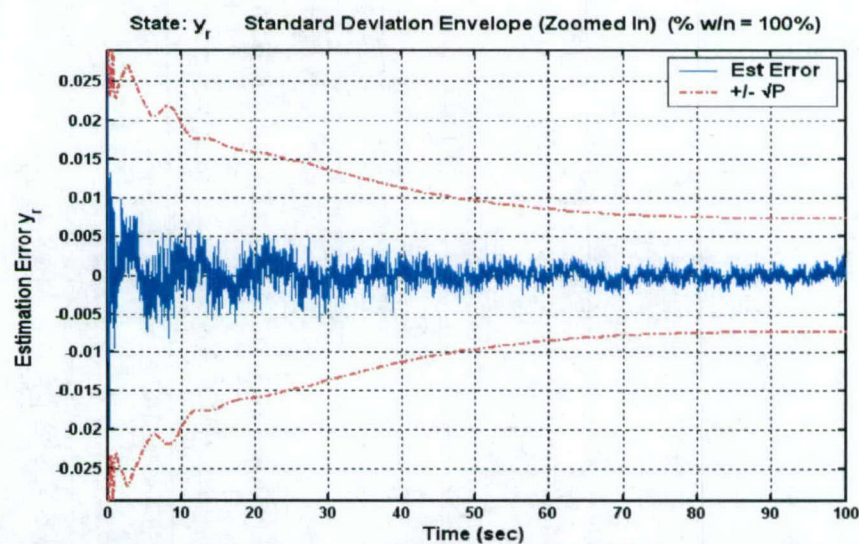


Figure 4-42. Estimation Error and Error Standard Deviation Envelope of y_r Estimation with ISS Model 2

Improved estimation using ISS Model 1 is also evident from the fact that estimation error does not stray outside the bounds of the estimation error standard deviation envelope (Figure 4-42).

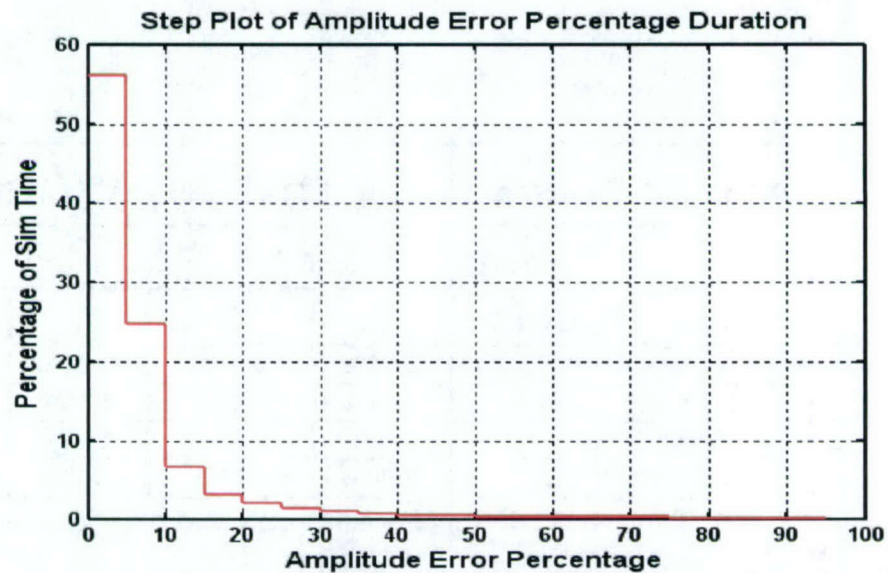


Figure 4-43. Duration of Error of y_r Estimation with ISS Model 1

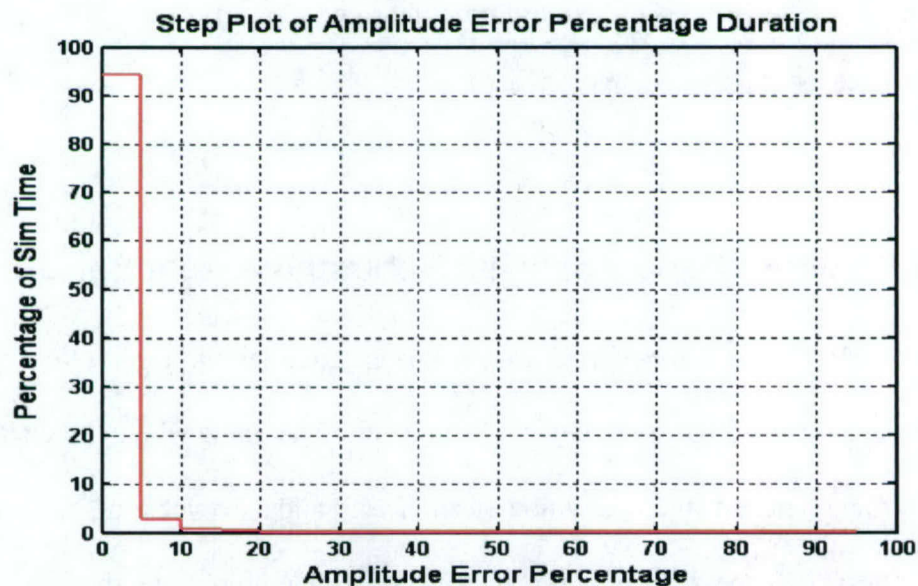


Figure 4-44. Duration of Error of y_r Estimation with ISS Model 2

Figure 4-44 shows that the occurrence of high estimation error can be decreased by using the expanded disturbance modeling found in ISS Model 2.

	Axis of Focus :	y and ϕ_x w/ spin-up				
	Test:	A		B		
	ISS Model #:	1	2	1	2	% imp
Rotor States	% Amp Error (x_r)	0.00%	0.00%	0.04%	0.04%	0.00%
	% Amp Error (y_r)	0.81%	0.93%	4.58%	0.81%	82.34%
	% Amp Error (ϕ_{xr})	0.82%	0.80%	2.66%	0.71%	73.32%
	% Amp Error (ϕ_{yr})	0.00%	0.00%	0.00%	0.00%	0.00%

Table 4-11. Results Focusing on y and ϕ_x (with spin-up)

The hypothesis also holds true during the rotor spin-up from 0 to 0.7 Hz over 300 seconds.

The results are shown in Table 4-11.

4.5 Monte Carlo Analysis: Robustness Test Set-Up

In order to test robustness to parameter uncertainty, each plant stiffness value was independently allowed to deviate from its nominal value where the deviations were defined by Gaussian distributions with a mean of zero and a 3σ value of 20% of the nominal value.

To test robustness to rotor imbalance disturbance amplitude, the components which make

up the rotor imbalance disturbance (M, ϵ, α), see Figure 3-2, were allowed to individually deviate from their nominal value where the deviations were defined by Gaussian distributions with a mean of zero and a 3σ value of 2 kg, 0.1 m, and 0.05 radians for M, ϵ , and α , respectively. To test robustness to ISS disturbance frequency uncertainty, the disturbance frequencies were allowed to deviate from their nominal values where the deviations were defined by Gaussian distributions with a mean of zero and a 3σ value of 20% of the nominal value.

Special care was taken in defining the distributions of the different deviations in order to prevent impossible deviations such as negative rodent mass, M . The Monte Carlo testing involved 1000 test runs of each uncertainty category using ISS Model 2. Other than the allowed deviations on the plant, nothing else in the simulation or the observer model was changed. The nominal spin frequency used equals 0.7 Hz, while the nominal ISS translational and rotational disturbance frequencies were chosen as the peak mode frequencies from the following two transfer functions, respectively: 1) d_{ys} to y_{rel} and 2) $d_{\phi_{xs}}$ to ϕ_{xrel} (see Figure 4-38).

4.5.1 Monte Carlo Analysis: Parameter Uncertainty Results

The following distributions are the result of the variation on the plant stiffness parameters as defined in Section 4.5.

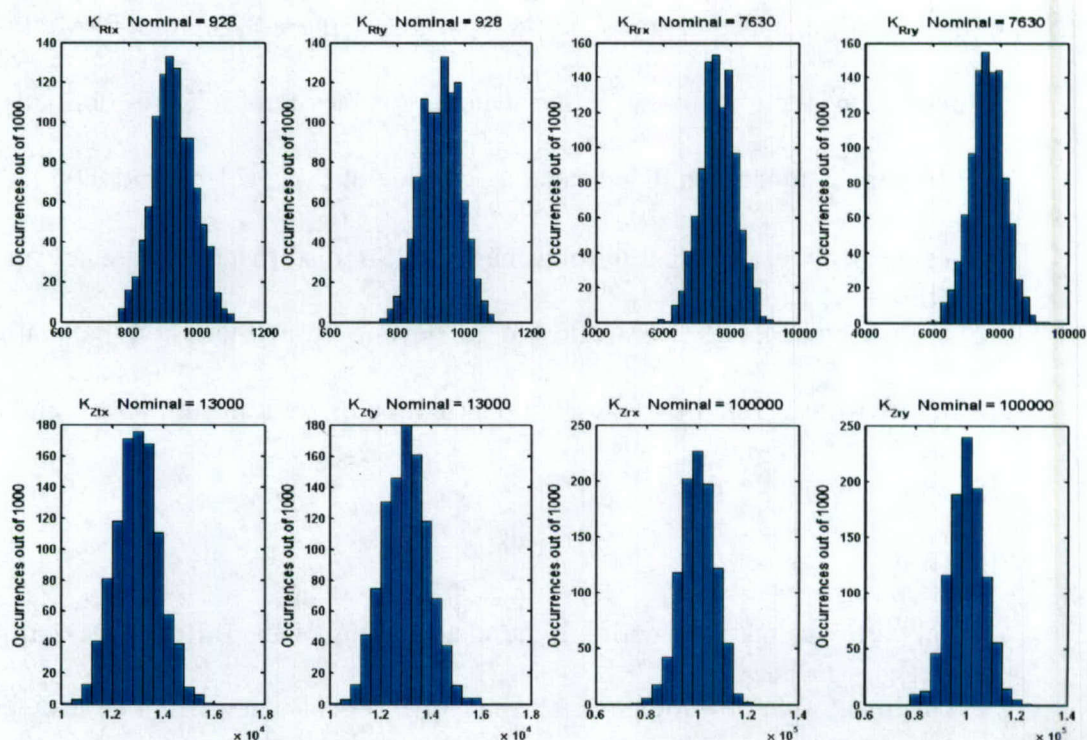


Figure 4-45. Distribution of Translational and Rotational Stiffness between Rotor and Shroud (top row) and Shroud and ISS Mass 1 (bottom row)

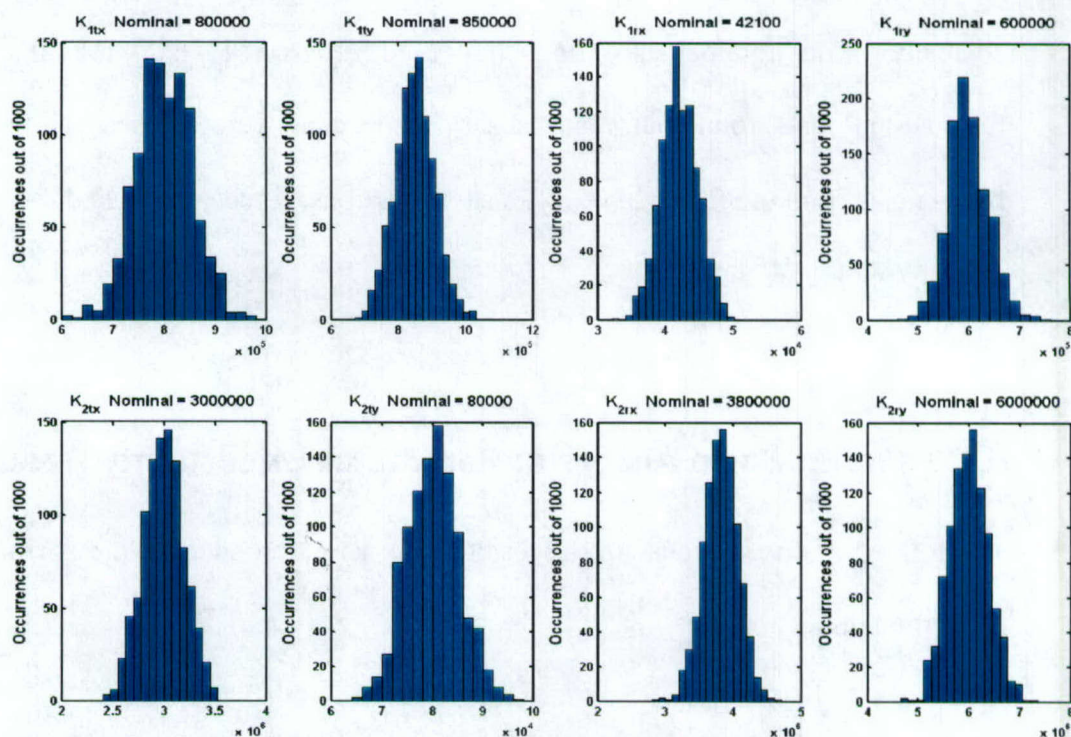


Figure 4-46. Distribution of Translational and Rotational Stiffness between ISS Mass 1 and ISS Mass 2 (top row) and ISS Mass 2 and Inertial (bottom row)

The variation of stiffness values forces a distribution of the plant's frequency response. The modal frequency distributions for the direct transfer functions (i.e. d_{xs} to x_{rel}) caused by the change in the stiffness parameters of the plant are shown in Figure 4-47 through Figure 4-50. The nominal Bode plots have been superimposed on the modal frequency distributions to show the variation from the nominal plant modal frequencies caused by the distribution of the plant stiffness parameters. Figure 4-47 through Figure 4-50 also provide information on which frequencies are more likely to be effected; that is, which frequencies will shift or appear/disappear due to variations in the stiffness parameters.

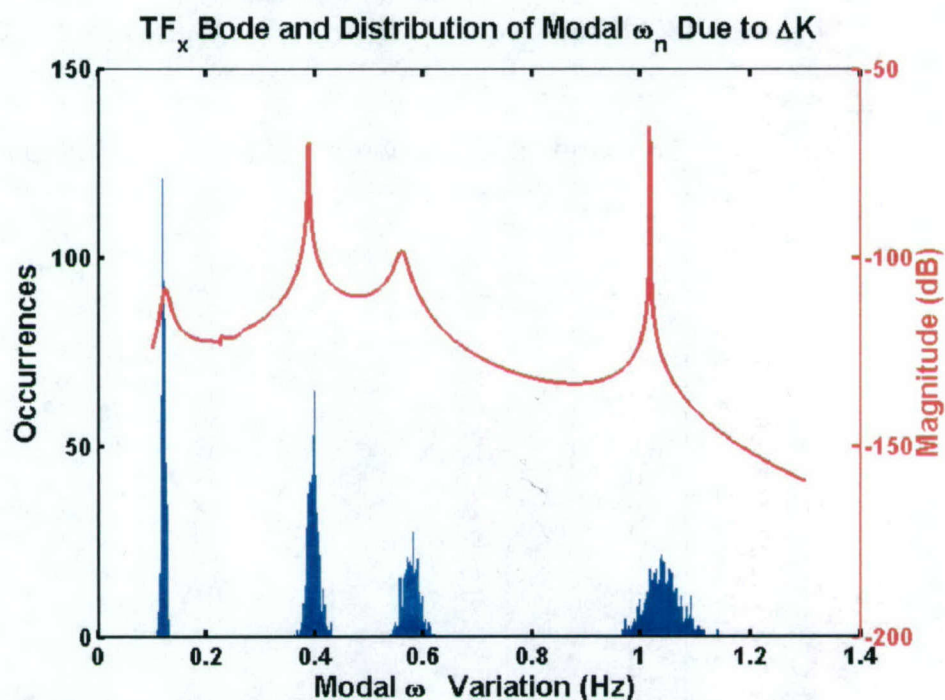


Figure 4-47. Modal Frequency Distribution Caused by ΔK (for d_{xs} to x_{rel})

Figure 4-48 and Figure 4-49 show that the higher modal frequencies will have a larger standard deviation from the nominal value than the lower frequencies.

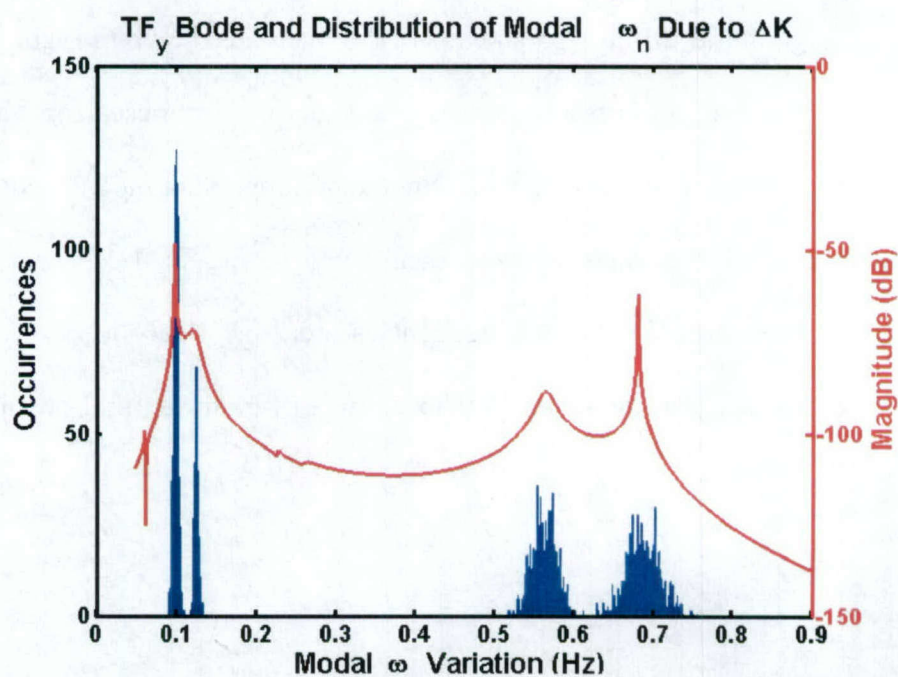


Figure 4-48. Modal Frequency Distribution Caused by ΔK (for d_{ys} to y_{rel})

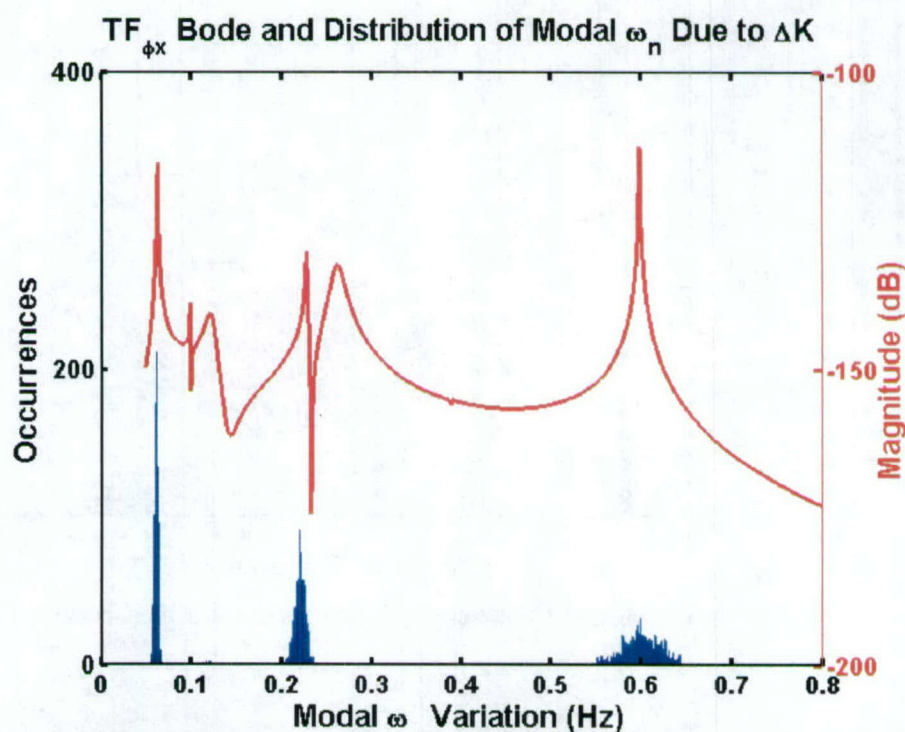


Figure 4-49. Modal Frequency Distribution Caused by ΔK (for $d_{\phi xs}$ to ϕ_{xrel})

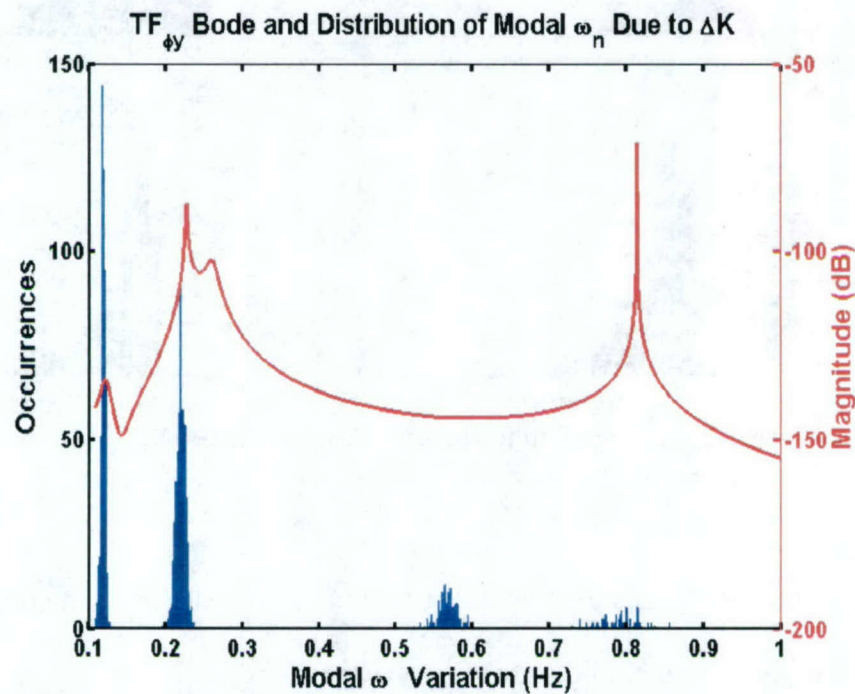


Figure 4-50. Modal Frequency Distribution Caused by ΔK (for $d_{\phi_{ys}}$ to ϕ_{yrel})

Figure 4-49 shows that the high frequencies are likely to shift away from the nominal value since the mean is not equal to the nominal value. Also in Figure 4-50, a new modal frequency appears around 0.58 Hz due to variations in plant stiffness parameters.

The Monte Carlo analysis results, testing estimation performance under conditions of parameter uncertainty can be found in Figure 4-51 below.

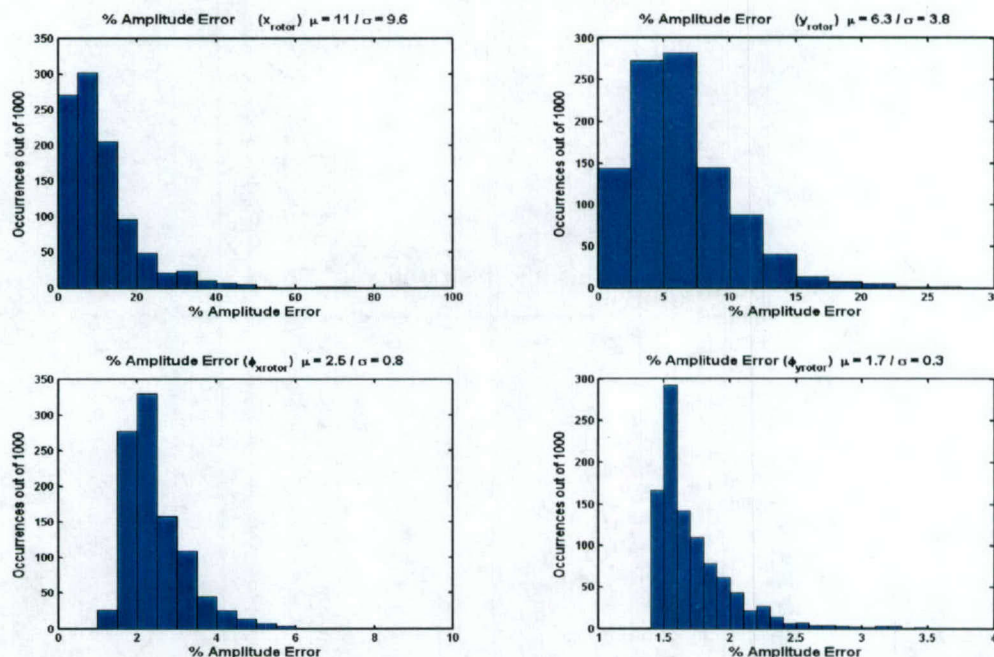
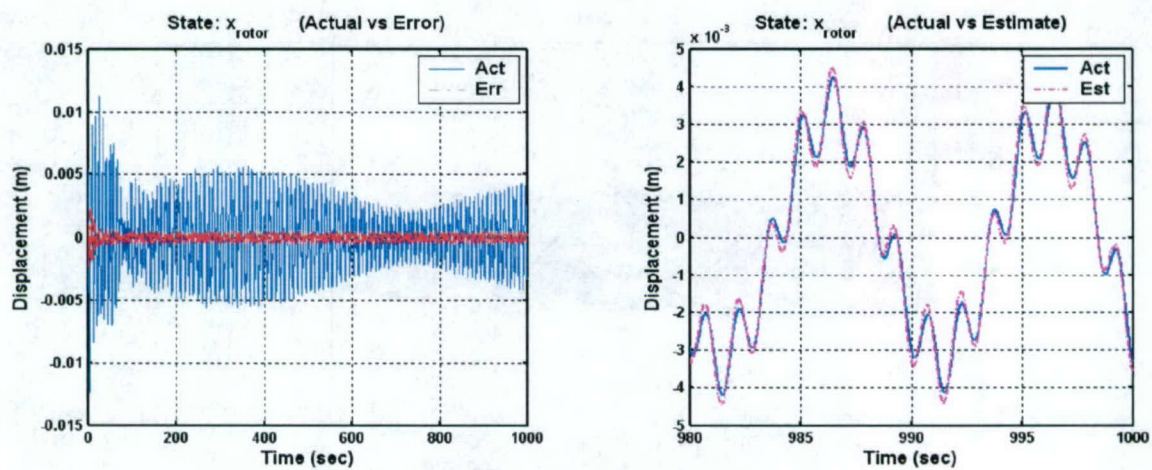
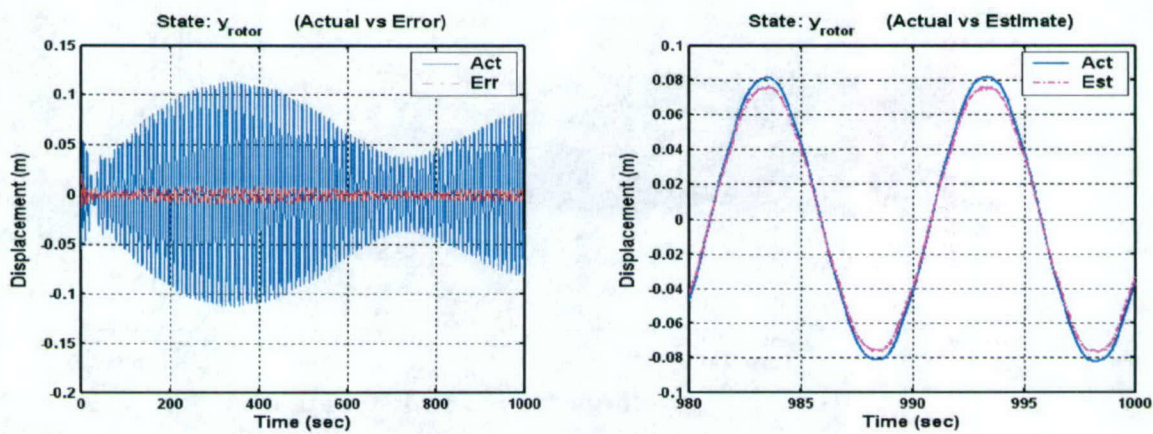
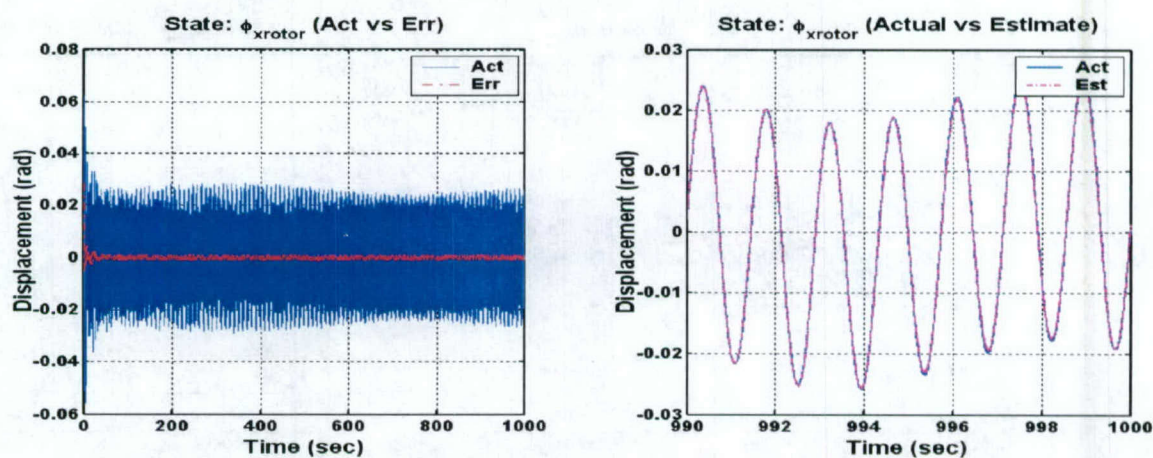
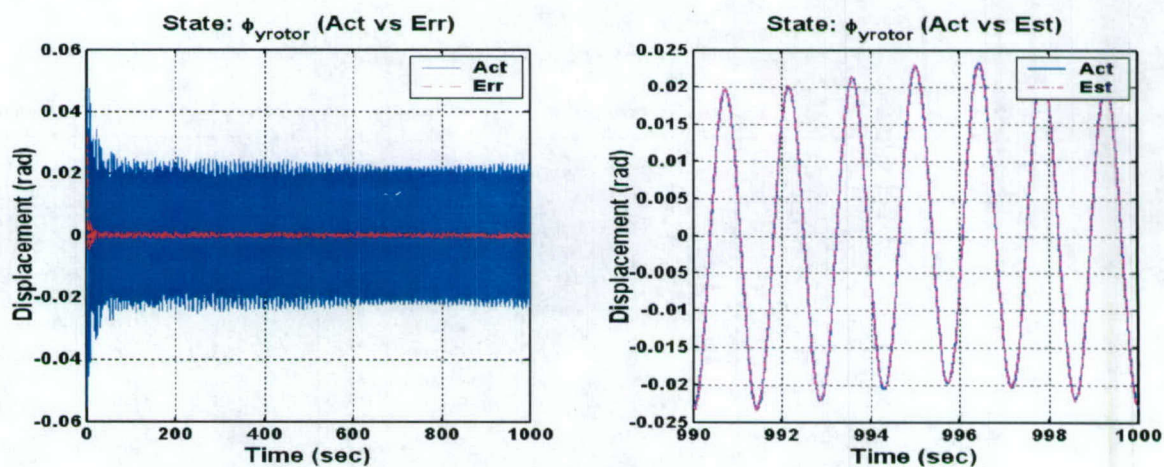


Figure 4-51. Monte Carlo Results Testing Parameter Uncertainty (no spin-up)

The largest percent amplitude error occurs in the translation of the rotor in the x axis. The estimation of the other dofs are very accurate.

It is important to note that the process noise covariance matrix, Q , does not change from the nominal Q during the Monte Carlo simulations. Since Q is determined by the level of uncertainty in the observer model, by increasing Q as the difference between the plant model and the observer model increased due to parameter changes, improved estimation would be expected. Time history plots, displayed in Figure 4-52 through Figure 4-55, were created using a set of parameters that produced the approximate mean amplitude error values, resulting from the Monte Carlo analysis, for all four motions of the rotor (x_r , y_r translations and ϕ_{xr} , ϕ_{yr} rotations). These parameter values produced a percent amplitude error of $x_r \rightarrow 11.79\%$, $y_r \rightarrow 6.3\%$, $\phi_{xr} \rightarrow 2.5\%$, and $\phi_{yr} \rightarrow 1.7\%$.

Figure 4-52. x_r EstimationFigure 4-53. y_r Estimation

Figure 4-54. ϕ_{xr} EstimationFigure 4-55. ϕ_{yr} Estimation

It is clear from Figure 4-52 through Figure 4-55 that the error is caused purely by amplitude differences between the actual and estimated states and not by phase lag or lead.

The Monte Carlo analysis results, with the time-varying case of rotor spin-up, can be found in Figure 4-56 below.

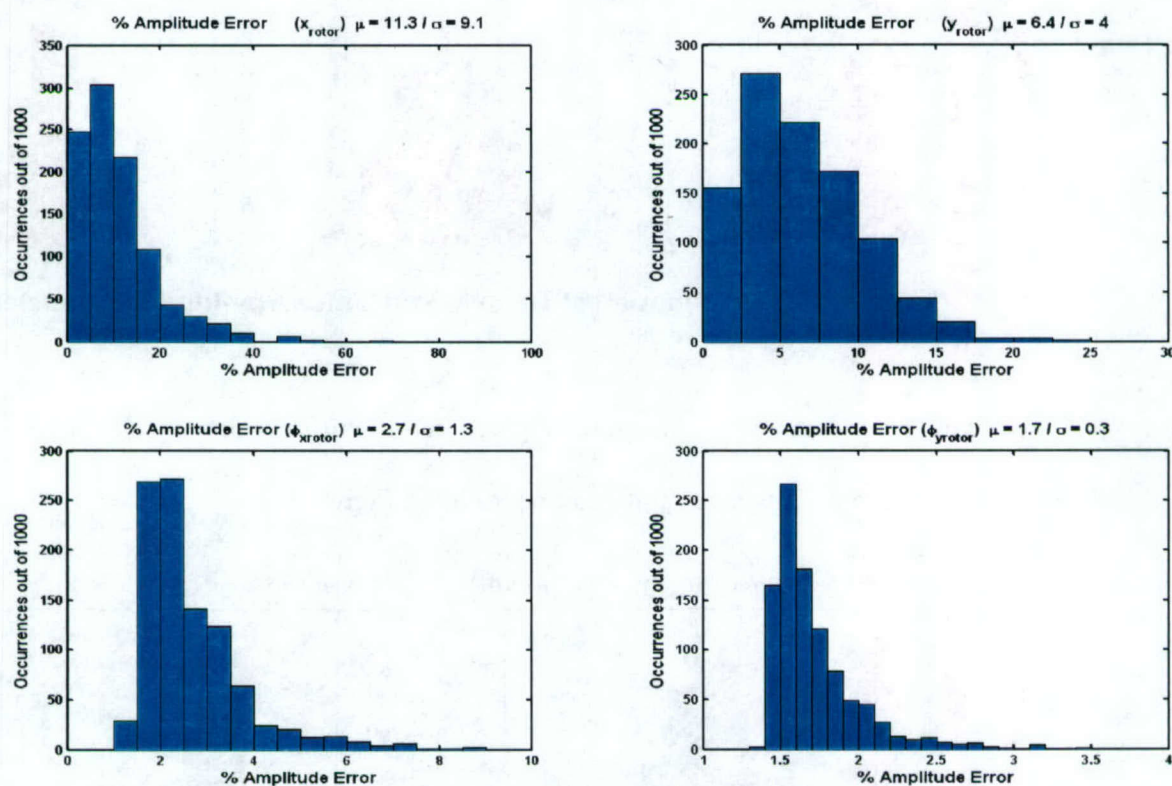


Figure 4-56. Monte Carlo Results Testing Parameter Uncertainty (with spin-up)

By comparing Figure 4-51 with Figure 4-56, it is evident that the Kalman filter performance is nearly identical regardless of time varying dynamics or time varying inputs.

4.5.2 Monte Carlo Analysis: Rotor Disturbance Amplitude Uncertainty Results

The following distributions are the result of the variation of the parameters that determine the amplitude of the rotor disturbance as defined in Section 4.5.

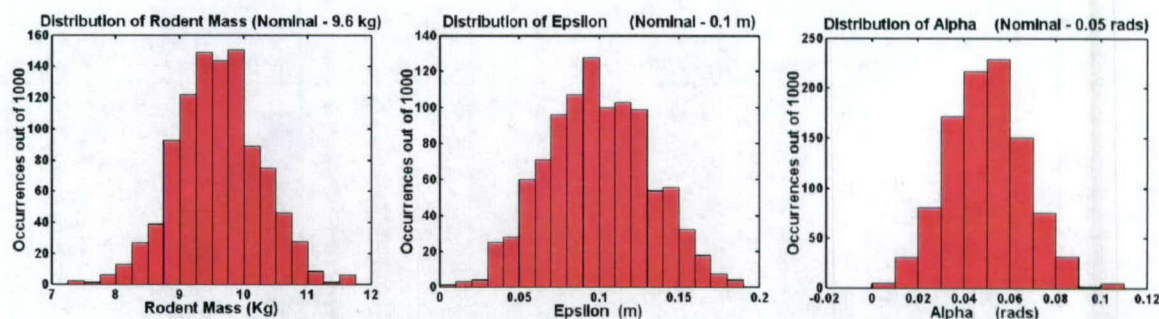


Figure 4-57. Distribution of Rotor Disturbance Amplitude Parameters

The Monte Carlo analysis results, testing estimation performance under conditions of rotor disturbance amplitude uncertainty can be found in Figure 4-58.

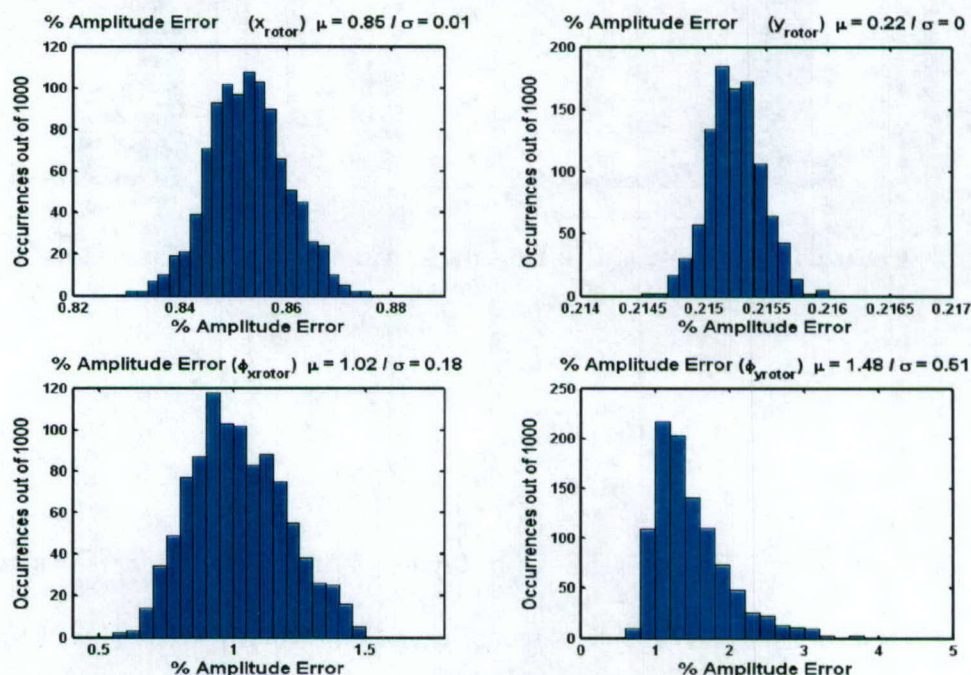


Figure 4-58. Monte Carlo Results Testing Rotor Disturbance Amplitude Uncertainty (no spin-up)

5 Conclusions

This thesis develops a state estimation algorithm for the Centrifuge Rotor (CR) system where only relative measurements are available with limited knowledge of both rotor imbalance disturbances and ISS thruster disturbances. A Kalman filter is applied to a plant model augmented with sinusoidal disturbance states used to model the effect of the ISS thrusters on the CR relative motion measurement. The sinusoidal disturbance states compensate for the lack of the availability of plant inputs for use in the Kalman filter. Testing confirms that complete disturbance modeling is necessary to ensure reliable estimation. Further testing goes on to show that increased estimator operational bandwidth can be achieved through the expansion of the disturbance model within the filter dynamics. In addition, Monte Carlo analysis shows the varying levels of robustness against defined plant/filter uncertainty variations.

Chapter 2 provided a problem overview and a concise description of the CR system. This included a description of the simplified model as well as the list of assumptions necessary for simplification. The model used for analysis and testing included a 4 mass (Rotor, shroud, ISS Mass 1, and ISS Mass 2), 16 degree of freedom, time-varying system. From this model, linearized equations of motion were derived.

In Chapter 3 a detailed description of how the disturbance models were implemented within the filter dynamics was formulated. This formulation required the derivation of both rotor and ISS disturbances. The rotor disturbance was derived as a function of imbalance geometry, mass/inertia, and spin rate, while the ISS disturbance modeling was done though

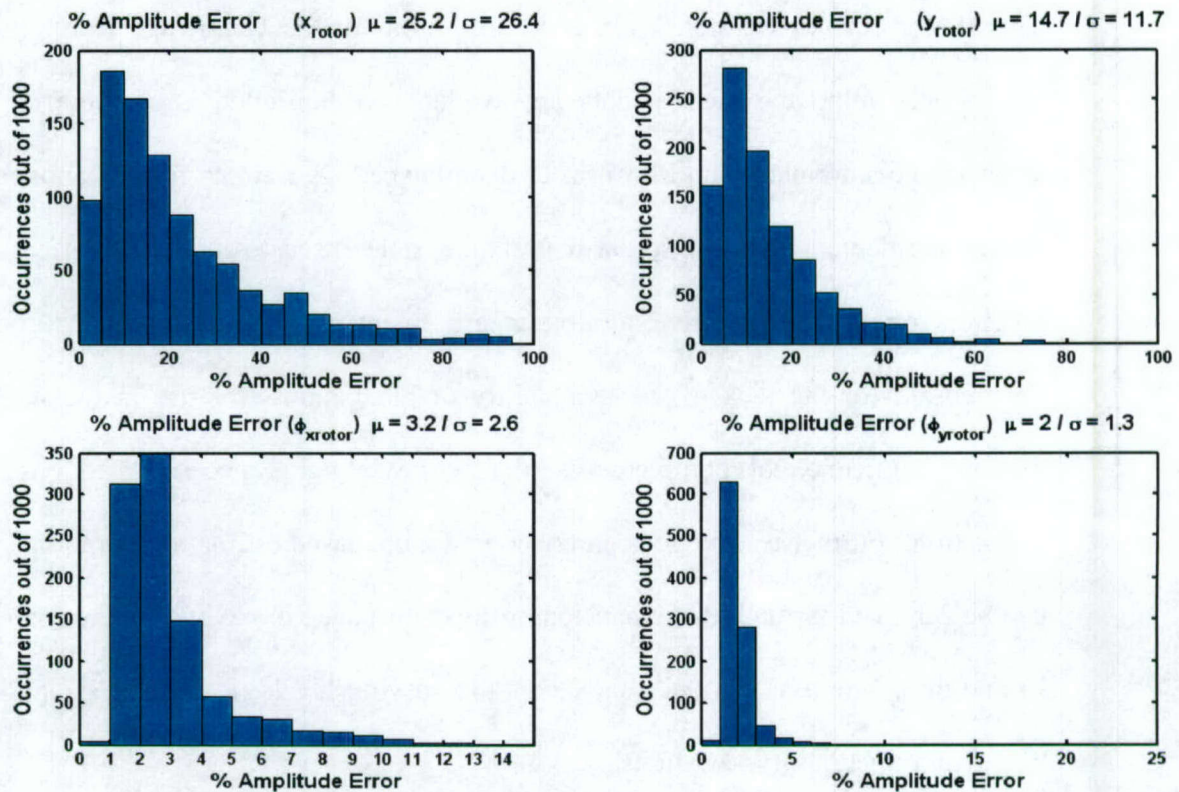


Figure 4-64. Monte Carlo Results Testing Combination of All Uncertainties (with spin up)

Relatively large errors result from the combination of all three uncertainty categories. Error in estimating ϕ_{x_r} and ϕ_{y_r} rotations remain relatively low while the errors in both x_r and y_r translation are relatively high. The two uncertainties having the most effect on estimation error are the plant parameter uncertainty and the ISS disturbance frequency uncertainty, both of which create frequency disparities between the plant and the filter models.

4.5.4 Monte Carlo Analysis: Combination of All Uncertainties Results

Monte Carlo analysis was conducted combining the plant parameter uncertainty, the rotor disturbance amplitude uncertainty, and the ISS disturbance frequency uncertainty in order to determine the error for a case with all uncertainties acting at the same time. The results for this analysis can be found in Figure 4-63 for the time-invariant case, and in Figure 4-64 for the rotor spin-up case.

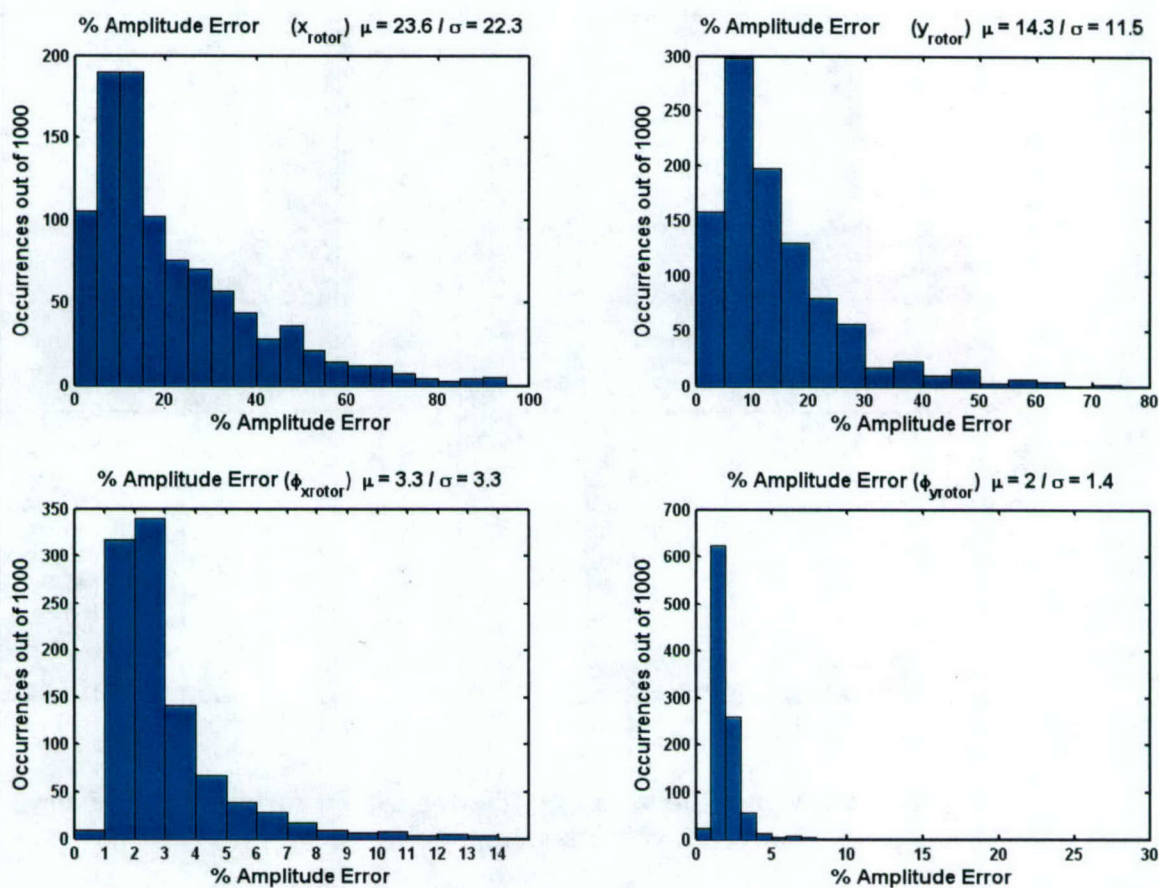


Figure 4-63. Monte Carlo Results Testing Combination of All Uncertainties (no spin up)

Figure 4-61 shows that the largest errors are caused by ISS disturbance frequency uncertainty. Therefore, it will be important to determine the ISS disturbance frequencies of concern and to expand the ISS disturbance model to capture all of them.

The Monte Carlo analysis result, considering a time-varying plant and disturbance inputs, can be found in Figure 4-62.

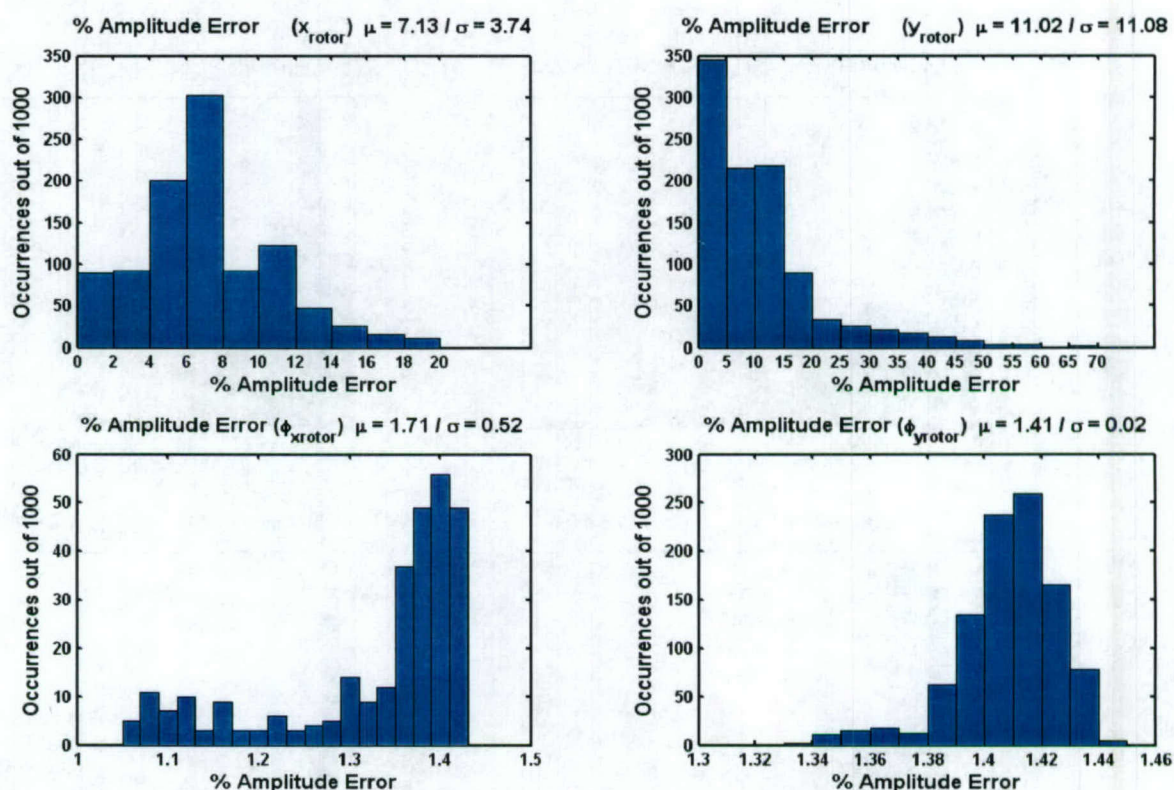


Figure 4-62. Monte Carlo Results Testing ISS Disturbance Frequency Uncertainty (with spin up)

Again, similar results are found between the time-invariant and time-varying Monte Carlo analysis, supporting the conclusion that the Kalman Filter operates similarly for both cases.

4.5.3 Monte Carlo Analysis: ISS Disturbance Frequency Uncertainty Results

The distributions, shown in Figure 4-60, are the result of the variation of both the translational and rotational ISS disturbance frequencies as defined in Section 4.5.

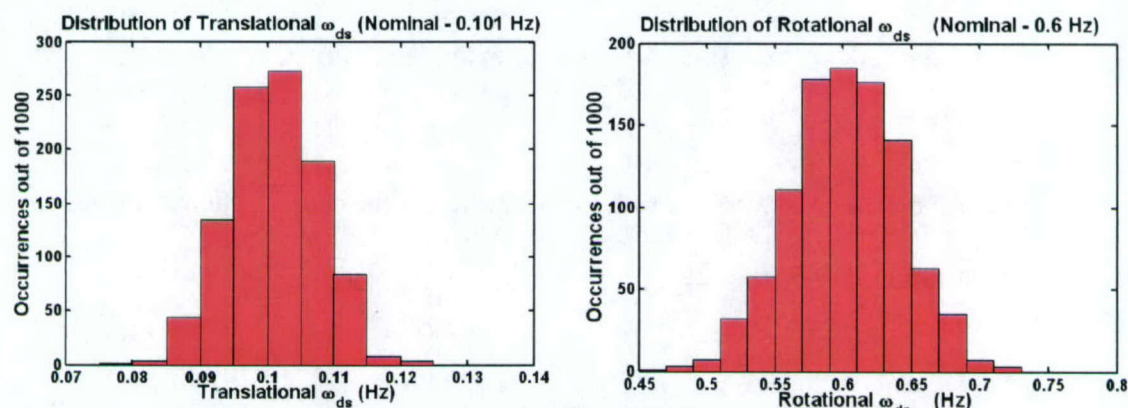


Figure 4-60. Distribution of Translational and Rotational ISS Disturbance Frequencies

The Monte Carlo analysis results, testing estimation performance under conditions of ISS disturbance frequency uncertainty can be found in Figure 4-61.

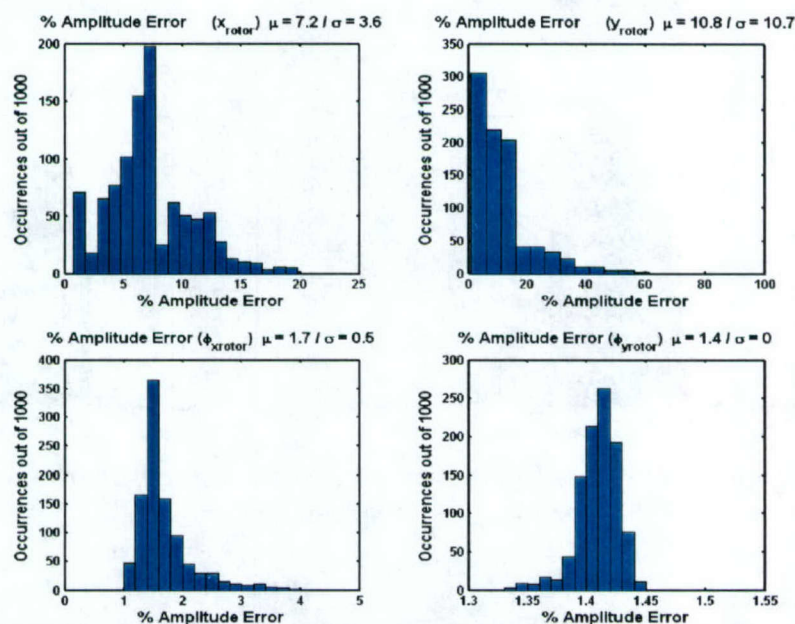


Figure 4-61. Monte Carlo Results Testing ISS Disturbance Frequency Uncertainty (no spin up)

From Figure 4-58 it is evident that the Kalman filter performance is insensitive to rotor disturbance amplitude per the defined distributions. This result is important, because rodent motion and rodent mass modeling discrepancies are expected during normal operations due to the fact that there is no way to predetermine the rodent motion or to predict the rodent mass fluctuations over extended study periods.

The Monte Carlo analysis result, considering a time-varying plant and disturbance inputs, can be found in Figure 4-59.

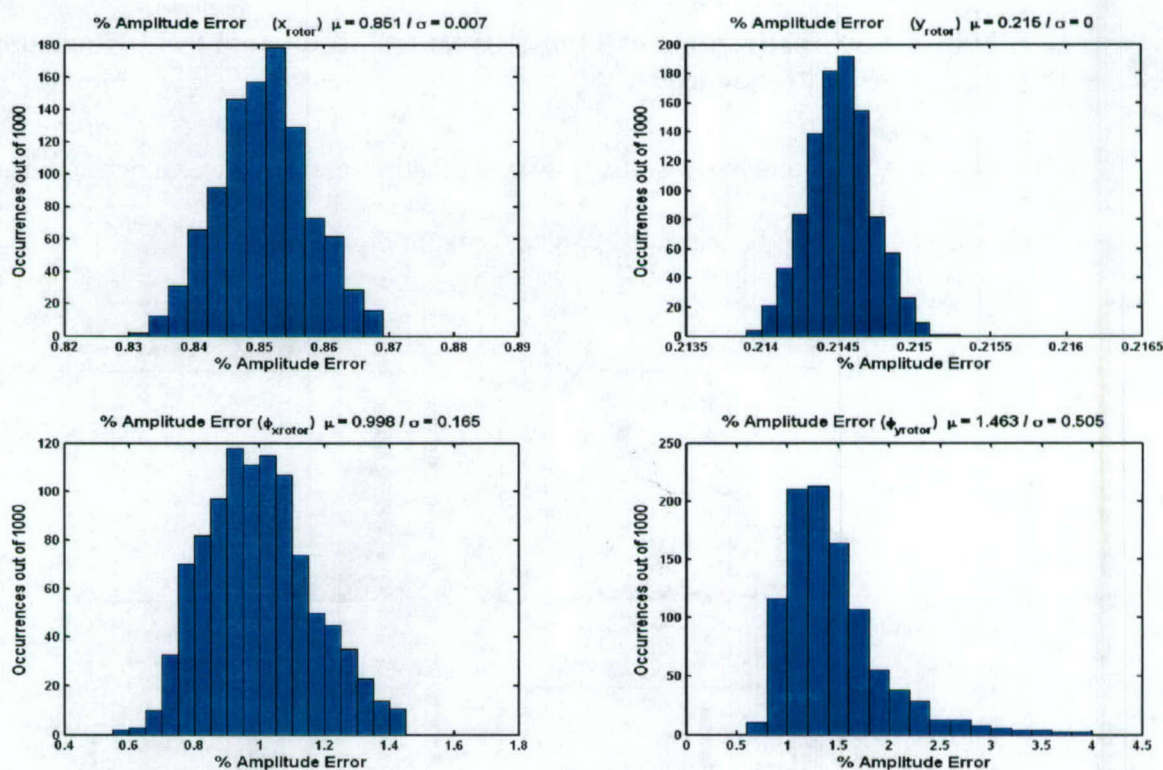


Figure 4-59. Monte Carlo Results Testing Rotor Disturbance Amplitude Uncertainty (with spin-up)

Similar results are seen between the time-invariant and time-varying Monte Carlo analysis, supporting the conclusion that the Kalman Filter is effective for both cases.

a sinusoidal approximation of the effect of a pulse train through the system dynamics. Modeling the ISS disturbances in such a manner introduced another complexity (i.e. the modeling of a pulse train disturbance input) into the CR state estimation example. Observability for both the plant and filter models was evaluated. Since both models are time varying, observability needed to be checked for each variation of the model dynamics using both a time-invariant test as well as a time-varying test for observability. It was shown that the plant model is observable over the entire range of spin frequencies, and the filter model is observable over the entire range of the combinations of constant spin and ISS disturbance frequencies, except for low spin frequencies below 0.015 Hz. This is reasonable since low spin frequencies would create very small rotor disturbances, thus not affecting the system. Also, the discrete Kalman filter equations and algorithm are introduced along with a method for calculating initial Kalman filter parameters.

In Chapter 4 the results from testing using the solution method proposed in Chapter 3 were presented. After determining performance measures, comparisons were made between different fidelities of disturbance modeling to show that it is necessary to model all of the disturbances which act on the plant in order to achieve good estimation. Also, comparisons were made between two filter models (ISS Model 1 and ISS Model 2), with different levels of ISS disturbance frequency modeling, show that expanding the disturbance model within the filter model will increase the range of disturbance frequencies for which the Kalman filter is effective. Finally Monte Carlo analysis shows that errors are sensitive to plant uncertainties as well as ISS disturbance frequency uncertainties. Therefore, care must be taken to ensure that the filter model is as close to the plant model as possible. An on-line

system identification process may be necessary to detect and automatically adjust for any changes between the plant and the filter models [33][34][35]. Monte Carlo analysis also showed that it will be important to expand the filter model to cover the entire range of ISS disturbance frequencies.

In conclusion, the use of disturbance modeling within the filter dynamics has proven to be useful in situations where the disturbance inputs into the plant are not available. Since many user defined parameters are not changed through the testing process, namely the process noise covariance, Q , and the initial error covariance, P_0 , the results provided are not the best possible. Therefore, for future work a method for updating Q and calculating P_0 in an optimal fashion should be investigated.

6 References

- [1] NASA. Website: <http://spaceflight.nasa.gov/gallery/images/station/index.html>
- [2] NASA Station Payloads. Website: <http://stationpayloads.jsc.nasa.gov>
- [3] Liu, Jui-Jung, Chin-Kao Ma, I-Chung Kung, and Dong-Cherng Lin, "Input Force Estimation on a Cantilever Plate by Using a System Identification Technique", *Computational Methods in Applied Mechanics and Engineering* 190 1309-1322, 2000
- [4] B. Hillary, D.J. Ewins, "The use of strain gauges in force determination and frequency response function measurements, *Proceedings of Fourth IMAC*, 1986: 627-634
- [5] Postma, Barry D., Robust Constrained Optimization Approach to Control Design for International Space Station Centrifuge Rotor Auto Balancing Control System, Masters of Science Thesis, Rice University, 1994
- [6] Stelzner, Adam D., Daniel C. Kammer, and Paul Milenkovic, "A Time Domain Method for Estimating Forces Applied to an Unrestrained Structure", *Journal of Vibration and Acoustics*, 2000
- [7] Carne, T.G., Bateman, V.I., and R.L. Mays, "Force Reconstruction Using a Sum of Weighted Accelerations Technique", *10th International Modal Analysis Conference*, 1992
- [8] Genaro, G., and D.A. Rade, "Input Force Identification in the Time Domain", *16th International Modal Analysis Conference*, 1998
- [9] Starkey, J.M. and G.L. Merrill, "On the Ill-Conditioned Nature of Indirect Force-Measurement Techniques", *Journal of Modal Analysis*, 1989: 103-108

- [10] Chang, Shao-Kung, You, Wen-Tong, and Hsu, Pau-Lo, "Design of General Structured Observers for Linear Systems with Unknown Inputs", *Journal of the Franklin Institute*, Vol 334B, No 2, 1997: 213-232
- [11] Darouach, M. Zasadzinski and S.J. Xu, "Full-order Observers for Linear Systems with Unknown Inputs", *IEEE Transactions on Automatic Control*, Vol 39, 1994: 606
- [12] Hou, M. and P.C. Müller, "Design of Observers for Linear Systems with Unknown Inputs", *IEEE Transactions on Automatic Control*, Vol 37, 1992: 871
- [13] Yang, F., and R.W. Wilde, "Observers for Linear Systems with Unknown Inputs", *IEEE Transactions on Automatic Control*, Vol 33, 1988: 677
- [14] Wie, Bong. Space Vehicle Dynamics and Control, American Institute of Aeronautics and Astronautics, Inc., Reston, V.A., 1998
- [15] Yamamoto, Toshio, and Yukio Ishida, Linear and Nonlinear Rotordynamics: A Modern Treatment with Applications, John Wiley & Sons, Inc., New York, N.Y., 2001
- [16] Bedrossian, Naz. "ISS Russian GN&C Systems Flex Verification and Flight Experience Overview", American Institute of Aeronautics and Astronautics, Inc. Reston, V.A., 2003
- [17] Howard, Roy M. Principles of Random Signal Analysis and Low Noise Design: The Power Spectral Density and Its Applications, John Wiley & Sons, Inc., New York, N.Y., 2002
- [18] Southall, B., B.F. Buxton, and J.A. Marchant, "Controllability and Observability: Tools for Kalman Filter Design", *British Machine Vision Conference*, 1998: 164-173

- [19] Juang, Jer-Nan and Minh Q. Phan, Identification and Control of Mechanical Systems, Cambridge University Press, New York, N.Y., 2001
- [20] Peters, M.A. and P.A. Iglesias, "A Spectral Test For Observability and Reachability of Time-Varying Systems", *SIAM Journal of Control and Optimization*, 1999: 1330-1345
- [21] Ogata, Katsuhiko, Modern Control Engineering, 3rd ed., Prentice Hall, Upper Saddle River, New Jersey, 1996
- [22] Mangoubi, Rami S., Robust Estimation and Failure Detection: A Concise Treatment, Springer-Verlag, London, 1998
- [23] Gelb, Arthur, Joseph F. Kasper, Jr., Charles F. Price, and Arthur A. Sutherland, Jr., Applied Optimal Estimation, The M.I.T Press, Cambridge, Massachusetts, 1974
- [24] Stegel, Robert F., Optimal Control and Estimation, Dover Publications, Inc., New York, N.Y., 1994
- [25] Kalman, R.E., "A New Approach to Linear Filtering and Prediction Problems", *Transactions of the ASME – Journal of Basic Engineering*, 1960
- [26] Welsh, Greg, and Gary Bishop, "An Introduction to the Kalman Filter", Department of Computer Science, April 5, 2004
- [27] Zarchan, Paul, and Howard Musoff, Fundamentals of Kalman Filtering: A Practical Approach, American Institute of Aeronautics and Astronautics, Inc., Reston, V.A., 2000
- [28] Ravikanth, Rayadurgam, and Sean P. Meyn. "Bounds on Achievable Performance in the Identification and Adaptive Control of Time Varying Systems". *IEEE Transactions on Automatic Control*, Vol 44, No 4, 1999: 670-682

- [29] Guo, Lei, and Lennart Ljung. "Performance Analysis of General Tracking Algorithms". *IEEE Transactions on Automatic Control*, Vol 40, No 8, 1995: 1388-1402
- [30] The MathWorks, Inc. Matlab v.6.5.1, 2002. Website: <http://www.mathworks.com>
- [31] Sobol', I. M., A Primer for the Monte Carlo Method. CRC Press, Boca Raton, 1994.
- [32] Spanos, P.D. and J.B. Roberts. Random Vibration and Statistical Linearization. Dover Publications, Inc., Mineola, N.Y., 2004.
- [33] Keller, B., "On-Line Physical Parameter Identification and Adaptive Control of a Launch Vehicle," Ph.D. Thesis, Dept. of Aeronautics and Astronautics, Stanford, Univ., Stanford, CA, March 1993
- [34] Horta, Lucas G., and Chris A. Sandridge, "On-line Identification of Forward/Inverse Systems for Adaptive Control Applications", *AIAA Guidance, Navigation, and Control Conference*, Hilton Head Island, SC, 1992: 1639-1649
- [35] Kammer, Daniel C., and Adam D. Stelzner. "Structural Identification Using Inverse System Dynamic", *Journal of Guidance, Control, and Dynamics*, Vol 23, No 5, 2000: 819-825